MODELLING MELT POOL CHARACTERISTICS TO PREDICT PROCESS PARAMETERS FOR SELECTIVE LASER MELTING OF TITANIUM ALLOYS

MARTHINUS STEYN VAN RHIJN

Dissertation submitted in fulfilment of the requirements for the degree

MASTER OF ENGINEERING IN

MECHANICAL ENGINEERING

in the

Department of Mechanical and Mechatronics Engineering
Faculty of Engineering, Built Environment and Information Technology

at

Central University of Technology, Free State

Supervisor: Prof WB du Preez, PhD
Co-supervisors: Dr M Maringa, PhD
Dr D Kouprianoff, DEng

BLOEMFONTEIN
February 2023

Declaration of Independent Work

I, MARTHINUS STEYN VAN RHIJN, identity number _____ and student number _____, do hereby declare that this research project submitted to Central University of Technology, Free State, for the degree MASTER OF ENGINEERING IN MECHANICAL ENGINEERING, is my own independent work; and complies with the Code of Academic Integrity, as well as other relevant policies, procedures, rules and regulations of Central University of Technology, Free State; and has not been submitted before to any institution by myself or any other person in fulfilment (or partial fulfilment) of the requirements for the attainment of any qualification.

_____ 09/02/2023

SIGNATURE OF STUDENT **DATE**

Acknowledgements

I would like to express my deepest appreciation to my supervisors, Prof. Willie du Preez, Dr Maina Maringa and Dr Dean Kouprianoff, for their unwavering support, valuable advice, extensive knowledge and, most of all, their patience in a study that took longer to complete than anticipated. The completion of my dissertation would not have been possible without their support and guidance.

I am also extremely grateful to the Department of Science and Innovation (DSI) through the Collaborative Program in Additive Manufacturing (CPAM), as well as CUT through their postgraduate grant awards programme, who provided me with the financial support that enabled me to complete this study.

I would like to extend my sincere thanks to Dr Thywill Dzogbewu for his guidance and experience, as he supported and guided me in preparing high-quality experimental samples for this study.

I also wish to thank CRPM for the processing of experimental samples, as well as PDTS for the machining of the experimental samples processed in this study.

I want to extend a very special thank you to my wife for all her love and support throughout this study, especially during this last year. Your encouragement and belief in me mean more to me than you will ever know.

Lastly, and most importantly, I would like to thank my heavenly Father for providing me with the opportunity to investigate a small part of a universe that was created unfathomably complex and interesting. To Him be all the glory and praise.

Abstract

The time-consuming experimental process required to optimize process parameters for the selective laser melting (SLM) of new materials is a major hurdle in adopting this technology. For this reason, various methods in the literature attempt to shorten the time taken to optimise the process parameters for a specific material. One possible solution to this problem is the use of accurate numerical modelling to predict the required process parameters. Currently, melt pool modelling on part-scale is computationally expensive and not a feasible method for reducing the time required for the optimisation of process parameters. However, some studies have indicated that it is possible to effectively optimise process parameters through experimental investigation of the cross-sectional geometry of the molten region of single tracks created at various process parameters. It follows, therefore, that the accurate modelling of single tracks can be an effective way of determining optimal process parameters. This study reports on efforts to set up a numerical model of a single track of the SLM process that is accurate enough to be effectively used to optimise process parameters. Experimental and simulation results were obtained for a broad range of laser powers and scanning speeds to investigate the accuracy of the model. Thereafter, the effects of changing various simulation parameters on the accuracy of the model with respect to simulated melt pool dimensions were investigated to find parameters that could be responsible for inaccuracies in the developed model. These parameters included the temperature-dependent absorptivity of the material, the evaporation pressure coefficient, and to a lesser extent, the effect of temperature on the surface tension. It was concluded that provided that accurate values could be obtained for the simulation parameters discussed in this document, single-track SLM simulations could be a very powerful tool for quickly and effectively determining process parameters for any material.

Publications Emanating From This Research

Publications in peer-reviewed journals

Van Rhijn, T., Du Preez, W., Maringa, M. and Kouprianoff, D. (2022). An Investigation into the Optimization of the Selective Laser Melting Process Parameters for Ti6Al4V Through Numerical Modelling, Journal of The Minerals, Metals & Materials Society (JOM), DOI: doi.org/10.1007/s11837-022-05608-2

Van Rhijn, T., Du Preez, W., Maringa, M. and Kouprianoff, D. (2021). Towards Predicting Process Parameters for Selective Laser Melting of Titanium Alloys Through the Modelling of Melt Pool Characteristics. South African Journal of Science and Technology 40 (1), DOI: doi.org/10.36303/SATNT.2021cosaami.32 (The proceedings of the CoSAAMI 2021 conference were published in this journal.)

Papers accepted and presented in international peer-reviewed conferences

Van Rhijn, M. S., Du Preez, W., Maringa, M. and Kouprianoff, D. (2021). Towards Predicting Process Parameters for Selective Laser Melting of Titanium Alloys Through the Modelling of Melt Pool Characteristics. Conference of the South African Advanced Materials Initiative. 18-21 October 2021. (CoSAAMI 2021)

Van Rhijn, M. S., Du Preez, W. B. and Maringa, M. (2020). Towards predicting process parameters for selective laser melting of titanium alloys through modelling of melt pool characteristics. 21st RAPDASA Annual International Conference, Stellenbosch. 4-6 November 2020. (This paper was accepted after peer review but could not be accommodated in the conference proceedings due to the restriction that did not allow more than 40% of the total number of published papers to be from one institution.)

Table of Contents

List of Figures

List of Tables

List of Symbols

P	Power
v	Velocity
h	Hatch spacing
t	Powder layer thickness
d	Laser spot size
E_v	Volumetric Energy Density
E_L	Linear Energy Density (LED)
E_S	Surface Energy Density
ρ	Density
h	Enthalpy
$\dot{q}_s$	Rate of heat transfer per unit area
$\dot{q}_V$	Rate of heat source per unit volume
t	Time
s	Displacement
T	Temperature
H^{vap}	Latent heat of vaporisation
V	Volume
γ	Ratio of specific heats
C_v^{vap}	Specific heat at constant volume
P_{evap}	Evaporation pressure
$\dot{m}$	Mass flow rate
M	Molecular mass
R	Universal gas constant
P_l^{sat}	Saturation pressure

q_{evap}	Heat loss due to evaporation

List of Abbreviations

ALE	Arbitrary Lagrangian Eulerian
AM	Additive manufacturing
CAD	Computer-aided design
CFD	Computational fluid dynamics
CNC	Computer numerical control
CPTi	Commercially pure titanium
CRPM	Centre for Rapid Prototyping and Manufacturing
DED	Directed energy deposition
DEM	Discrete element method
DMLS	Direct metal laser sintering
EBM	Electron beam melting
EDM	Electric discharge machining
FDM	Finite difference method
FEM	Finite element method
FVM	Finite volume method
GMRES	Generalised minimal residual method
HAZ	Heat-affected zone
HPC	High-performance computing
HTC	Heat transfer coefficient
ISS	International space station
LBM	Lattice Boltzmann method
LED	Linear energy density
LENS	Laser-engineered net shaping
LLNL	Lawrence Livermore National Laboratories

LOM	Laminated object manufacturing
L-PBF	Laser powder bed fusion
mLS	Metal laser sintering
Nd:YAG	Neodymium-doped yttrium aluminium garnet
PBF	Powder bed fusion
PDTS	Product Development Technology Station
ppm	Particles per million
PSD	Particle size distribution
RSD	Relative standard deviation
RSM	Response surface methodology
SLM	Selective laser melting
SLS	Selective laser sintering
STC	Surface tension coefficient
STL	Stereolithography file type
UC	Ultrasonic consolidation
VOF	Volume of fluid method

Chapter 1 - Introduction

1.1. Background

The concept of additive manufacturing (AM) was considered in the 1950s and 1960s (Gibson et al., 2015). However, at the time, the various technologies related to the process of AM, such as computer hardware and software, laser technology and AM-specific materials, were not sufficiently developed. Various patents were filed as the relevant technologies caught up with the concept of AM in the early 1980s. All of these patents had the same basic idea of building three-dimensional objects by adding layers of material on top of each other (Gibson et al., 2015). A stereolithography patent by Charles Hull is widely considered the most influential in the rise of AM, as it brought about 3D Systems (Shellabear & Nyrhila, 2004). Further patents later in the 1980s gave rise to three AM companies and the commercialisation of the selective laser sintering (SLS) process (Shellabear & Nyrhila, 2004).

The powder bed fusion (PBF) process was one of the first AM processes to be used commercially. Selective laser sintering was first used, after which a few different PBF techniques were also developed. These included solid-state sintering, chemically induced sintering, partial melting, full melting, or selective laser melting (SLM), most commonly associated with the fusion of engineering metals (Gibson et al., 2015).

The basic working principle of all PBF processes is the same. A heat source, most commonly a laser, is used. Other heat sources, such as electron beams, can also be used. These sources are used to fuse very thin layers of powder particles, initially, to the build platform and thereafter to layers of the component being manufactured. This process of building layer upon layer is repeated until a complete, three-dimensional product is formed (Gibson et al., 2015).

The SLM process involves many process variables that can affect the quality of the final part. However, the operator cannot easily or effectively change all these parameters. These parameters are also often interdependent. Therefore, the process parameters cannot be optimised by simply keeping all other parameters constant and only optimising

a single parameter at a time. Due to this interdependence, as well as the time and cost involved in conducting such experimental procedures, it proves challenging to optimise the entire process. Process parameters that play a large role in determining the properties of the products produced by the SLM process can be categorised into laser-related parameters, scanning-related parameters, powder-related parameters and temperature-related parameters (Sun et al., 2017).

There is consensus that the four process parameters that can relatively easily be altered by the machine operator and have a considerable impact on the quality of the final part are laser power (P), laser scanning speed (v), hatch spacing (h) and powder layer thickness (t). The quality of parts is measured non-destructively by measuring the relative density and surface roughness of as-built parts. A more detailed discussion about the aforementioned parameters and their effect on the quality of parts is provided in the literature study in Chapter 2. For this reason, these four process parameters are most often investigated when attempting to optimise process parameters (Gong et al., 2013).

Some published studies contained information on the effect of laser scanning speed and laser power, hatch spacing and powder layer thickness on the density of parts obtained by employing systematic experimental trials. Gong et al. (2013) identified a processing window in which fully dense parts could be created for a specific Ti6Al4V powder by varying both laser power and scanning speed and measuring the density of the obtained parts. A graphical representation of this processing window can be seen in Figure 1. In this figure, fully dense parts of high quality are created in Zone I. In all other zones, porous or incomplete parts are created (Gong et al., 2013).

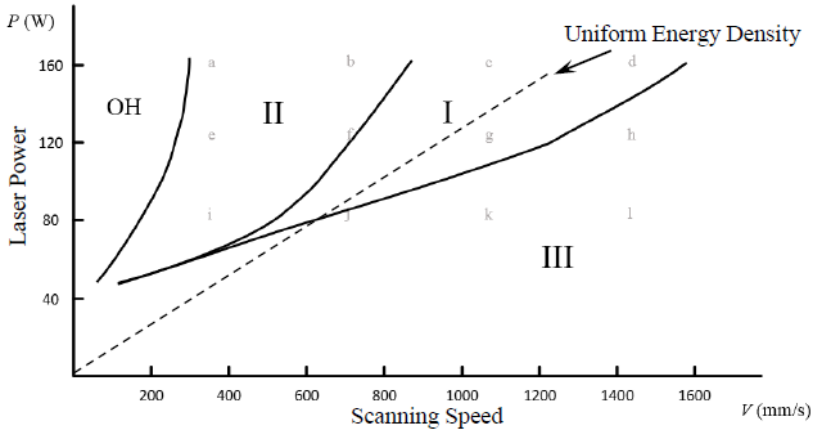

Figure 1: Processing window for Ti6Al4V (Gong et al., 2013)

Due to the current time-consuming nature of the experimental optimisation of process parameters, recent studies focused on optimising process parameters by predicting the optimal process parameters through modelling and simulation methods (Cheng et al., 2019), (Rauniyar & Chou, 2019), (Majeed et al., 2019) (Ridolfi et al., 2019).

1.2. Problem statement

One of the main reasons why the SLM of metals has not yet been used extensively in the manufacturing industry is the lack of sufficient data to prove the consistent quality of manufactured parts. Currently, the cost of optimising the processing conditions to manufacture and qualify components is extremely high due to the extensive experimental research required to produce statistically convincing data for proving the repeatability and reliability of SLM (Shipley et al., 2018).

Mukherjee & DebRoy (2019) reasoned that using a digital twin for the 3D printing process would improve the quality of parts and shorten the time needed to qualify products whilst drastically reducing the cost of qualifying products. Although a digital twin will be ideal for determining the exact process parameters needed for the manufacturing process, the development of such a twin requires extensive work, as it includes a mechanistic model, a sensing and control model, a statistical model, big data, as well as machine learning to interpret the collected data. However, if a much simpler approach can be taken only to predict ideal process parameters, this would be very useful.

However, there is currently no known methodology to accurately and efficiently predict the ideal process parameters through modelling without the need for experimental work. Currently, systematic experimental methods are being used to determine these parameters (Shipley et al., 2018).

Gong et al. (2013) investigated the effect of various laser power and scanning speeds on the part porosity and surface finish. This research accurately determined a range of parameters for which fully dense parts could be created if the powder layer thickness and hatch spacing were kept constant. However, this research was also based on time-consuming, systematic experimental work. If a numerical model could be used to compare these experimental results with the melt pool characteristics, a possible range of preferred melt pool characteristics could be found, as was suggested by Gong et al., (2014). This information could then be extended to predict the process parameters for various other materials.

Significant literature concerning the development of numerical models for the SLM process already exists, while several other publications also focus on the directed energy deposition process. The work by Mukherjee et al. (2018) and Huang et al. (2016) are pertinent, as well as the work that was done by Luo & Zhao (2018). However, none of these numerical models focused on using the characterisation of the melt pool as a means to predict process parameters. As such, the need exists to investigate the possibility of characterising the melt pool through simulation to accurately predict process parameters that will yield high-quality components, thereby drastically reducing the cost of parts and qualification time.

1.3. Aim and objectives

The aim of this study was to demonstrate that, through numerical modelling and melt pool characterisation, processing parameters for the selective laser melting of the Ti6Al4V alloy can be predicted.

The aim was achieved through the following objectives:

- Create a numerical model of a single-track SLM process with existing commercial software, incorporating optimisation techniques found in the literature. This also has the added benefit of adding local expertise and capabilities.
- Validate the numerical model by comparing the melt pool characteristics with experimentally obtained results found in literature and through experimentation.
- Assess the obtained preferred significant process parameters for the SLM process of Ti6Al4V. Use these parameters in the numerical model to determine the melt pool characteristics and compare these results for various sets of process parameters. Find the range of melt pool characteristics for which high-quality parts are obtained.
- Expand the numerical model from a single-track model to a multiple-track, single-layer model.

1.4. Delimitations of the study

- Creating or editing the computer code of the simulation for increased accuracy was beyond the scope of this study.

- This study attempted to create a model accurate enough to predict process parameters. However, the level of accuracy was not specified as a required outcome of this study.
- Although the eventual goal was to be able to use this model for various materials, this study only focused on the Ti6Al4V alloy.
- Hatch spacing was not considered in this study, as this study focused on the cross-sectional geometry of single tracks.
- Modelling multiple layers of the SLM process was not a required outcome of this study.

1.5. Outline of dissertation

The first chapter of this dissertation indicates the benefits of a numerical model with sufficient accuracy to aid in the determination or optimisation of processing parameters such as laser power or scanning speed.

Chapter two provides an overview of the literature currently available on the subject, starting with a broad overview of the materials and process and moving gradually towards material that is focused on numerical modelling of the SLM process. The available literature on the specific material properties of Ti6Al4V used in the numerical model is also presented and critically analysed.

This is followed by a discussion in Chapter three of the methodology followed in this dissertation. This includes the methodology for both the experimental work conducted for the validation of results from numerical modelling and the process that was followed for setting up the numerical model.

In Chapter four of this document, all results obtained in this study are presented and discussed. Experimental results are presented first and are followed by a thorough discussion of the initial results from simulation, the effect of these results on the methodology of the study, refinement of the numerical model, and finally, a presentation and discussion of the final results from simulation.

In the last chapter of this dissertation, Chapter five, an in-depth look is taken at all the results obtained from this study and some conclusions are drawn.

Chapter 2 - Literature Study

In this chapter, an overview of insights into the topics related to this study gained from the literature review is presented. An in-depth look is taken at the SLM process, including its operation, limitations, the effect of process parameters on the built parts and common problems that arise when using incorrect process parameters. Thereafter, a review of the current state of the art of numerical modelling of the SLM process is given, and the current shortcomings are discussed. Lastly, information related to material properties for use in simulation is considered and assessed.

2.1. The SLM process

According to the ASTM F2792 standard, the SLM process can be classified as a laser powder bed fusion (L-PBF) additive manufacturing (AM) process applied to metals. This process is also referred to as metal laser sintering (MLS) or direct metal laser sintering (DMLS) (Sun et al., 2017). Although SLM can be applied to non-metallic materials, this section will discuss the L-PBF process for metals.

Before the SLM process can start, a 3D CAD model of the part to be manufactured is required. This CAD file is then saved as an STL file and computer software is applied to slice the model into individual 2D layers used to manufacture the part. A predetermined scanning strategy is employed to determine the laser scanning path for each layer. This information is then exported as a G-code file for use by the SLM machine (Gibson et al., 2015).

The SLM process starts with the placement of a substrate or baseplate for the printed material into the machine. This baseplate can be of the same material as the powder used in the process. A layer of metal powder is then deposited onto the substrate by a hopper or feed cartridge. After the powder has been deposited, a counter-rotating roller or recoater blade is used to evenly distribute the powder layer to the desired thickness (Gibson et al., 2015). In the EOS M280 system used in this study, the powder layer is spread onto the baseplate from the powder dispenser bin by a recoater blade. After the layer of powder has been deposited, the powder particles are selectively fused together and onto the

substrate according to the data obtained from the CAD model, using a high-power laser beam. The high-power laser beam moves along the top surface of the powder, heating it past its melting point and in the process creating a small pool of molten metal (Gibson et al., 2015).

As the laser traverses the powder, the molten metal solidifies again, forming a solid layer fused to the baseplate or the layer beneath it. After this process has been completed for the first layer, the substrate is lowered by the desired layer thickness. Thereafter, powder is deposited onto the fused layer, and the process is repeated until the topmost layer of the part being manufactured has been melted by the high-power laser beam. Various scanning patterns can be used to create solid parts (Gibson et al., 2015).

Fine metal powders have a high surface-area-to-volume ratio and are prone to oxidation. The elevated temperatures caused by the laser beam exacerbate this problem as elevated temperatures increase the rate of oxidation and create the possibility for certain materials, such as titanium, to react spontaneously with air. For this reason, the SLM process is conducted in an inert gas atmosphere circulated over the build area. For titanium alloys, argon gas is used for this purpose. The flow of inert gas over the powder bed also helps remove metal gas and condensate that can be produced during the melting process. The homogeneous flow of inert gas over the part being built, therefore, plays an important role in the final quality of the built part (Gibson et al., 2015).

2.1.1. The effect of process parameters

The SLM process is controlled by a large number of process variables. These parameters are also often interdependent. For this reason, it proves challenging to optimise the entire process fully (Gibson et al., 2015) (Shipley et al., 2018). However, the process parameters that play a role in the properties of the products produced by the SLM process have been well-categorised and are displayed in the diagram in Figure 2. The following subsections will be dedicated to discussing some of the process parameters mentioned in this figure and their effect on the final part.

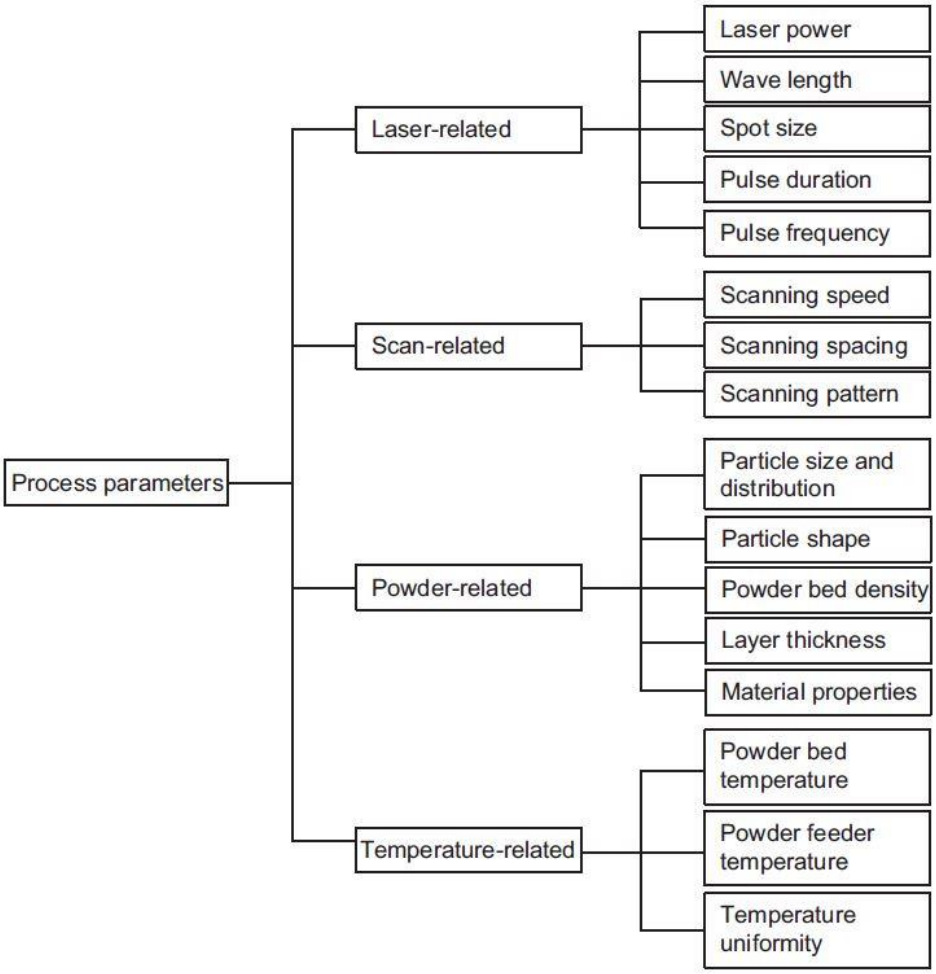

Figure 2: The various process parameters of importance in the SLM process (Sun et al., 2017)

2.1.2. Powder-related parameters and their impact

When discussing metal powders used in the SLM process, the particle size distribution and shape greatly affect the process as these variables affect the flowability of the powder, the absorption of laser energy and the thermal conductivity of the powder bed. This, in turn, affects the further selection of all other process parameters (Yadroitsev et al., 2021).

The particle shape and size distribution also greatly affect the packing density of the powder bed. Preferably, the powder bed should have a high packing density, resulting in reduced surface roughness and porosity, lower internal stresses and reduced part distortion. Powders with a wide distribution of particle sizes usually lead to greater packing density (Sun et al., 2017).

The flowability of powder is also affected by the particle size and shape, with spherical particles and larger particles improving the flowability of the powder. The flowability, in turn, affects the packing density of the powder bed, with a higher flowability of the particles increasing the density of the powder bed. For this reason, powder particles produced by gas atomisation are generally used as the feedstock material for SLM processes because gas atomisation produces particles with a spherical shape. In contrast, particles with a non-spherical shape tend to interlock mechanically. This leads to inhomogeneous packing density, adversely affecting part quality through porosity and lack-of-fusion voids (Sun et al., 2017).

Reduced particle sizes have both positive and negative implications on the process. Firstly, reduced particle sizes lead to an increase in the surface-area-to-volume ratio of the powder bed, which increases the absorption of laser power and increases the melt pool size and temperature. However, smaller particle sizes simultaneously heighten the chances of particle agglomeration and reduce the flowability of powder (Yadroitsev et al., 2021).

The effective thermal conductivity of the powder bed is affected to a greater extent by the packing density of the powder bed than by the thermal properties of the material itself. For this reason, particle size and shape have a great effect on the thermal conductivity of the powder bed. Since particles with a wide size distribution have greater packing density than spherical powders of equal size, they also lead to higher effective thermal conductivity in the powder bed (Sun et al., 2017).

Powder that is suitable for SLM consists of particles that are spherical in shape, have a low fraction of particles smaller than 2 µm, which can cause agglomeration, and no particles larger than 60 µm, which would increase the powder layer height beyond what is currently considered ideal for the SLM process (Yadroitsev et al., 2021). The powder layer thickness for SLM typically ranges from 20 µm to 150 µm (Gibson et al., 2015).

2.1.3. Melt pool properties and issues

Before considering the various process parameters influencing the melt pool and its geometry, some combined process parameters which collectively affect the melt pool can be defined. Taking the laser power (P), the laser scanning speed (v), the hatch spacing (h), the powder layer thickness (t) and the diameter of the laser spot at the surface of the powder bed (d), the following combined process parameters can be defined:

Volumetric Energy Density (VED): (Sun et al., 2017)

$$E_v = \frac{P}{v \times h \times t} \tag{2.1}$$

Linear Energy Density (LED): (Sun et al., 2017)

$$E_L = \frac{P}{v} \tag{2.2}$$

Surface Energy Density (SED): (Sun et al., 2017)

$$E_S = \frac{P}{vd} \tag{2.3}$$

The characteristics of the melt pool are discussed shortly, as well as the effect of process parameters on the characteristics of the melt pool.

- The temperature of the melt pool is affected by the laser power (P), linear energy density (LED) and laser scanning speed (v). Both an increase in laser power and linear energy density significantly increases the temperature of the melt pool, while an increase in scanning speed decreases the LED and thus its temperature (Li & Gu, 2014), (Yadroitsev et al., 2014), (Li et al., 2009).
- The temperature gradient within the melt pool is also an important characteristic to consider. An increase in applied laser power linearly increases the temperature gradient within the melt pool, and the lower the thermal conductivity of the powder bed, the higher the temperature gradient (Yadroitsev & Yadroitsava, 2015).
- Melt lifetime is defined as the period the melt pool exists at a specified position before it returns to its solid form. An increase in laser power and a decrease in scanning speed will both increase the lifetime of the melt pool (Yuan & Gu, 2015).
- Various factors affect the dimensions of the melt pool. An increase in laser power or LED will increase all dimensions of the melt pool. However, for increased LED, the effect on the width and height of the melt pool is more pronounced than on its depth. For an increase in scanning speed, an increase in the length of the melt pool and a decrease in its width were observed (Zhang & Coddet, 2016).

- It is also important to regulate the viscosity of the molten material in the melt pool, as too high a viscosity will prevent the material from spreading properly, while too low a viscosity will lead to the balling phenomenon that will be discussed later in section 2.1.3. Melt viscosity is influenced by material properties and melt pool temperature (Yadroitsev et al., 2010).
- Movement within the melt pool (melt flow) is predominantly caused by thermocapillary flow (the Marangoni effect). This is the result of the surface tension gradient due to the dependence of the viscosity of metals on temperature. The directional severity of flow is determined by the size and sign of the surface tension gradient of the melt. Flow is radially outward for most metals, but flow can move radially inwards under certain conditions. An increase in laser scanning speed and powder layer thickness increases the melt flow velocity. At too high laser scanning speeds, splashing of the melt pool can result (Yuan & Gu, 2015).
- The stability of the melt pool is of great importance for ensuring the quality of processed parts because instability in the melt pool leads to irregularities in the melt. This, in turn, can lead to surface roughness and porosity in finished parts due to balling or incomplete melting. The stability of the melt pool is affected by both the scanning speed and laser power, with a range of scanning speeds that result in a stable melt pool for a specified laser power. These ranges are material-specific (Yadroitsev et al., 2010). As the laser power increases, the range of stable scanning speeds increases, as seen in Figure 3. Materials with a high thermal conductivity result in a narrowing of this range.

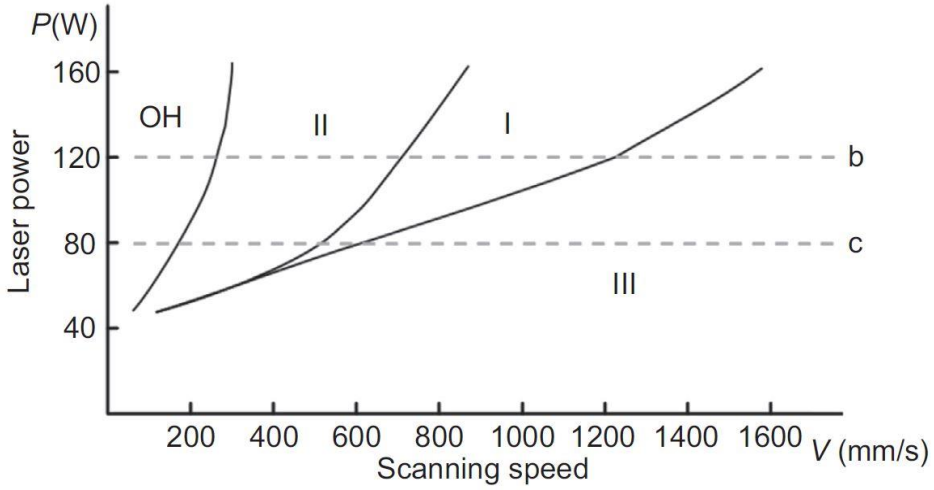

Figure 3: Effect of laser power and scanning speed on melt pool stability (Sun et al., 2017)

In Figure 3, Region I refers to a stable melting zone, creating fully dense parts. Region II refers to a region of over-melting, which leads to balling. Region III refers to incomplete melting, which leads to defects of irregular shapes and region OH refers to a region of overheating.

Balling of the melt pool

Figure 4: Incidences of balling of the melt pool due to too high scanning speeds (Li et al., 2011)

Balling in the melt pool is caused by molten tracks that shrink and form spheres to reduce the surface energy by reducing the free surface. The resulting track geometry from the balling effect can be seen in the upper track in Figure 4. Various factors contribute to the occurrence of this phenomenon. These factors include melt pool instability due to capillary and thermocapillary forces, melt pool splashing caused by the high surface temperature of the melt pool, high velocities in the melt pool, and high oxygen content in the atmosphere. Insufficient melting of the substrate due to high laser scanning speeds can also cause the balling effect. This is worsened by higher scanning speeds leading to melt-pool geometries with higher length-to-width ratios, which further increases the chances of balling. Balling can also be detrimental to the manufacturing process as the balling effect can obstruct the roller or recoater blade if the sizes of the balls formed are larger than the layer height (Li et al., 2011).

Keyhole mode melting

Under ideal operating conditions in the SLM process, the melt pool is formed in conduction mode. When the melt pool is in conduction mode, the heat transfer in and around the melt

pool is dominated by the conduction of heat from the heated surfaces to the bed. A melt pool created in conduction mode can be identified by its semi-circular shape, where the depth-to-width ratio of the melt pool is approximately equal to 0.2. The considered material may affect this ratio (Weckman et al., 1997).

However, the melting mode can be changed from conduction- to keyhole mode if the applied energy density exceeds 10^5 W/cm^2 (Rai et al., 2007). When the applied power density is sufficiently high, the metal is heated to such an extent that evaporation of the material occurs and a plasma forms. This superheated plasma results in an area of higher pressure, which acts on the surrounding molten metal and results in the formation of a temporary cavity in the melt pool. The evaporation rate of a metal also enhances the formation of this cavity. The formation of this cavity, in turn, enhances the absorption of laser energy. This causes the laser to penetrate much deeper into the material than what was possible in conduction mode melting. This deeper penetration is illustrated in Figure 5. For this phenomenon, King et al. (2014) defined keyhole mode melting as areas where the depth of the melt pool was more than half-width of the melt pool.

Keyhole mode melting has proven very useful in certain applications, such as laser welding, where deeper penetration is required. However, in the SLM process, the formation of keyholes is undesirable. This is due to the eventual incomplete collapse of vapour cavities that results in the formation of small voids in the final product, which increases the porosity of parts and reduces their quality (Sun et al., 2017).

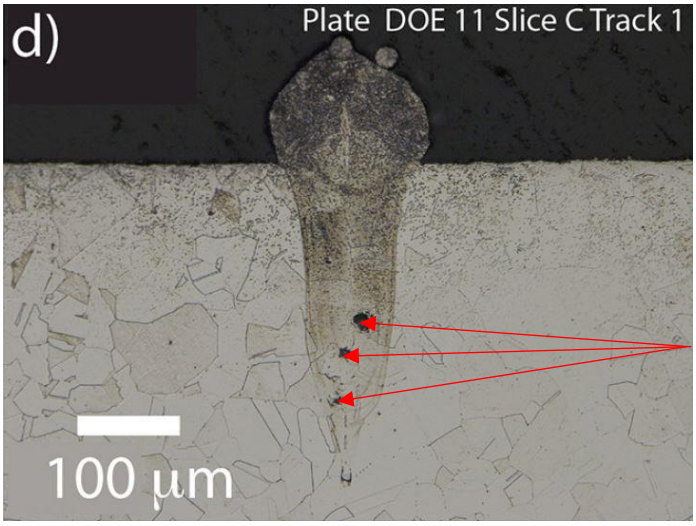

Figure 5: Cross-sectional view of the melt pool geometry in keyhole mode melting, showing keyhole-induced porosity indicated by the red arrows (King et al., 2014)

Le et al. (2019) focused on the numerical modelling of the keyhole melting mode and commented that it was challenging to model this phenomenon due to the change in absorption coefficient when the process enters keyhole melting mode. For this reason, Le et al. (2019) deemed it necessary to develop a ray-tracing model to model the process accurately.

2.1.4. Mechanisms causing melt pool instability

As mentioned in section 2.1.3, melt pool instability can be detrimental to part quality. These instabilities can affect both part density and surface finish. This section considers the mechanisms by which instability in SLM melt pools occurs.

Hydrodynamic instability in the melt pool is driven by the Marangoni effect. The Marangoni effect is the movement of a fluid caused by a gradient in the surface tension. For the SLM process, this surface tension gradient is caused by a temperature gradient in the metal and temperature-dependent surface tension of the liquid metal. This fluid movement is also referred to as thermo-capillary convection and has a greater effect on the melt pool when a higher LED is used. (Yadroitsev et al., 2010)

Capillary instability is a well-known phenomenon. Due to the surface tension of the liquid metal in the melt pool, the liquid metal will move to lower its surface area if the viscosity of the metal is low enough. As the viscosity of the metal decrease with an increase in temperature, the effect of capillary instability is greater at higher melt pool temperatures (Sun et al., 2017). This instability can cause balling of the melt pool as discussed in section 2.1.3, which affects the surface roughness of SLM parts (Attar et al., 2014).

Recoil pressure in the melt pool can also cause melt pool instability. This recoil pressure is caused by the evaporation of metal in the melt pool which results in increase of pressure in the region. This can have several effects on the melt pool. Firstly, this can result in melt pool collapse. This is the collapse of a keyhole melt pool on itself resulting in gas pores in the SLM part. Unsteady recoil pressure and melt pool collapse can also result in uneven penetration of the laser into the substrate (Kempen et al., 2015). In addition, recoil pressure can result in spattering, causing drops of molten metal to shoot out of the melt pool and affect surface finish if it lands in the build area (Simonelli et al., 2015).

2.1.5. Defects and density of SLM processed parts

Certain defects are likely to form when non-optimal process parameters are used in the SLM process. As mentioned previously, a wide variety of process parameters can be altered, and as a result, it is difficult to optimise the parameter set fully. Consequently, almost all components produced by the SLM process contain at least a small number of defects (Shipley et al., 2018). These defects include pores, lack-of-fusion voids and cracks that adversely affect mechanical properties, as discussed in section 2.1.6 (Sun et al., 2017).

Spherical gas pores can be formed when gas is trapped within the molten metal. The gas trapped in these pores usually comes from powder created by a gas atomisation process or the formation of moisture on the surface of particles. However, these pores can still be avoided by using the correct process parameters (Sun et al., 2017).

Keyhole pores can form when a too-high linear energy density is used, as discussed in section 2.1.5. This creates a deep and narrow melt pool that can collapse on itself to create this type of pore (Kempen et al., 2015)

Lack-of-fusion defects are the most detrimental to the mechanical properties of SLM parts due to their usually sharp edges. This type of defect is usually found between layers and is sometimes referred to as elongated pores due to its shape. Figure 6 compares the geometry of lack-of-fusion defects with that of gas pores (Weingarten et al., 2015), (Liu et al., 2014).

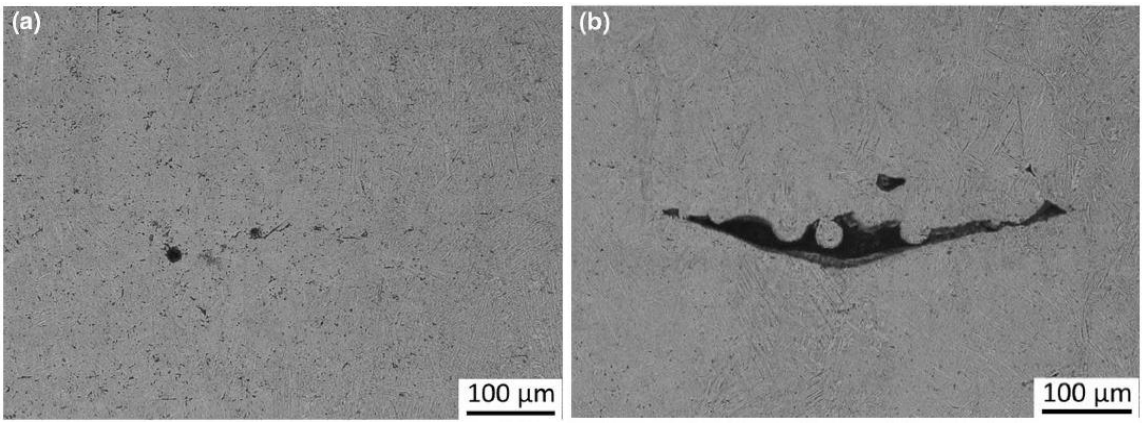

Figure 6: Comparison between a) gas pores and b) lack-of-fusion defects (Beese & Carroll, 2015)

The porosity or number of defects present in an SLM component was found to be strongly dependent on the LED of the process (Jia & Gu, 2014), (Zhou et al., 2016), (Harrison et al., 2015). Part density increases for an increase in LED up to an optimal LED value, where the relative density of the component is almost one. Upon further increase in the LED, vorticity in the melt pool drastically increases, having a detrimental effect on part porosity. For this reason, at a given laser power, the porosity of the final part is dependent on the laser scanning speed (Sun et al., 2017). This effect can be seen in Figure 7.

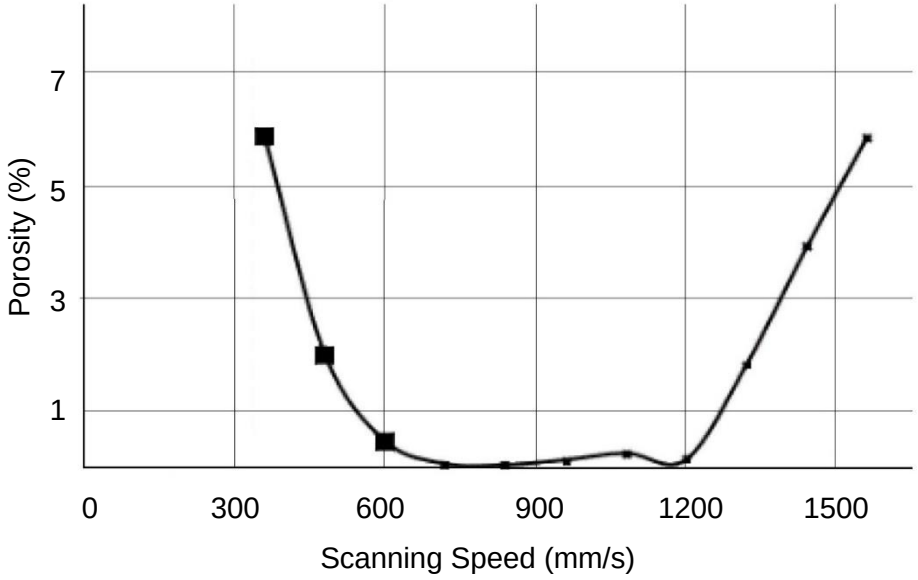

Figure 7: Effect of laser scanning speed on part porosity for a constant laser power of 120 W (Gong et al., 2013)

2.1.6. Influence of process parameters on the mechanical properties of SLM parts

A review by Sun et al. (2017) provided valuable information about the mechanical properties of parts produced by the SLM process. The review made a few interesting observations and is now briefly discussed. The mechanical properties of SLM parts show great dependence on the microstructure produced by the process, as well as the relative density of parts after production. Like the mechanical properties of cast materials, the ductility, strength and fatigue life of SLM-processed parts decrease with a decrease in the relative density of the parts caused by an increase of porosity in the parts. The strength, ductility and fatigue life are further reduced when the size of the pores exceeds the critical value for the specified material.

According to a study conducted on SLM samples of commercially pure titanium (Attar et al., 2014), the ductility and strength of the parts could be increased by increasing the laser power and the laser scanning speed while maintaining a constant energy density. In this study, the effect of higher laser power was attributed to resultant parts of higher relative density, while the effect of the higher scanning speed was the formation of finer martensitic microstructures. It was also found that pores and lack-of-fusion voids significantly affected the fatigue life of the parts.

Other studies found that the strength of materials (specifically aluminium and titanium alloys and stainless steel) produced by the SLM process was generally higher than the same materials processed by conventional methods. This was attributed to the high cooling rates in the process, causing fine, metastable microstructures (martensitic structures). Consequently, parts produced by the SLM process are generally expected to have much lower ductility than conventional components (Brandt et al., 2013), (Vilaro et al., 2011), (Facchini et al., 2010).

The fatigue properties of parts produced by SLM were found to be affected by multiple parameters. Firstly, the presence of defects greatly reduced the fatigue life of the parts (Leuders et al., 2013). Secondly, higher residual stresses within the parts lead to decreased fatigue life. The effects of residual stresses can, however, be mitigated by applying stress-relieving heat treatments to the parts after the SLM process (Edwards & Ramulu, 2014). The pre-heat temperature of the build chamber also affected the fatigue life of the parts. This was most likely due to reduced residual stresses caused by the elevated build chamber temperatures (Edwards & Ramulu, 2014).

Lastly, it was also observed that the build orientation was found to affect the tensile properties of as-built and annealed SLM parts. However, it was also concluded that the fatigue life of these SLM parts was not affected to a statistically significant degree by the build orientation but rather by the positioning of crack-initiating pores (Malefane et al., 2018).

From the abovementioned literature, however, it was observed that drawing general conclusions on the mechanical properties of SLM parts has proven to be quite a difficult task due to the considerable scatter of data caused by defects such as pores in the produced parts.

2.2. Determination of ideal process parameters

Some of the process parameters can be adjusted easily by the machine operator. The significant process parameters include the laser scanning speed, power, hatch spacing and powder layer thickness. These process parameters specifically affect the volumetric energy density (VED) and, therefore, the properties of the melt pool (Gibson et al., 2015). The VED is defined in Equation 2.1.

The effect of all of the parameters in Equation 2.1 on the stability of the melt pool, and therefore the quality of the final part, is well understood and has been discussed in detail in work by Gibson et al. (2015).

Gong et al. (2013) investigated the effect of laser scanning speed and laser power on the density of parts using systematic experimental trials. By varying both laser power and scanning speed and measuring the density of the parts obtained, they could identify a processing window in which fully dense parts could be created. A graphical representation of this processing window is shown in Figure 1. The process parameters used by Shi et al. (2019) confirmed these findings.

In the study by Gong et al. (2013), the authors found that the defects in Zone II were spherical, while the defects in Zone III were elongated and non-spherical. Further investigation indicated that the observed spherical porosity in Zone II was most likely caused by keyhole-induced porosity, while the defects in Zone III were caused by incomplete fusion of the powder particles and layers.

2.3. Computational fluid dynamics

When investigating the use of computational fluid dynamics (CFD) to predict process parameters for the SLM process, a basic understanding of CFD is required. This section aims to provide a broad overview of the CFD method and the methods of equations solved in the finite difference (FDM) method, specifically the finite volume method (FVM).

2.3.1. Conservation equations

Computational fluid dynamics refers to the process of numerically solving equations that govern the motion of fluid flow. These equations are often referred to as the Navier-Stokes equations or the conservation equations of mass, momentum, and energy. These conservation equations are incredibly versatile and can be used to predict fluid flow from

around an aeroplane to fluid flow in arteries (Moukalled et al., 2015). The conservation equations are given here:

Continuity or conservation of mass equation:

$$\frac{\partial \rho}{\partial t} + \nabla \cdot [\rho \mathbf{v}] = 0 \tag{2.4}$$

Where the symbol ρ denotes density and $\mathbf{v}$ the velocity vector.

Conservation of momentum:

This equation is derived from the principle of conservation of linear momentum and by application of Reynold's transport theorem,

$$\frac{\partial}{\partial t}[\rho \mathbf{v}] + \nabla \cdot \{\rho \mathbf{v}\mathbf{v}\} = \mathbf{f} \tag{2.5}$$

with the symbol $\mathbf{f}$ standing for the external force per unit volume.

Conservation of energy:

This equation is derived from the first law of thermodynamics, which states that the time-derived rate of change of total energy is equal to the sum of the rate of work done on the system by external forces and the change of heat content per unit of time. This equation has many forms since it can be written in terms of specific internal energy, specific enthalpy or total enthalpy. Based on specific enthalpy, this equation can be written as:

$$\frac{\partial}{\partial t}(\rho h) + \nabla \cdot [\rho \mathbf{v} h] = -\nabla \cdot \dot{q}_s + \frac{Dp}{Dt} + (\tau : \nabla \mathbf{v}) + \dot{q}_V \tag{2.6}$$

with the symbol h being the specific enthalpy, $\dot{q}_s$ the rate of heat transfer per unit area, Dp/Dt the rate of change of pressure and $\dot{q}_V$ the rate of heat source per unit volume (Moukalled et al., 2015).

2.3.2. The finite volume method

This method uses a numerical technique to transform the partial differential equations mentioned in section 2.3.1 into discrete algebraic equations to be solved numerically over finite volumes (cells) created during a meshing process which divides the control volume into smaller cells. This meshing process is similar to meshing in the FDM and FEM methods and discretises the domain into non-overlapping finite volumes. The differential equations can then be transformed into algebraic equations by integrating these equations over the finite volume. This then creates a system of equations that can be solved through iteration to determine flow variables, such as velocity components at different temperatures of the cells. In the FVM, some terms are evaluated at the boundaries of the finite volume cells by converting the terms to face fluxes (Moukalled et al., 2015).

Because of this, the FVM is strictly conservative. This property of the FVM has made this method the preferred CFD method to be used. Also, as the unknown flow variables are determined at the centres of the finite volume cells, various boundary conditions can easily be implemented using this method. Because of these characteristics and various improvements of this method since it was first used, the FVM has become a very powerful tool for analysing complex physics phenomena and their applications (Moukalled et al., 2015).

2.3.3. The volume of fluid method

When modelling fluid flow using the FVM, the boundaries of the fluid are usually predetermined by the boundary conditions selected in the pre-processor of the simulation software. However, when one of the boundaries of the fluid is a free surface, such as the interface between air and molten metal, the need arises to track the location and advection of this free surface so that boundary conditions, such as surface tension and or interaction with another fluid, can be imposed at the free surface (Griebel et al., 1998).

The volume of fluid (VOF) method is a numerical method used to determine the location and advection of the free surface of a fluid or the interface between two fluids. At its most basic level, the VOF method determines the free surface of a fluid by monitoring the fraction of the fluid in each mesh cell of the computational domain and reconstructing the surfaces in the cells where the fluid fraction is between zero (empty cells) and one

(completely filled cells) (Tryggvason et al., 2011). Numerous VOF methods exist, but the exact functioning of each of these methods falls outside the scope of this study.

Tryggvason et al. (2011) explain the VOF method in much more detail and highlight the differences between the various VOF methods and the advantages and disadvantages of each method.

2.4. Numerical models of metal additive manufacturing

Schoinochoritis et al. (2015) reviewed FEM models created to investigate metal AM processes. Thirty-five models were included in the review, and of these, seventeen were designed specifically to model the SLM process. The models reviewed were created for various purposes, but Schoinochoritis et al. (2015) divided them into three categories based on their focus. These categories were temperature fields, residual stresses, and melt pool characteristics. It was noted that almost all other literature related to numerical models could also fit into one of these categories.

Multiple new numerical models have since been created for various purposes. The aims and findings of some of these models are discussed now.

Wu et al. (2018) created a mesoscale model using the VOF method to study melt pool behaviour and showed the importance of modelling metal evaporation in the SLM process. Shi et al. (2019) used the Arbitrary Lagrangian-Eulerian (ALE) method to create a powder scale model to investigate the formation of microstructure in the SLM process.

Majeed et al. (2019) created a FEM model to predict the distribution of temperature and study the effect of the process on underlying layers. Le et al. (2019) studied keyhole mode melting in SLM by developing a ray-tracing energy source model. This model could predict porosity in parts produced by the keyhole melting mode.

Khairallah & Anderson (2014) created a mesoscopic scale model with random particle distribution to study the effect of a stochastic powder bed on the process and found that this had a profound effect on the process. This work was further improved by Khairallah et al. (2016), this time adding the Marangoni effect and recoil pressure during evaporation to demonstrate the importance of simulating these phenomena.

Zhuang et al. (2018) combined a FEM model with a Response Surface Methodology (RSM) process to determine melt pool parameters. This was done to investigate the effect

of process parameters, specifically laser power, scanning speed and hatch spacing, on the melt pool dimensions and temperature distribution within the melt pool. This work is of particular interest as it closely relates to the work laid out in this dissertation.

Cheng et al. (2019) studied melt pool process dynamics and pore defects using a CFD model created with the FLOW-3D simulation software. Interestingly, this study considered melt pool cross-sections and compared these to cross-sections obtained experimentally. The study concluded on possible mechanisms for the formation of keyholes but also noted that errors in the dimensions of melt pools ranged between 1,3% and 15,9% when compared to dimensions obtained from experimental work. These results seemed relevant when considering the aim of this study.

Chen & Yan (2020) developed a novel numerical model to study the mechanisms and effects of spattering and denudation. This was done by coupling an FVM and Discrete Element Method (DEM) model bi-directionally to simulate the movement of particles. However, only the solid and gas phases were modelled in this model. This was done as the addition of a third phase to the model would make the model computationally too expensive. The spattering modelled was, therefore, only the spattering of solid particles. They found that the vortex flow induced by the vapour jet was the main reason for the formation of denudation zones on the substrate. This was taken into consideration in the present study.

Rauniyar & Chou (2019), Du et al. (2019), Li et al. (2018a), Liu et al. (2019), and Mukherjee et al. (2018) created other numerical models of the SLM process found in previous literature. The aforementioned work is by no means an exhaustive list of numerical simulations created for the SLM process but rather a summary of work relevant to this study.

Review by Cook & Murphy

Cook & Murphy (2020) compiled a comprehensive review of available literature concerning modelling the melt pool in SLM. The review commented on the state-of-the-art at the time and progress, as well as the shortcomings of the literature. The software packages currently in use were also mentioned. A summary of the findings in the review is now given.

The review aimed to provide an overview of the state-of-the-art melt pool modelling in SLM and assess the different approaches taken to incorporate the modelled physical effects. This study also investigated literature concerned with keyhole laser welding due to its similarities to the SLM process.

In the review, the relevant physics was discussed, with emphasis placed on the approximations and simplifying assumptions used in the assessed models. Simplifying assumptions used in all numerical models included the assumption of purely laminar flow in the melt pool, temperature-independent viscosity of the molten metal and temperature-independent density of the molten metal. Various assumptions and models have also been implemented to approximate the thermal conductivity of the powder bed.

Many different approaches have been considered when modelling the transfer of power from the laser beam to the powder bed. Various studies modelled the powder bed as a continuum with effective thermal properties being applied to the continuum. In contrast, other studies modelled the individual particles, usually by applying DEM, simulating spherical particles of either identical size or with a simplified particle size distribution (PSD).

According to the review, a clear shift from continuum powder bed modelling to discrete particle modelling was observed over the previous years because the thermal conductivity of the powder bed greatly affects the development of the melt pool. However, treating the powder bed as discrete elements did not solve all inaccuracies, as non-spherical particles and particle sintering also greatly affect the conductivity of the powder bed.

Some studies also employed ray-tracing calculations to model the heating of the powder bed more accurately. These calculations are used to follow the path of the applied laser as it reflects multiple times in the powder bed or molten pool. Heat is then applied numerically to the cells in which the laser was reflected. However, very few studies have taken this approach.

Cook & Murphy (2020) also listed research groups focused on the development of numerical models to simulate the melt pool, the software packages these research groups used and the capabilities and limitations of those software packages. Limitations among almost all the software packages used included oversimplified assumptions to model the complex nature of the absorption of laser power in the powder bed, difficulties that arise from modelling vaporising liquid metal and its thermal effect on the system, as well as modelling the powder bed with sufficient accuracy. It was noted that despite all these assumptions and limitations, these research groups could still create models with impressive accuracy.

The software packages most often used in the reviewed literature included ESI ACE+, ALE3D, FLOW-3D, and OpenFOAM, as well as software of other research groups that had developed their own software packages. Other software packages, such as Ansys Fluent and COMSOL Multiphysics, have also been used. The benefits and limitations, as well as the possibility of using these simulation packages in this study, are explored under the section on the development of a numerical model in section 3.2.

Finally, in their review, Cook & Murphy (2020) discussed the general shortcomings of the reviewed literature that are worth noting here. Firstly, certain key items of information regarding the setup of the model, such as boundary and initial conditions, were often omitted, making the reproduction of the published work impossible. Secondly, the sensitivity of the impact of the mesh on the obtained results was rarely discussed. Lastly, they found the quality of work done to validate the accuracy of the models to be generally poor.

2.5. Material properties of Ti6Al4V for use in simulation

Bulk material properties for Ti6Al4V were provided with the FLOW-3D AM simulation software. However, all these material properties were selected from a single source (Mills, 2002). Furthermore, no temperature-dependent material properties were provided for temperatures higher than 2200 K, and for some material properties, no values were available for their liquid state.

As the saturation temperature (the temperature at which a phase changes from liquid to vapour, which is dependent on pressure) of Ti6Al4V is approximately 3300 K, it was decided to communicate with FLOW-3D on how the simulation software handles material properties outside the temperature range for which it is provided. The communications

confirmed that if temperatures were reached in simulations that were higher than the highest temperature for which material properties were specified, the last provided value would be used for calculations at higher temperatures. This then gives rise to a broad temperature range over which likely incorrect material properties are used.

Consequently, and to ensure that the accuracy of the model would not be affected by incorrect material properties, it was decided to thoroughly investigate the material properties of Ti6Al4V up to its saturation temperature.

All the material properties that were changed in the simulation software are discussed in the following sections. The original values presented by Mills (2002) were accepted for material properties not mentioned in these sections.

2.5.1. Surface tension coefficient and its temperature dependence

Various studies have been conducted on the surface tension of Ti6Al4V and its temperature dependence. Egry et al. (2010) found that the surface tension of a metal is very sensitive to any impurities, and a few parts-per-million (ppm) of oxygen could decrease the surface tension of liquid Ti6Al4V by several per cent. Sufficient oxygen content could also potentially reverse the sign of the temperature dependence of the surface tension. This is of great importance because the temperature dependence of surface tension is the driving force of Marangoni convection in the melt pool, which is essential for the accurate modelling of the melt pool (Tang et al. 2020).

Values of the temperature dependence of the surface tension of Ti6Al4V were found in several studies. These values, as well as the sources from which they were obtained, are presented in Table I. In this table, the surface tension coefficient (STC) refers to the dependence of the surface tension of the material on the temperature of said material.

Table I: Surface tension of Ti6Al4V according to various sources

Surface tension at liquidus temperature [N/m]	Surface tension coefficient (STC) [N/mK]	Source
1.389 ± 0.09	$-(9.017 \pm 0.56) \times 10^{-4}$	(Schneider et al., 2002)
1.52	-5.52×10^{-4}	(Aune et al., 2005)
1.49	-4.10×10^{-4}	(Aune et al., 2005)
1.52	-4.50×10^{-4}	(Aune et al., 2005)
1.52	-	(Vinet et al., 2004)
1.52	-5.52×10^{-4}	(Wunderlich R. K., 2008)
1.33	-3.6×10^{-4}	(Egry et al., 2010)
1.49	-4.1×10^{-4}	(Egry et al., 2010)
1.38	-3.13×10^{-4}	(Zhou & Wei, 2016)
1.493 ± 0.008	$-(1.9 \pm 0.5) \times 10^{-4}$	(Mohr et al., 2020)

For the surface tension at the liquidus temperature, most sources seem to correlate well with each other, except for the separate studies by Zhou & Wei (2016) and Egry et al. (2010). Upon further investigation, the study by Wunderlich (2018) was found to be from the same institution as that by Aune et al. (2005), and the same values were used again without further validation by Wunderlich (2008). The work done by Mohr et al. (2020) has a high degree of credibility, as it was done in microgravity aboard the International Space Station (ISS) and correlates well with the older results.

However, the value for the temperature-dependent coefficient of the surface tension (STC) is still very uncertain. This might be due to the varying oxygen content in the samples used in the various studies. The much lower value of this coefficient given by Mohr et al. (2020) could be due to a sample of higher purity being used. This is consistent with the observation by Egry et al. (2010) that impurities affected the temperature dependence of surface tension.

Taking everything into consideration, it was decided to use the value of surface tension of 1.493 obtained by Mohr et al. (2020) and an STC of -4.0×10^{-4}, which is an average of the results obtained from the various studies presented in Table I.

.

2.5.2. Density

The density of liquid Ti6Al4V was investigated in a study by Schmon et al. (2017). In this study, temperatures between 2050 K and 2590 K were measured. Figure 8 shows the different values of density of Ti6Al4V obtained in the literature.

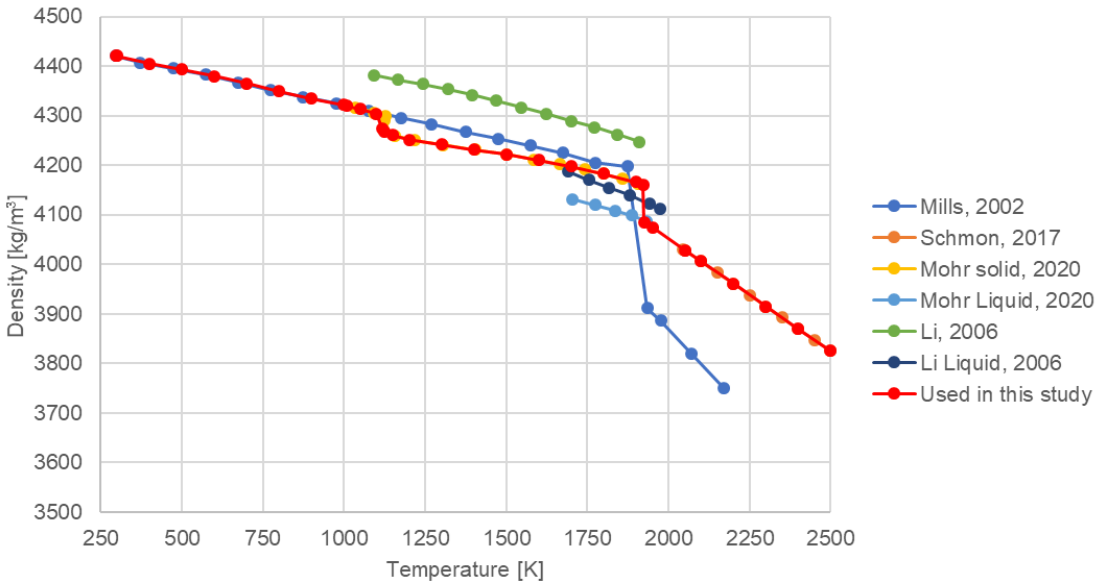

Figure 8: Temperature-dependent density of Ti6Al4V from various sources, as well as values used in simulations

Some values presented in Figure 8 were not given by the sources and were estimated through extrapolation to investigate the correlations of the different data sets. Values by Mills (2002), Mohr et al. (2020) and Li et al. (2006) were presented in graphical form in the original work and were analysed digitally using WebPlotDigitizer (Rohatgi, 2020) for comparison with values from the other sources.

From the values given in Figure 8, it is clear that the values by Schmon et al. (2017) and Mohr et al. (2020) for liquids correlate well at the melting point (1923 K) (within less than 1.5% of each other). It can also be seen that the separate values by Mills (2002) and Mohr et al. (2020) for solids correlate well at temperatures below the beta-transus temperature (1300 K).

Considering the aforementioned, the following information on density was used for the current study: The data obtained by Mills (2002) were used for temperatures between 273 K and 1000 K. The data collected by Mohr et al. (2020) was used from 1000 K to 1950 K.

From 2000 K to 2600 K, the data collected by Schmon et al. (2017) was used, and lastly, from 2600 K to the saturation temperature of Ti6Al4V, the data by Schmon was linearly extrapolated. The aforementioned data was the most accurate available at the stage of this study. This dataset is presented in Figure 9 and compared to data found in the study by Mills (2002) because the values by Mills (2002) are the default values loaded into FLOW-3D. The complete dataset can be found in Appendix A.

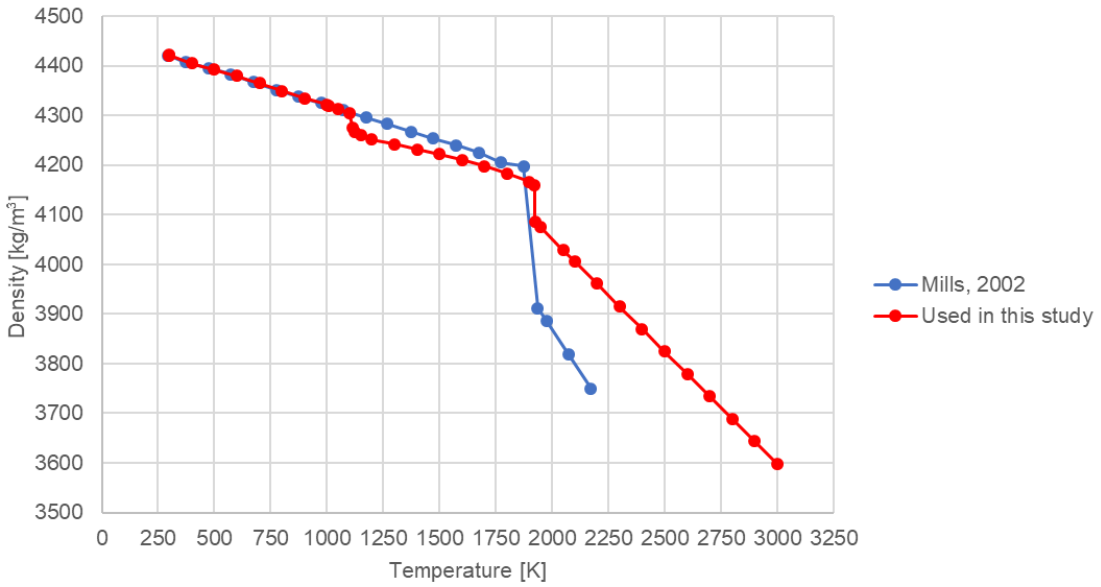

Figure 9: Comparison of the temperature-dependent density of Ti6Al4V according to the data by Mills (2002) in FLOW-3D and the data compiled from this study

2.5.3. Viscosity

Available experimental data on viscosity shows that the relationship between the viscosity and temperature of a material is non-linear and that viscosity decreases with an increase in temperature. Results obtained by Wunderlich (2008) demonstrated the effect of the concentration of oxygen in the Ti6Al4V on the viscosity of the liquid alloy, where a 0.05% increase in the oxygen content led to a doubling of the viscosity of the liquid at its liquidus temperature. From the results obtained in the literature, it became clear that measurement of this quantity was no easy task. Wunderlich commented in his work that the accuracy of the measured values of viscosity was ± 20%. Further investigation of these values also led to the investigation of the temperature-dependent viscosity of pure titanium. The results obtained from the various sources are represented graphically in Figure 10. The complete dataset can be found in Appendix B

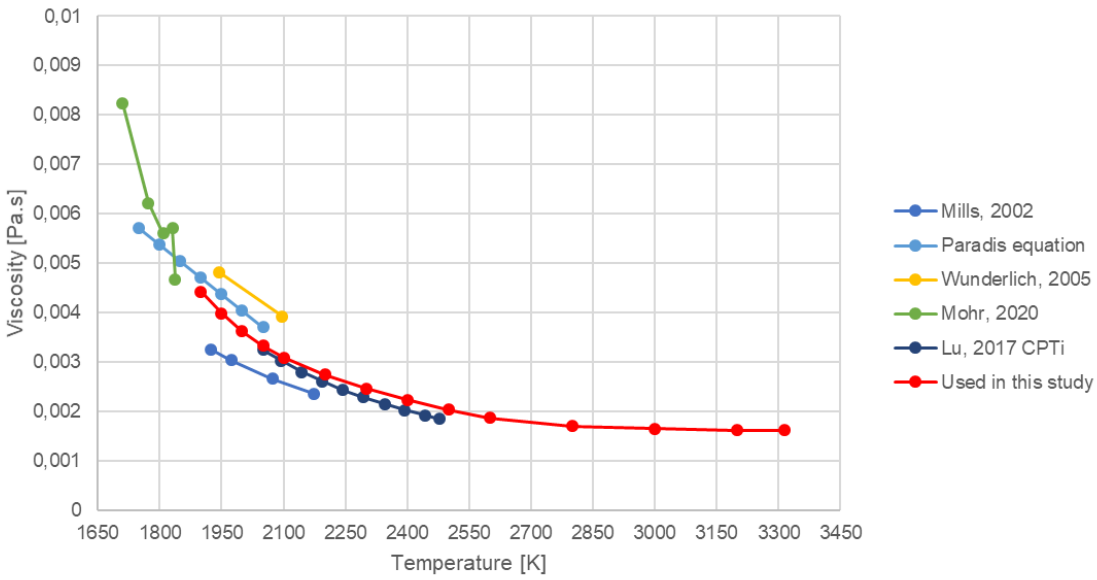

Figure 10: Temperature-dependent viscosity of TI6AI4V from various sources, as well as values used in simulations in this work

2.5.4. Convective heat transfer coefficient

This heat transfer coefficient (HTC) refers to the convective heat transfer coefficient between the bed molten pool and the atmosphere passing above it. In simulations, the air above the bed is simulated as a void with a constant convective HTC at the interface between the fluid and the air to increase computational efficiency. This is discussed in more detail in section 3.5.1.

According to Cengel & Ghajar (2015), the convective HTC of air on a surface ranges between 50 and 250 W/mK for the non-turbulent flow of the air. A value of 100 W/mK was recommended in documentation from the software provider. It should be noted that the assumption of slow-moving, non-turbulent air surrounding the build area is fair, while the air at the melt pool interface will most likely be very turbulent due to the fast and dramatic changes in the local air temperature.

To investigate the effect of this value on the results of the simulation, three simulations were run in the same way as described in section 3.5. All variables were kept constant except for the HTC, which was altered between 50, 100 and 250 W/mK. This was done with the optimal process parameter set.

From these simulations, only a very small difference in the temperature profiles of the different HTC values was observed and no change in melt pool dimensions could be seen. Consequently, no further investigation of this value was conducted, and a value of 50 W/mK was used in all simulations.

2.5.5. Thermal conductivity

The data by Mills (2002) provided values for the thermal conductivity of Ti6Al4V between 293 K and 2000 K. These values are presented in Figure 11. The values obtained by Mohr et al. (2020) and Boivineau et al. (2006), as well as by Milosevic et al. (2012), are also presented in this figure. From this graph, it is clear that the data from the first three sources for the thermal conductivity of Ti6Al4V in the temperature range 1300 K to 1800 K correlates very well. However, the data by Mills (2002) for the alpha + beta (1050 K-1300 K) phase and the liquid phase does not correlate as well over the temperature range shown in the figure. It should be noted that Boivineau et al. (2006) estimated the uncertainty of their measurements to be approximately 15%. According to Milosevic et al. (2012), the peak in their data at approximately 1280 K is due to the alpha-beta phase transition. Considering all these results, it was decided to use the values represented in Figure 11 in the simulations performed in the current study. The complete dataset can be found in Appendix C.

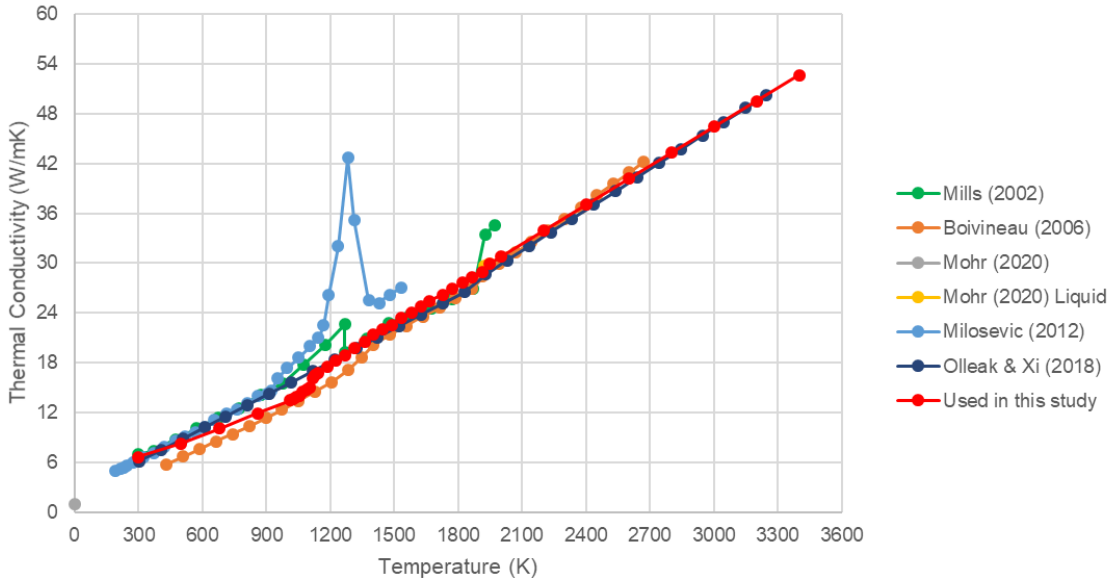

Figure 11: Comparison of thermal conductivity data of Ti6Al4V from various sources

2.5.6. Specific heat

When investigating the specific heat of Ti6Al4V, it was found that the results obtained by various studies vary significantly. For this reason, all possible sources that could be found were compared in an attempt to find the most accurate information. Information by Cezairliyan et al. (1977), Mills (2002), Kaschnitz et al. (2002), Basak et al. (2003), Boivineau et al. (2006), Milosevic & Aleksic (2012) and Mohr et al. (2020) were considered. The values obtained from these studies are visually represented in Figure 12.

The change in specific heat at approximately 1200 K is due to the phase change from the alpha to the beta phase. The values that were decided on were not based on a specific method but rather on the values where most sources correlated. This most closely relates to the values obtained by Milosevic et al. (2012) between 300 K and 1600 K and Mohr et al. (2020) for temperatures higher than 1600 K. The values for liquid Ti6Al4V obtained by Mohr et al. (2020) were for a subcooled liquid. The complete dataset can be found in Appendix D.

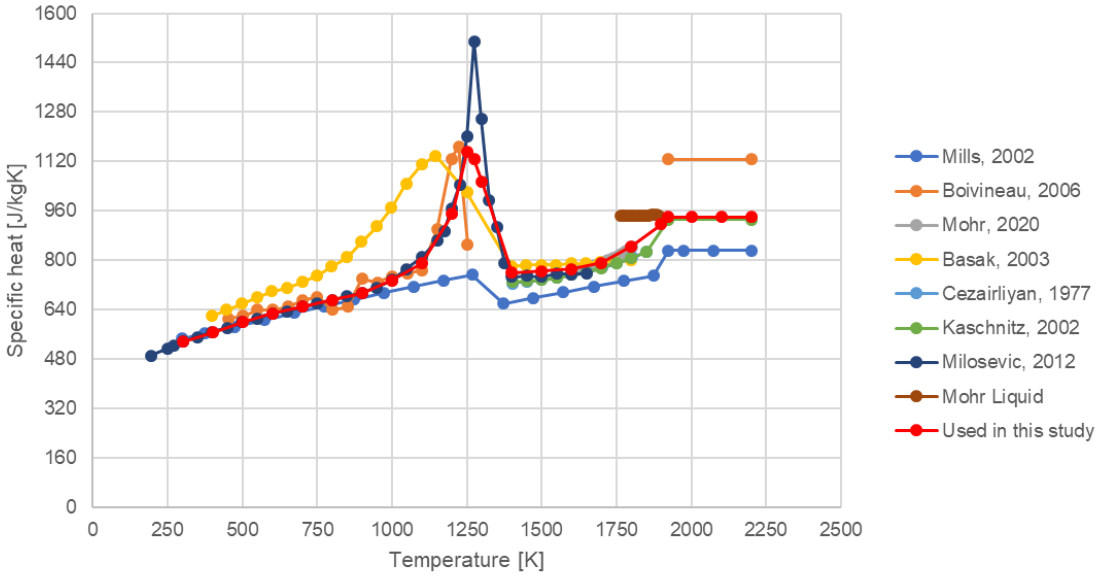

Figure 12: Temperature-dependent specific heat of Ti6Al4V according to various sources, as well as the values that were used in this study

2.5.7. Saturation temperature

In literature, it is widely accepted that the saturation temperature of commercially pure titanium (CPTi) is 3560 K. This value can be found on various websites and in some literature sources (Royal Society of Chemistry, n.d.). When researching the saturation temperature for Ti6Al4V, however, very little could be found in the literature.

The most reliable source found for Ti6Al4V was from a study by Rai et al. (2008), investigating the heat transfer and fluid flow of Ti6Al4V during the electron beam welding process, which led to a deep, narrow keyhole. This study referenced Smithells Metals Reference Book (Brandes & Brook, 1992) for a boiling point of Ti6Al4V of 3315 K at 100 kPa. As this was the only referenced value that could be found, this value was used in all the simulations in the current study.

2.5.8. Absorptivity

The values of absorptivity presented here are only of bulk material, due to the nature of the proposed CFD simulation with ray-tracing. Investigating the effective absorptivity of a powder bed was considered to be of little value to this study.

Various sources were considered to find the absorptivity of an Nd:YAG laser on a Ti6Al4V surface. According to Boley et al. (2016), the absorptivity is 0.39 for a flat surface and approximately 0.64 on a powder bed. This study considered pure titanium for the powder bed and baseplate. Schneider et al. (2002) considered absorptivity for laser drilling. In his study, a reflectivity value of 0.56 was used, resulting in an absorptivity value of 0.44 for pure titanium.

In another study, Xie et al. (1997) theoretically investigated the temperature-dependent absorptivity of pure titanium. They theorised that CPTi has an absorptivity of 0.26 at room temperature, which steadily increases to 0.43 at 1200 K, and thereafter remains constant. The same study also theorised that aluminium has a very low absorptivity coefficient (below 0.2). This could also possibly decrease the absorptivity value for Ti6Al4V.

A study by Lia et al. (2017) investigated the absorptivity of Ti6Al4V and Inconel 625 using the DED process. This study found an absorption coefficient for the Ti6Al4V bulk material of 0.51. This is much higher than the other sources found, and for this reason, it was not used.

Considering all these factors, it was decided to use a temperature-dependent absorptivity for Ti6Al4V very close to that found by Xie et al. (1997), as it correlates well with other studies. A slightly lower maximum absorptivity value of 0.41 was used to provide for the content of aluminium in the alloy.

Further investigation and simulation work, however, showed that the determination of an accurate absorptivity value for a liquid is no easy task because various parameters influence the effective absorptivity of the material, complicating the determination of the true value of absorptivity. This is discussed in more detail in section 4.3.1. It should be noted that the value settled on here was not used in all simulations since the obtained simulation results indicated that the credibility of these values could be questioned.

2.5.9. Accommodation coefficient

The accommodation coefficient is defined as a value that characterises the behaviour of gas or vapour particles in their collisions with a solid or liquid body surface. Pavlyukevich & Polezhaev (2011) noted that the presence of admixtures on the evaporation surface could affect the accommodation coefficient significantly. For pure titanium, the accommodation coefficient ranges between 0.5 and 1 for a temperature range of between 1600 K and 1800 K. Pavlyukevich & Polezhaev (2011) also noted that, at the time, it had not been observed experimentally with any accuracy that the accommodation coefficient was temperature-dependent. No information on the accommodation coefficient of Ti6Al4V could be found.

Lectures by the FLOW-3D software company noted that this value controlled the amount of evaporation occurring in the process. Software lectures recommended a value between 0.01 and 0.1, and a cautionary statement was made never to let this value exceed 1. However, it was unclear whether these recommended values were acceptable for any melt or were specific to a certain material or process parameter. Consequently, this value was experimented with in simulations and was not kept constant. The effect of this parameter on the results of simulation and related discussions can be found in sections 4.2.3 and 4.3.2

2.5.10. Gamma coefficient

In the setup of the simulations, the software required a gamma coefficient. Documentation included with the software indicated that the gamma coefficient is the C_p/C_v (specific heat) ratio. The gas used to fill the building chamber was argon baseline (pure argon). Therefore, the ratio of the specific heats of argon of 1.67 was used in the initial simulations (Engineering Toolbox 2003).

After consulting with a CFD engineer from FLOW-3D, it was found that the required value was the ratio of the specific heats for Ti6Al4V vapour. An experimentally obtained value could not be found anywhere, and it was inferred that this was due to the high temperature at which the vapour exists. The experimental ratio of specific heats for various other metals with low melting points was investigated to determine an approximate value. However, no study could be found in the literature that investigated this ratio for any metal.

Upon further investigation, it was found that this ratio theoretically remained constant for all monoatomic ideal gasses. (Safarian & Engh, 2012). Approximating Ti6Al4V vapour as a monoatomic ideal gas comprised of the three constituents, titanium, aluminium and vanadium, the value was the same as that of argon (Ford & Lee, 2001). For this reason, it was decided to continue using a value of 1.67. This value also correlated well with the values recommended by FLOW-3D.

2.5.11. Multiple reflections

It was noted in the documentation of the software provider that in keyhole mode melting, light reflects inside the keyhole, thereby increasing the energy density at the bottom of the keyhole. Moreover, the depth of keyhole mode melting is increased by activating the multiple reflection model, further noted in the documentation that the number of reflections in the model can be set in one of two ways: either by manually setting the physical number of reflections that are calculated for each time step, or by setting the attenuation rate for ending the reflections. With a constant absorption rate of 0.5, an attenuation rate of 0.01 will be reached after seven reflections, as observed in the documentation. Moreover, mesh size must be considered when multiple reflections are enabled, as each cell will only store one reflection vector.

When enabling multiple reflections in the software, there are three ways to calculate the amount of laser power absorbed. These are temperature-dependent constant absorption, angle-dependent absorption, and angle-dependent Fresnel absorption.

For temperature-dependent constant absorption, the rate of absorption is determined by the temperature and remains constant independent of the angle of contact with the surface. For this option, a table of absorption rates for various temperatures has to be entered into the simulation software. For angle-dependent absorption, the absorption rate is calculated using a cosine function multiplied by the maximum absorption rate, which must be entered into the software. All of this was noted in the software documentation.

According to Rai et al. (2008), this laser absorption coefficient is approximately 0.24. For the angle-dependent Fresnel absorption, the absorption is calculated using the Fresnel equation. Bergstrom (2008, p. 216) found that Fresnel absorption accurately represents the absorption of Nd:YAG lasers in titanium alloys. For this reason, it was decided to use Fresnel absorption for all simulations.

2.5.12. Hemispherical emissivity

This value was needed to account for radiative heat loss in simulations. Mohr et al. (2020) found that the total hemispherical emissivity of Ti6Al4V was 0.3 for solid Ti6Al4V and 0.32 for liquid Ti6Al4V. For this reason, it was decided to use an emissivity value of 0.32 for all simulations.

2.6. Summary

From the reviewed literature, a few observations can be made. Firstly, it is clear that there is already a good fundamental understanding of most of the process parameters that affect the SLM process and the varying degrees to which they affect the process quality.

It is also understood that the parameters that have the greatest effect on the process and, therefore, the quality of parts are the laser power and scanning speed used in the process, as discussed in section 2.1.3. There is also an in-depth understanding of the effect that varying these process parameters has on the melt pool stability, quality of parts, and mechanical properties of the parts.

From the observed literature in section 2.1.5, it is also clear that the mechanics for the formation of defects in single tracks that adversely affect the quality of parts have also been identified. These are weak penetration, balling and keyhole mode melting.

When investigating existing numerical models of the SLM process, it was interesting to note that numerous numerical models have been developed previously with varying degrees of accuracy. However, a review of SLM simulations by Cook & Murphy (2020) mentioned that studies regarding the accuracy of the models were lacking.

When investigating the material properties of high-temperature Ti6Al4V, multiple sources that investigated these material properties for the solid and liquid phases could be found, with the values presented by most sources being close to each other for most of the material properties. Two notable exceptions were the viscosity of liquid Ti6Al4V, for which no literature could be found that investigated the viscosity of the material in the temperature range of 2500 K–3315 K, and the absorptivity of Ti6Al4V, for which only very incomplete values of temperature-dependent absorptivity could be found.

The lack of material properties of Ti6Al4V in the gaseous phase was notable, although understandable, due to its high temperature. This led to several assumptions that were made for Ti6Al4V in the numerical model. These are discussed in section 3.5 in this document.

Chapter 3 - Methodology

The initial planning, as well as the challenges, alterations and final methodology of this study, will be discussed in this chapter.

3.1. Overview of the study

The first step in developing a numerical model that simulated the SLM process was the selection of a commercial simulation software package to be used. A discussion of how the software was selected is given in section 3.2. The software selected was the AM suite by FLOW-3D, supplied by Flow Science, Inc., Santa Fe, New Mexico, United States.

After the software was selected, the process parameters to be varied and the parameter sets that would subsequently be used in both experimental and simulation work were determined. The process by which these parameters were selected is discussed in section 3.3. The final selection of parameter sets that were used can also be found in this section.

Upon completion of the selection of process parameters, the experimental work required for the validation of the numerical model was performed. Experimental work was performed at the CRPM, which is proficient at using Ti6Al4V and possesses a broad knowledge of the optimal and non-optimal process parameters for Ti6Al4V. For this reason, Ti6Al4V was used for the experimental work in this study. Details of the preparation of the experimental specimens are discussed in section 3.4.

After cutting the Ti6Al4V substrate to obtain sections through the built tracks, as explained in section 3.4.2, the built single tracks and layers were analysed using optical microscopy. In these analyses, a micrograph of the cross-section of each of the single tracks and the single layer was recorded. For every single track, the following three measurements were taken: height of the melt pool above the surface, depth of the melt pool below the surface and width of the melt pool at the surface. The average, standard deviation and relative standard deviation (RSD) of each of these values were determined for each parameter set. A summary of the results from these analyses is presented in section 4.1. The complete datasets of these analyses are given in Appendix F and Appendix G.

After the experimental work was completed, a numerical model of a single track without powder was developed. The setup of this model is discussed in some detail in section 3.5.1, and more detail on how the model was set up with specific reference to the software is given in Appendix E. Upon successful development of the model, simulations were run for each parameter set. The results of these are presented in section 4.2.2. The methodology planned for simulations in this study is presented in Figure 13.

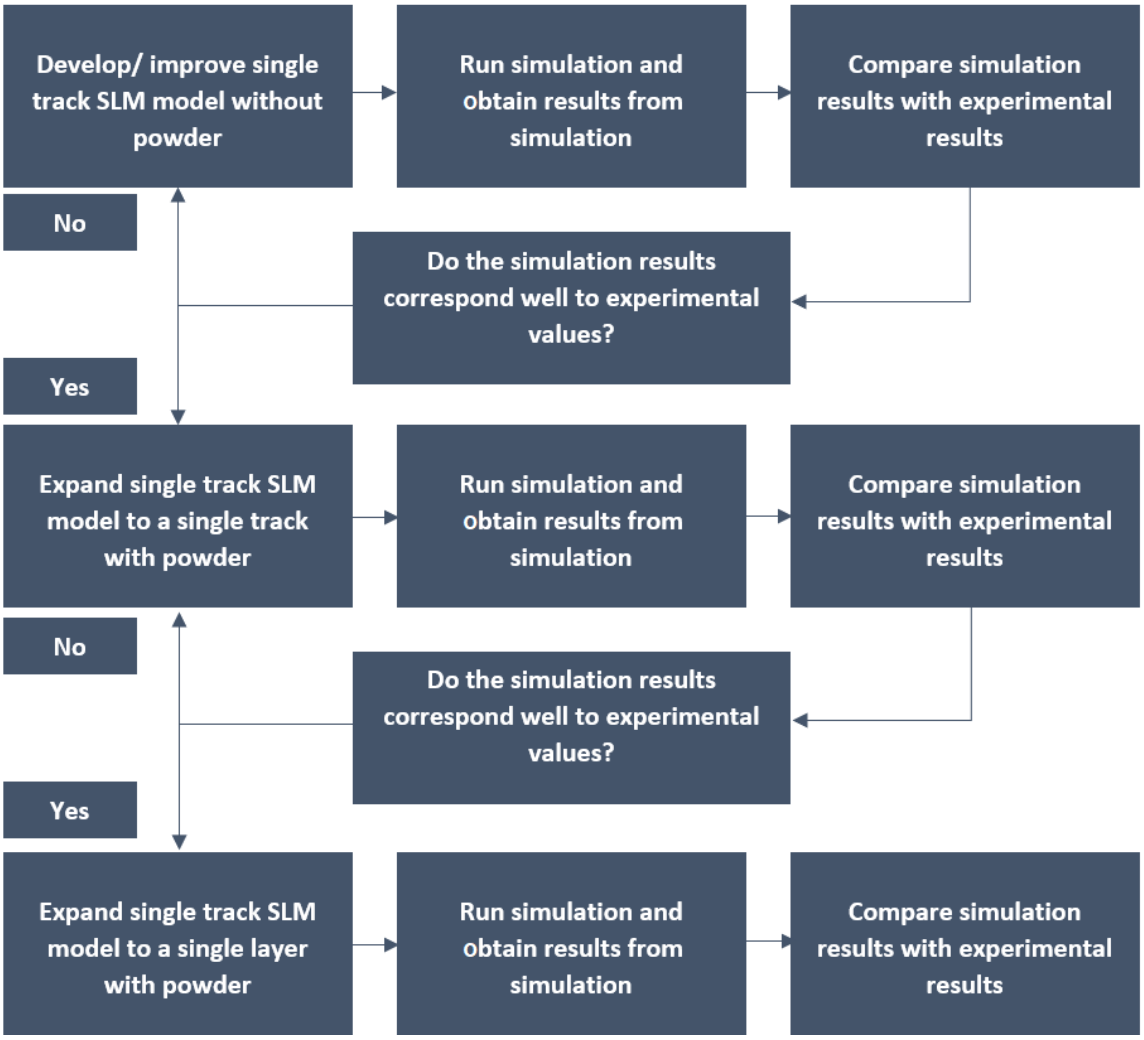

Figure 13: Planned methodology of this study

From Figure 13, it can be seen that a numerical model of a single track without powder was developed first, before creating a numerical model of a single track with powder. This was done to simplify the initial models and reduce the number of variables for the initial validation of the model, as adding a powder layer to the model adds significant variability to the model.

The results from these simulations were compared with the experimentally obtained results and found to be far too inaccurate to be usable. Various parameters that could be the reason for these inaccuracies were then identified. These parameters are discussed in section 4.3. After the parameters were identified, they were varied systematically in an attempt to obtain more accurate melt pool cross-sections.

After multiple attempts at obtaining simulation results that were close to the experimental results for all parameter sets by changing various simulation parameters, a further refined simulation set was obtained (see section 4.2.5). Although this simulation parameter set resulted in some improvement, input parameters that would yield results close to the experimental results for all parameter sets could not yet be obtained.

Although sufficiently accurate results could not be obtained at this stage to continue with the planned methodology as laid out in Figure 13, it was decided to continue with the simulation of single tracks with powder. This decision facilitated the possibility of analysing the capabilities of the software and determining other issues that could also inhibit the efficiency of using this simulation software to determine optimal process parameters accurately. In section 3.5.2, the process of developing a single layer with powder is discussed.

After the models with powder were created, the simulations were run, and the results with powder were compared to the experimental results. The results of these simulations are presented in section 4.2.9. Upon comparison of these results with the experimental results, it was found that further inaccuracies resulted from the way in which the powder bed was represented in the simulation. The reasons for these inaccuracies are discussed in section 4.3

Lastly, a simulation of a single layer with powder was created, and its creation is discussed in section 3.5.3. Because the dimensions of the melt pools for the other parameter sets were unsatisfactory, only the optimal parameter set was used to create a simulation for a single layer.

After all the simulations were conducted, conclusions regarding the strengths and weaknesses of using the FLOW-3D AM simulation software for predicting and optimising process parameters were drawn, followed by recommendations on areas of improvement and the way forward.

3.2. Selection of software

The first objective of this study was to create a numerical model of a single-track SLM process using existing commercial code. The selection of appropriate software for this task, to optimise chances of success, was done. In section 2.4, the software packages used in the literature for the numerical modelling of the SLM process were noted. These were ESI ACE+, ALE3D, FLOW-3D AM, OpenFOAM, Ansys Fluent and COMSOL. These software packages were selected based on their capability to model the fluid dynamics of the melt pool. Other software does exist that is only used to determine temperature profiles, which is not the focus of this study. The advantages and disadvantages of each software package suitable for the current study were investigated as now summarised.

The ESI ACE+ software is a multiphysics, high-fidelity simulation software package that supports various industries. A broad range of disciplines in physics, including heat transfer, biochemistry, electromagnetics, electrochemistry and many more, can be simulated simultaneously using this software. The software is versatile but normally requires high-performance computing (HPC) to solve complex problems (ESI, n.d.). Advantages of this software include the possibility to simulate the spreading of the powder bed, as well as the inclusion of the gas phase into the modelling (Cook & Murphy, 2020).

The ALE3D package is an arbitrary Lagrangian-Eulerian multiphysics simulation software developed by the Lawrence Livermore National Laboratory (LLNL) (Lawrence Livermore National Laboratories, n.d.). Compared to ESI ACE+, ALE3D has much more basic powder spreading capabilities but still has some DEM capabilities for simulating the creation of the powder bed. Advantages of this software include the linked Lagrangian particle movement. Gaps in the capability of this software include the fact that no mushy zone can be simulated during solidification (Cook & Murphy, 2020).

The FLOW-3D software is a multiphysics CFD software specialising in free-surface flow problems (FLOW-3D, n.d.). This software was originally developed for applications that required the VOF method. The AM package includes a DEM solver for the creation of a powder bed and a FLOW-Weld interface to simulate the interaction of a laser with the powder bed. The powder bed simulation capabilities are advanced when compared to other software. Cook & Murphy (2020) noted that a gap in the capability of this software was the ability to apply the heat of the laser only to the top surface of the powder bed.

The OpenFOAM package is a CFD software that is both free and open source. (OpenFOAM, n.d.) This software is a traditional CFD software solution and does not include any DEM functionality for powder bed simulation or multiphysics capabilities for simulating multiple laser reflections. As the source code for this software is available, it is possible to create sub-models for handling these phenomena, as has been done by Gurtler et al. (2013).

The Ansys Fluent software is one of the most well-known commercial CFD solutions (Ansys, n.d.). Since Ansys fluent is another classic CFD software solution, it has the same limitations as the OpenFOAM software. On this software's web page, limited DEM modelling capabilities are mentioned, but its use in literature for the creation of a powder bed could not be found. Furthermore, according to Cook & Murphy (2020), the models created with this software are incapable of movement of free surfaces and do not account for the effects of evaporative pressure. An advantage of this software is its advanced meshing capabilities.

Lastly, COMSOL multiphysics software (COMSOL, 2021) was considered. This is another very capable multiphysics software solution. However, according to the literature, the use of this software package is much more limited than the other software packages mentioned here. For the instances in the literature where this software package was used (Andreotta et al., 2017), the powder bed was modelled as a continuum instead of consisting of individual particles, no heat loss or pressure due to evaporation was modelled, and the movement of the free surface was modelled in a separate 2D model.

It should be noted that all the software packages mentioned are being further developed and that the information contained in this document might not be complete at the time of publication.

Considering the above-mentioned information, the final decision was between ESI ACE+ and FLOW-3D AM due to their enhanced capabilities, powder bed simulation capabilities and ease of use. Due to the existing literature on modelling the SLM process with the software ((Bayat et al., 2019), (Wu et al., 2018), (Liu et al., 2019)), as well as the supplier's favourable response, FLOW-3D was selected as simulation software for the current study.

3.3. Selection of process parameters

After the software selection was made, the process parameters to be used for modelling and experimental work were determined. As the focus of this study was to establish the ability to predict the optimal process parameters to be used, the model also had to accurately predict physical phenomena that would yield non-optimal process parameter sets so that these parameters could be ruled out.

Because this study aimed to predict these parameter sets using melt pool characterisation, process parameters that do not apply to single tracks, such as hatch spacing and powder layer thickness, were not considered.

As discussed in section 2.1.3, the two process parameters that affect the melt pool to the greatest extent are the laser power and scanning speed of the laser beam. Although parameters such as the laser spot size and frequency also greatly affect the melt pool, these parameters were not usually changed from those provided by the machine supplier and were, therefore, not varied in this study. For these reasons, it was decided to only change the laser power and scanning speed in this study. The combination of laser power and scanning speed will be referred to as a parameter set in the remainder of this document.

Examination of Figure 1 shows that there are three main reasons for the parameter set selected to be non-optimal. Firstly, when too low laser power is selected, the powder layer is not sufficiently melted. This results in lack-of-fusion voids when multiple layers are built. This parameter set will be referred to as the weak penetration parameter set.

The second reason for a parameter set to be non-optimal is a too-high energy density resulting in the melt pool transforming from conduction mode melting to keyhole mode melting. This results in gas pores in the final build. This will be referred to as the keyhole parameter set.

Lastly, if too high a scanning speed is used, this affects the stability of the melt pool and can result in build failure or lack of fusion. This will be referred to as the balling parameter set. These phenomena were explained in more detail in sections 2.1.3 and 2.1.5. After consultation with a machine operator at CRPM, the laser power and scanning speed for each parameter set were selected. A summary of the parameter sets and the laser power and scanning speed used to obtain these parameter sets are shown in Table II.

Table II: Laser power and scanning speed of the process parameter sets used in the current study.

Parameter set	Laser power [W]	Scanning speed [m/s]
Weak penetration	80	1.2
Optimal	170	1.2
Balling	350	2.0
Keyhole	340	0.6

The exact process parameters that were used, were obtained from well-established SLM process parameters within the CRPM. Local expertise for the specific material (Ti6Al4V) and powder that was used facilitated the accurate selection of optimal and non-optimal process parameters, as can be seen from the experimental results in section 4.1.

3.4. Experimental procedure

Experimental results for comparison with simulation results were obtained in four steps. First, planning the layout and conduction of the experiments. Second, the cutting of the built specimens into various smaller specimens. Thirdly, mounting, polishing, and etching of the smaller specimens and lastly, analysis of the geometry and characteristics of the single tracks and single layers created. The steps and procedures guiding the preceding processes are now discussed.

3.4.1. Layout of the experiments

When considering the layout of the experiments, a few important factors were taken into account. Firstly, sufficient single tracks had to be created for each parameter set to ensure that statistically relevant data could be obtained from each parameter set. Therefore, it was decided to create fifteen single tracks for each parameter set. The single tracks were created with a one-millimetre spacing in between to ensure they were far enough apart not to affect the geometry of the neighbouring melt pool but close enough to ease the mounting of the specimens. The layout of these single tracks and single layers is shown in Figure 14. In this figure, the large rectangles with the parameter set names inside them indicate the position of the single tracks. The small squares indicate the single-layer sample squares.

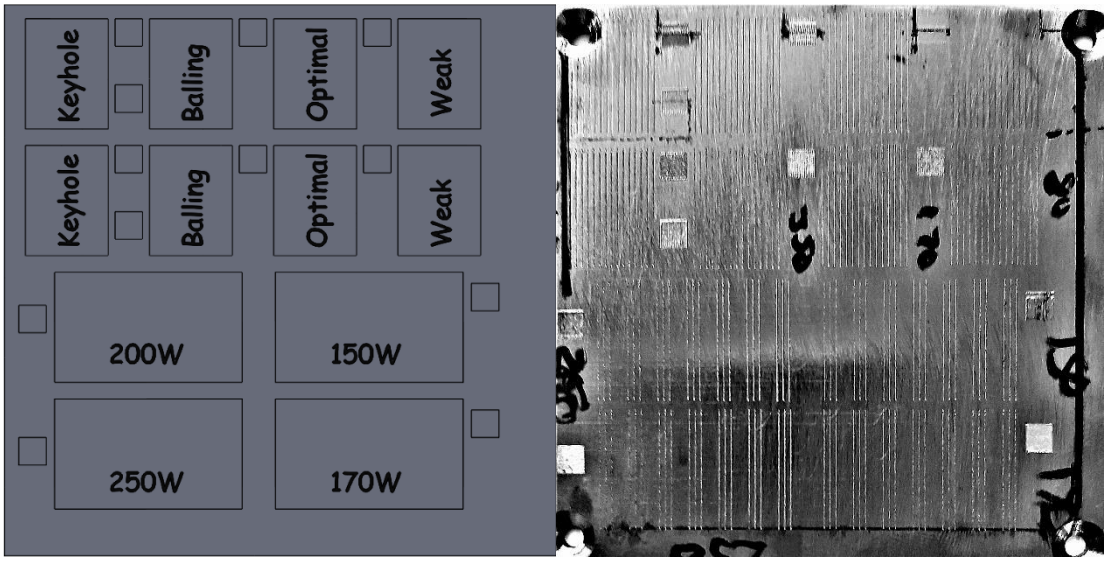

Figure 14: Diagram (left) and actual experimental layout (right) of the single tracks and single layers on the substrate

The second row of single tracks per parameter set, as shown in Figure 14, was identical to the first row of single tracks with the notable exception that the first row was created without powder, and the second row was created with powder. A feeler gauge was used as a reference to create a powder layer height of approximately 50 µm (± 10 µm).

As a single layer was also to be built in this study, this was done for all parameter sets. A five-by-five-millimetre square block of single tracks was deemed sufficient to obtain accurate and usable experimental results of single layers. A hatch spacing of 100 µm between tracks was used because this was the optimal hatch spacing for the optimal process parameter set. The small square blocks shown in Figure 14 are the single-layer areas. The single layers in the first row were created without powder, and in the second row with powder.

Finally, it was decided to create the bottom two rows of builds shown in Figure 14. These were to be used to provide additional information on the effects of varying laser power and scanning speed. The rows consisted of four blocks of single tracks, each created with a single laser power. For each block, the scanning speed was varied between 0.6 and 1.8 m/s, and three tracks were created with each set. These two rows of single tracks were both created with powder.

The experiments were conducted with an EOS M280 machine. This machine had an Nd:YAG fibre laser with a spot diameter of 80 µm. The substrate consisted of a 3 mm thick Ti6Al4V plate.

3.4.2. Cutting, mounting, polishing and etching specimens

After the experimental specimens had been built, the specimens were cut out through the substrate, and the relevant area for analysis of the melt pool cross-sectional shape and size was determined. Specimens were cut long enough to contain both the single tracks and single layer of a specific parameter set but short enough to still fit into the machine used for mounting the specimens into a resin.

Considering this, the specimens were cut, as shown in Figure 15. The green areas in this figure indicate the areas from which the specimens were cut. Red lines indicate single tracks that were created and red blocks indicate areas where single layers were created. This was done for the first and second rows of experiments. The specimens were cut at the Product Development Technology Station (PDTS) at the Central University of Technology, Free State, using submerged wire electric discharge machining (EDM).

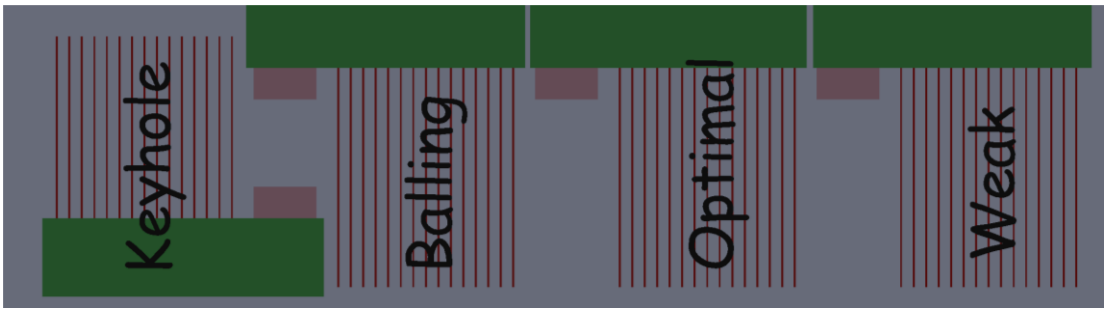

Figure 15: Schematic for cutting of specimens

After the specimens had been cut, they were mounted in clear resin in a Struers CitoPress machine. Thereafter, the specimens were ground and polished on a Struers Tegramin machine, using the pre-set grinding and polishing program for Ti6Al4V. Lastly, the polished specimens were etched using Kroll's reagent. The result of this process is demonstrated by the specimens shown in Figure 16.

Figure 16: Polished specimens of single-track builds without powder after mounting, polishing, and etching

3.4.3. Optical microscopy of specimens

After etching, each sample was investigated under a Zeiss Axio Scope.A1 optical microscope. An objective with 20x magnification was used for this. A micrograph was taken of each melt pool cross-section, resulting in 15 micrographs for each parameter set. This was done for the single tracks with and without powder, resulting in a total of 120 micrographs. At this point, various micrographs of the single layers with and without powder were also taken.

Upon the completion of this exercise, each micrograph was analysed, and three measurements were extracted from each. These were the width of the melt pool at the surface, the depth of the melt pool below the surface, and the height above the surface. The measurements were made digitally since the microscope was calibrated beforehand by Carl Zeiss (Pty) Ltd, the original supplier of the microscope. The length corresponding to each pixel was, therefore, known. Therefore, the number of pixels was determined for each micrograph and then multiplied by this calibration factor.

3.5. Development of a numerical model

The commercial FLOW-3D software AM suite was used to undertake simulations. Version 12.0 of the FLOW-3D software and version 11.2 of the FLOW 3D weld package were used for the numerical model. An Intel 10980XE processor with 128 GB of RAM was used for all simulations. Sections 3.5.1, 3.5.2 and 3.5.3 describe the procedures followed to set up the various models. These sections outline all process parameters that were used,

boundary conditions that were applied, physics models that were enabled and the reasoning behind them. For a complete guide on how this model was set up, with specific reference to the use and operation of the FLOW-3D AM software, the reader is referred to Appendix E.

Upon completion of the development of the various models, as well as a simulation run for the model, the built-in postprocessor of the FLOW-3D software was used to investigate a cross-section of the melt pool in the middle of the created track. FLOW-3D's built-in capability to determine melt pool width and depth was then used to extract this data from the completed simulation run and compared to the experimental data.

3.5.1. Development of a single-track model without powder

For the setup of the numerical model, the SI unit system was selected, the pressure type was selected to be absolute pressure, the reference pressure was set to 100 kPa and the reference temperature was set to 273 K. The completion time for each simulation was set according to the specific process parameters used. This was determined by the scanning speed and the cooling time for the specific process parameter set because time was allowed for solidification after printing.

Next, all physical phenomena relevant to this simulation were enabled. For this model, a single fluid simulation approach was selected. This meant that only the Ti6Al4V was fully modelled, with the atmosphere above the substrate being simplified substantially by only taking the temperature and pressure of the argon gas into consideration. Utilising this approach, no mass-, momentum- or energy conservation equations needed to be solved for the region where only argon was present, resulting in substantially reduced computational time. The volume above the substrate where argon gas was present will be referred to as the void to be consistent with the terminology used in the software. The model was set up assuming the incompressible flow of the melt.

The first model that was activated was the bubble and phase change model. This was done to account for the evaporation of metal during the SLM process. For this simulation, constant pressure bubbles with vaporisation were selected. The ratio of specific heats for the vapour was set to 1.66. The pressure of the void was set to 100 kPa. The convective heat transfer coefficient between the void and the metal was set to 50 W/m^2K, and the accommodation coefficient for evaporation was varied between simulations. The rationale for the use of these values was discussed in section 2.5.

Secondly, the function of evaluation of density was turned on in the software to account for the dramatic change in density of the printed material over the wide range of temperatures modelled. Volumetric thermal expansion was included in the simulation because the effect thereof on the simulation was unknown, and good information on the density of Ti6Al4V up to high temperatures was available in the literature (see section 2.5.2).

Gravity was then enabled and set as 9.81 m/s^2 in the negative z-direction (back into the melt from the void). Subsequently, heat transfer was enabled, and first-order fluid internal energy advection was enabled to simulate heat transfer through the substrate.

The next model that was activated was the solidification model. This model included various sub-models that could be activated, including the evolution of thermal stress, shrinkage, segregation of binary alloys, and microporosity. These sub-models were all left deactivated because their activation would add unnecessary complications to the model without adding to the accuracy of the model. It should be noted that some of these sub-models were developed for the simulation of metal castings and were, therefore, not all relevant to this study. The possibility of investigating the evolution of thermal stress is, however, an exciting possibility for future studies.

Following this, the surface tension model was activated, with the surface tension set to 1.493 N/m at a reference temperature of 1923 K (the melting point of Ti6Al4V). The temperature-dependence coefficient of surface tension was set to -0.0004 N/mK for the reasons outlined in section 2.5.1.

Lastly, the viscosity and turbulence model was activated. The simulation of viscous flow was also enabled. Various turbulence options were available, most notably laminar flow, k-epsilon turbulence and k-omega turbulence models. Upon investigation, it was found that most numerical models assumed laminar flow within the melt pool (Cook & Murphy, 2020). Some studies suggested that the flow within the melt pool during the SLM process could be quite turbulent, specifically for keyhole mode melting (Le et al., 2019). The relatively coarse mesh that was utilised was a concern, as a coarse mesh could result in inaccuracies when simulating turbulence (Argyropoulos & Markatos, 2015). However, since the melt flow was not being studied, and the only important parameter was the dimensions of the final melt pool, both laminar flow and k-epsilon turbulence models were utilised, and it was found that the effect of the turbulence model on the melt pool dimensions was negligible.

After activation of all the thermophysical models, the relevant temperature-dependent material properties were imported. These included temperature-dependent density, thermal conductivity, specific heat, viscosity and, in addition, solidus and liquidus temperatures. A discussion of the material properties used was presented in section 2.5. The complete datasets are given in appendices A to D.

Subsequently, the simulation domain was set up, and cell size selection was made. The setup of the mesh is given in Figure 17. A non-conforming mesh was used. To capture heat dissipation through the substrate but also model flow within the melt pool accurately, it was decided to use a mesh with various meshing planes, with the different planes denoting different cell sizes. If the cell size of two adjacent planes differed, the cell sizes in between were gradually increased from one plane to the next. This is illustrated in Figure 17. In this figure, thick black lines represent the different meshing planes, while the positioning of the individual cells is indicated by the thin blue lines. An example of the gradual increase in cell size between meshing planes is indicated within the red rectangle.

At first, a single cell size was used for the simulation when conducting the mesh dependency study. The results arising from this study are presented in section 4.2.1. This study concluded that a cell size below 7.5 µm was required and that a cell size of 5 µm would be optimal for the determination of the cross-sectional geometry of the melt pool. Consequently, it was decided to use a cell size of 5 µm for the innermost mesh planes.

Based on recommendations from the documentation of the simulation software, it was decided to use a cell size four times larger than the inner cells (20 µm) for the outer mesh planes to capture the diffusion of heat further away from the melt pool. This can be clearly seen in Figure 17. This figure shows the finer mesh in the innermost meshing planes and a coarser mesh along the edges to account for thermal diffusion. Also shown is the orientation of the axes in this figure for reference and arrows showing the directions of increasing mesh-refinement.

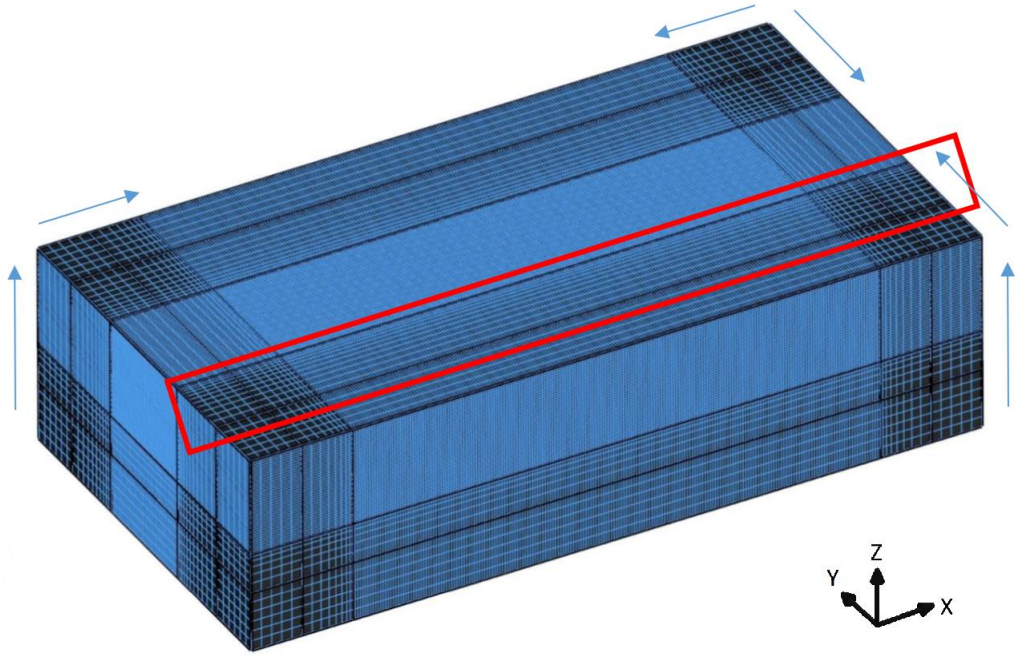

Figure 17: Graphical representation of the meshing of the simulation domain. The direction of the arrows indicates a decrease in cell size

For selection along the y-axis of the mesh, the recommendation in the simulation software documentation was used to create an inner mesh twice the width of the expected melt pool. This was equal to 400 µm for the keyhole process parameter set and 240 µm for all other process parameters. For the length of the melt pool, after initial simulations, it was decided to use a scanning track length of 1000 µm. This resulted in an inner mesh length of 1400 µm for the keyhole parameter set and 1240 µm for all other parameter sets.

Lastly, along the z-axis, only four meshing planes were used, as there was no thermal conduction to account for at the top of the domain. The inner mesh was extended 100 µm above the surface of the substrate, as well as 300 µm below the surface for the keyhole parameter set and 100 µm below the surface for all other parameter sets.

After the mesh was set up, boundary conditions were specified. The upper boundary was set up as a constant pressure outflow boundary at atmospheric pressure and a temperature of 293 K. All other boundaries were set up as walls with no in- or out-flow at a constant temperature of 293 K. This was done to most closely represent the physical reality. These were also the boundary conditions recommended by tutorials provided with the FLOW-3D software.

The initial conditions for the simulation were then specified. Initially, a fluid region was added to the mesh to define the region where the substrate was located. As almost the entire mesh consisted of the Ti6Al4V substrate, only a z-axis limit was introduced 100 µm below the top plane of the mesh. This was done to be able to simulate heat transfer between the substrate and the surrounding air, as well as accurately model protrusions of the melt pool above the surface.

The initialisation of these regions is graphically represented in Figure 18. After the fluid and void regions had been initialised, the initial temperature of both the fluid region and void region was set to 293 K, and the initial pressure of the void was set to atmospheric pressure.

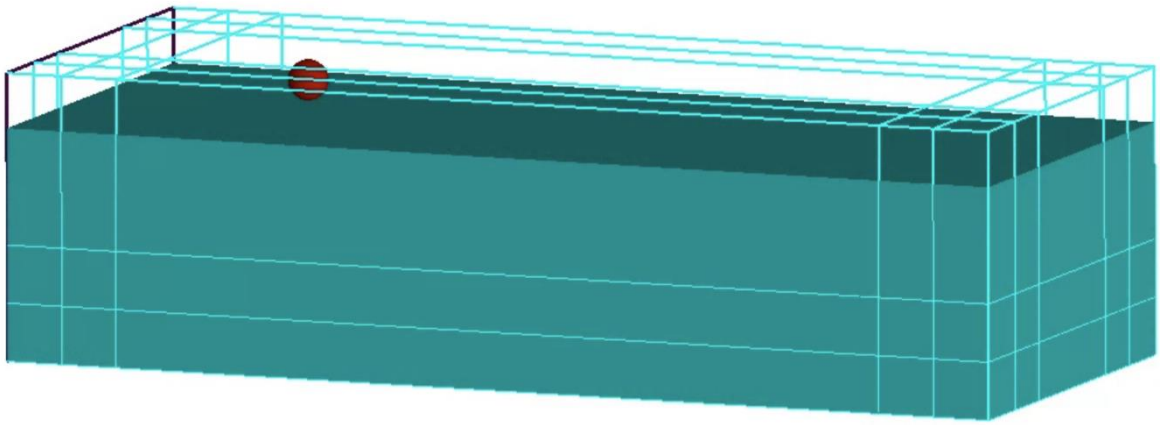

Figure 18: Initialisation of the fluid region (blue) and void region (open space), with meshing planes represented by the light blue lines

For the initial simulations that were run, none of the default parameters was changed. However, as certain simulation problems arose and interaction with a CFD engineer at FLOW-3D continued, some of these parameters were changed. The changes and reasoning behind them are discussed.

Firstly, the volume-of-fluid advection was changed from automatically determined to using the Split Lagrangian method. The Split Lagrangian method is an advanced VOF advection method that uses the velocity fields in the surrounding cells to more accurately determine the location and geometry of the tracked free surface. This change was not due to any errors but rather as a recommendation of a CFD engineer at FLOW-3D.

Next, the removal of isolated fluid droplets was enabled. This was done after the ejection of isolated fluid particles, also known as spattering in the SLM process, slowed simulations

substantially because the very high velocity of these particles lowered the convection stability time step limit, thereby increasing the simulation time. Therefore, a coefficient of 0.1 was used to remove these fluid droplets. This coefficient is dependent on the cell size used and was determined by trial and error.

By default, a dynamically adjusted convergence criterion was activated for pressure iterations. However, this led to large amounts of fluid lost through numerical processing for some of the initial simulations, specifically for those with higher pressure values, such as for the simulation of balling and keyhole process parameters. Consequently, this dynamically adjusted convergence criterion was changed to a constant convergence criterion of 0.1. This value was recommended in interactions with a FLOW-3D engineer.

Finally, the generalised minimal residual (GMRES) subspace size was changed for simulations where excessive pressure iterations took place from the default GMRES subspace size. This specifically took place for the simulation of keyholes with powder. The GMRES value was 15 by default for all simulations and was increased to 30 for the simulation of keyholes. This, however, increased the computation time required.

The settings for laser power and scanning speed were set up in a separate user interface, and the details for this setup are now given here. According to the EOS M280 user guide, the position of the laser beam source is 410 mm above the substrate. Hence, the position of the origin for the laser beam was set at the x- and y-values of the model origin and 410 mm above the model origin.

Next, the shape of the laser beam was defined as circular. The focal distance was set as 410 mm, the same distance as between the laser beam source and the substrate. Since there was no intent to study the effects of an unfocused beam, it was decided to keep the beam diameter at the lens and the focal point the same.

The spot diameter of the laser beam used in the experimental work was equal to 80 µm. This is effectively the $1/e^2$ diameter of a beam with a Gaussian distribution. This diameter of the beam is measured by finding the points in the Gaussian distribution where the relative intensity of the beam reaches $1/e^2$ or 13.53 % of the maximum relative intensity. The inflexion point was, therefore, set for a laser beam with a Gaussian distribution and $1/e^2$ diameter of 80 µm. A total beam diameter of 160 µm was modelled to account for the small percentage of radiation outside the $1/e^2$ diameter. The resulting heat flux applied to the domain with a cell size of 5 µm is shown in Figure 19.

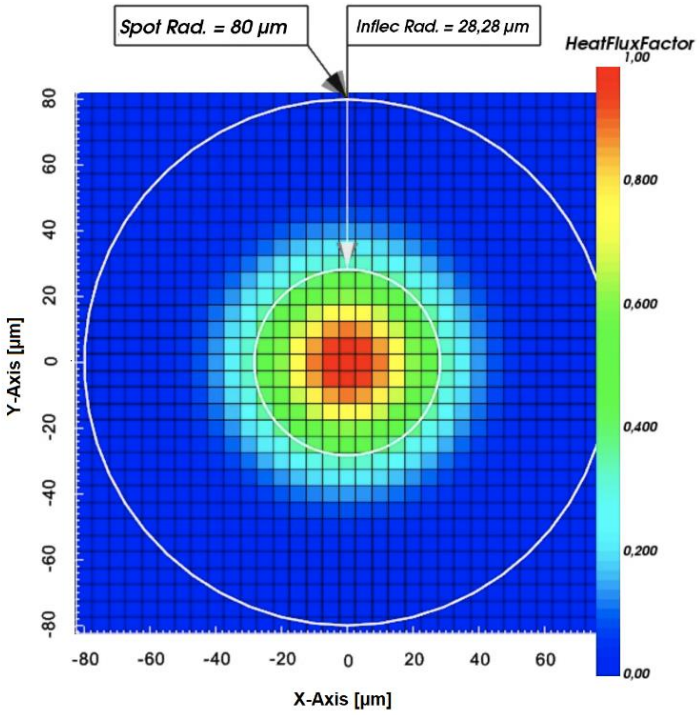

Figure 19: Heat flux distribution of the laser as applied by the simulation software on a mesh with a cell size of 5 µm

Because the simulation continued for longer than the laser was activated to allow for cooling and solidification, the time at which the laser had to be shut off had to be calculated. To determine this, the simple equation $t = s/v$ was used with the symbols *s* representing the displacement, *t* time and *v* the scanning speed. The value of time was different for every parameter set.

Lastly, the evaporation pressure coefficients were set. It should be noted that no literature could be found on the evaporation pressure coefficients to be used in simulations. Equations to estimate these values, however, could be found. The derivations of these equations are shown and discussed in some detail in section 4.3.2. The rationale behind the selection of values for the evaporation pressure coefficient can be found in the same section. The values of evaporation pressure used for simulations varied for various simulation sets. Therefore, these values are given in section 4.2, together with the relevant results.

3.5.2. Development of a single-track model with powder

Additional steps to those discussed in section 3.5.1 were required for the setup of a simulation with powder. Only the additional steps that were required in this case are

mentioned here, as all steps mentioned in the setup of the model without powder were still required for the model setup in this case.

The first step in creating a simulation with powder was the creation of the powder bed geometry. This had to be done as the FVM model does not have the capability of modelling the movement of powder particles. Therefore, the settling and spreading of powder particles had to be modelled using DEM, and the resultant geometry was imported into the simulation without powder. This was done by running two separate simulations. First, a simulation was set up where the particles were initialised mid-air and allowed to fall onto the substrate. Next, the results of this study were used as initial conditions, and a recoater blade was run over the powder bed to create a powder layer height of 50 µm.

This was done by creating a DEM simulation in the FLOW-3D software. In this simulation, mass particles were enabled. Seven species of mass particles were created to account for the PSD of the powder that was used. The sizes of the particles used are given in Table III. The particle sizes and concentrations used were obtained from (Thejane et al., 2017) – a study that characterised the PSD of Ti6Al4V powder, which was also applicable to the experimental work in this study.

Table III: Powder PSD and concentration used in the simulation software.

Particle Diameter [um]	Particle concentration [%]
12	1,8
16	11,2
19	21,7
23	31,1
27	19,9
32	11,2
37	3,1

The total number of particles was determined by running various simulations until a powder layer height of more than 70 µm was obtained, which was required for the particle spreading simulation.

Next, an STL file created in CAD software was added to the simulation for particles to settle on when falling. The resulting geometry can be seen in Figure 20. Subsequently,

the mesh was created inside which the particles were to be placed, and the simulation would take place. The mesh had dimensions 3600 x 760 x 300 µm, as shown in Figure 20.

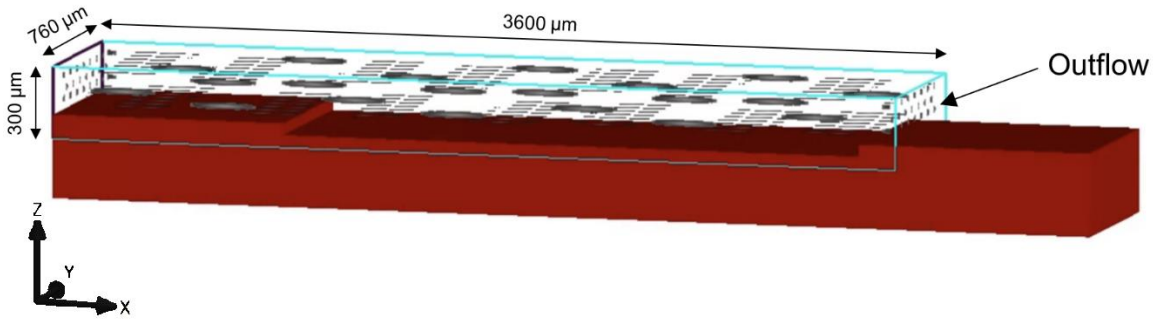

Figure 20: Geometry and mesh used for the particle-settling and particle-spreading simulations

The y-boundaries and x-min boundaries were set up as walls to prevent powder from flowing everywhere. The x-max boundary was set as an outflow. This was done so that particles could flow out at this end in the simulation that followed.

Lastly, the spring constant for the particles was automatically calculated using the software, and a coefficient of restitution in both the normal- and tangential directions of 0.3 was used according to the recommendations of FLOW-3D. A static coefficient of friction of 0.2 was used for both the particles and the walls, and a dynamic coefficient of friction of 0.15 was used, also according to the FLOW 3D recommendation.

This summarises the setup of the first simulation. After running the simulation, the geometry shown in Figure 21 resulted. The various particle diameters are indicated with a colour range, with red particles being the largest and dark blue particles the smallest particles for the range shown in Table III.

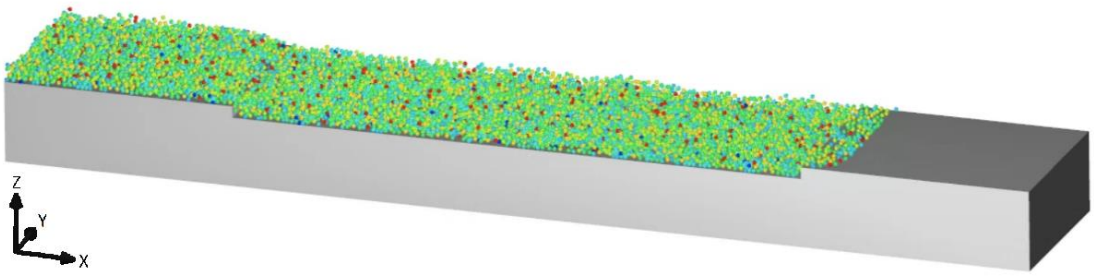

Figure 21: Resulting powder bed geometry after particle-settling simulation and before particle-spreading simulation

These results were subsequently used as initial conditions for the particle spreading simulation. For this simulation, a moving recoater blade that interacted with the particles was added. This recoater blade had a simplified rectangular geometry and was given a constant velocity in the positive x-direction. Lastly, the creation of new powder particles was disabled. After this, the simulation was run, and the results obtained are shown in Figure 22.

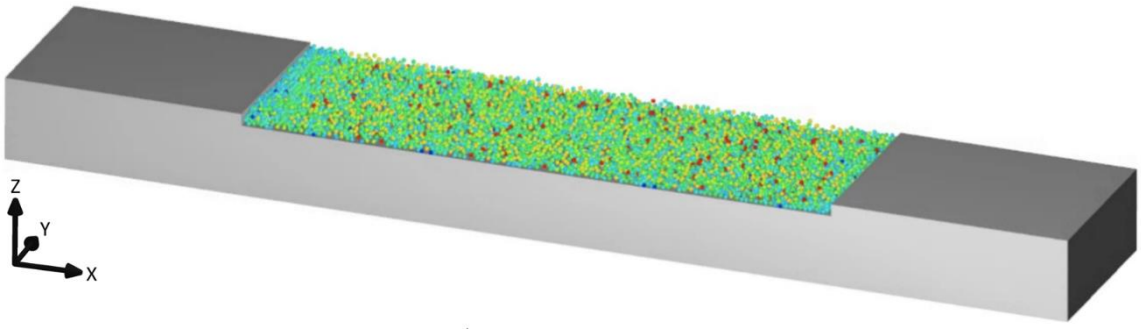

Figure 22: Resulting powder bed geometry after particle-spreading simulation

After this simulation was completed, the geometries of the particles were extracted from the simulation results file using the FLOW-3D Particle to STL converter. A magnified screenshot of the resultant geometry is shown in Figure 23. In this image, each major grid line represents 200 µm.

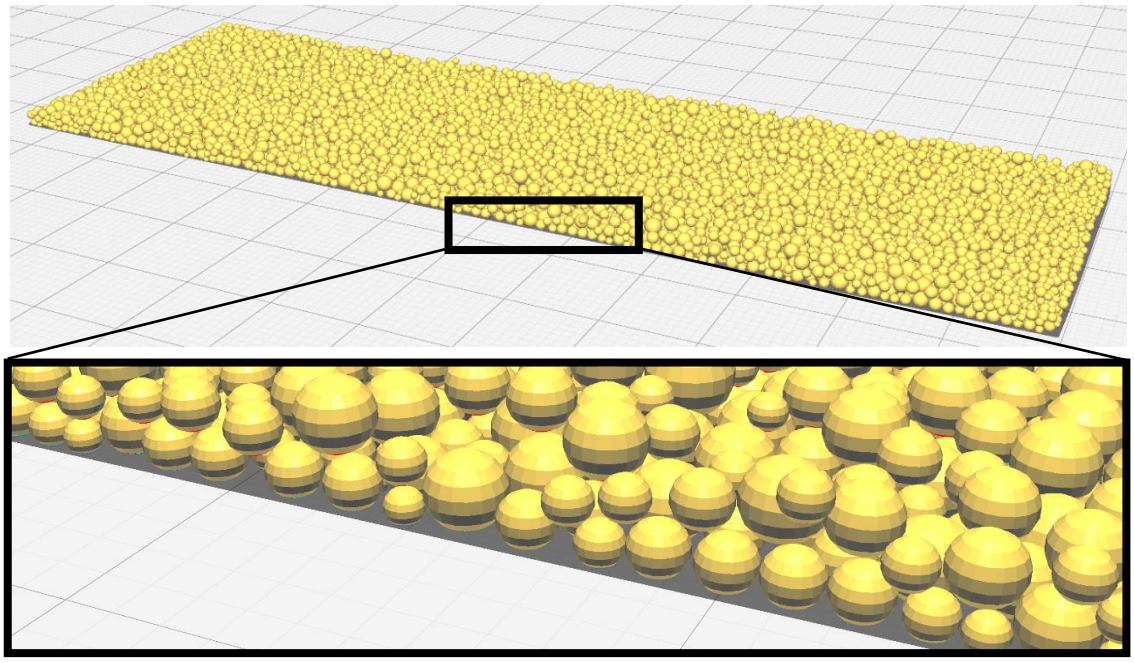

Figure 23: Screenshot of the resulting STL geometry after all particle simulations were completed

Subsequent to running these simulations and obtaining the powder bed geometry, the last step was to import the geometry file into a simulation without powder, setting the initial temperature to be the same as the substrate and lowering the substrate height by 50 µm. After these last changes were made, the simulations with powder were run.

3.5.3. Development of single-layer models

For the development of single-layer models, little additional setup work was required. The domain was enlarged in the y-direction, and a more complex x- and y-velocity profile was created for the laser beam. This velocity profile allowed some time for the first and second tracks to cool down before subsequent tracks were melted. This was done to represent the experimental creation of layers as closely as possible. A larger powder bed was also created in the same way as laid out in section 3.5.2. All other parameters remained the same.

3.6. Summary

Experimental specimens of single tracks and single layers were created on a substrate with- and without powder using a baseplate and powder of Ti6Al4V. The tracks and layers were created in an EOS M280 machine using four distinctly different process parameter sets. The specimens were cut, polished and etched using standard techniques for sample preparation. The cross-sectional geometry was then analysed and measured for each specimen using optical microscopy.

A numerical model using the same process parameters as those for building experimental specimens was then set up using the commercial FLOW-3D CFD software, utilising the VOF method to model the free surface of the melt pool.

Upon completion of the first set of simulations, it was observed that some discrepancies between the experimental and simulation results still existed. Possible causes for the discrepancies were investigated, and multiple changes were subsequently made to the existing model to improve the simulation results. The effect of these changes on the accuracy of the model was also investigated. The results of these changes are discussed in the following chapter.

Chapter 4 - Results and Discussion

In this chapter, all experimental and simulation results are presented and discussed. First, the results obtained from the experimental investigation of melt pool size are considered. This includes single tracks and single layers, with and without powder, for the various parameter sets. The obtained measurements of width and depth are then discussed, as well as the geometric anomalies of some of the melt pools observed during optical microscopy.

Thereafter, the various results obtained from numerical modelling are presented and discussed. First, the results from a mesh dependency study are presented, after which initial results of single tracks without powder are presented and compared to the experimental results. This is followed by sensitivity analyses of some of the modelling variables for which the input was unclear. Subsequently, a comparison between documentation by the software providers and other relevant literature to identify the use of the unknown modelling variables is presented. Following this, other results of single tracks without powder are presented and discussed. Thereafter, simulation results of single tracks with powder and single layers with and without powder are presented and discussed.

Lastly, the inaccuracies in the model are discussed. The possible reasons for these inaccuracies and their related simulation parameters are discussed. Possible solutions and alternatives are also examined.

4.1. Experimental results

4.1.1. Single tracks without powder

Table IV summarises the results of melt pool dimensions for the different parameter sets created on a substrate without powder obtained through optical microscopic analysis. The complete dataset can be found in Appendix F – Experimental results without powder. The results for each parameter set are discussed in detail here.

Table IV: Summary of melt pool dimensions for different parameter sets created on a substrate without powder.

Parameter set	Weak penetration	Optimal	Balling	Keyhole
Average depth (µm)	23,6	76,0	66,0	153,9
Standard deviation (µm)	0,80	1,49	2,49	67,7
RSD (%)	3,39	1,96	3,77	44,0
Average width (µm)	74.2	117,2	106,2	195,4
Standard deviation (µm)	2,42	1,65	1,52	9,11
RSD (%)	3,27	1,39	1,53	4,66
Depth/Width Ratio	0,32	0,64	0.62	0,78

Considering the RSD values presented in Table IV, it is clear that an RSD value lower than 4% can be expected with the stable creation of melt pools without powder. Values of RSD that are much higher than this likely indicate the unstable creation of a melt pool.

Weak penetration parameter set

Figure 24 shows the typical melt pool geometry created by the weak penetration parameter set.

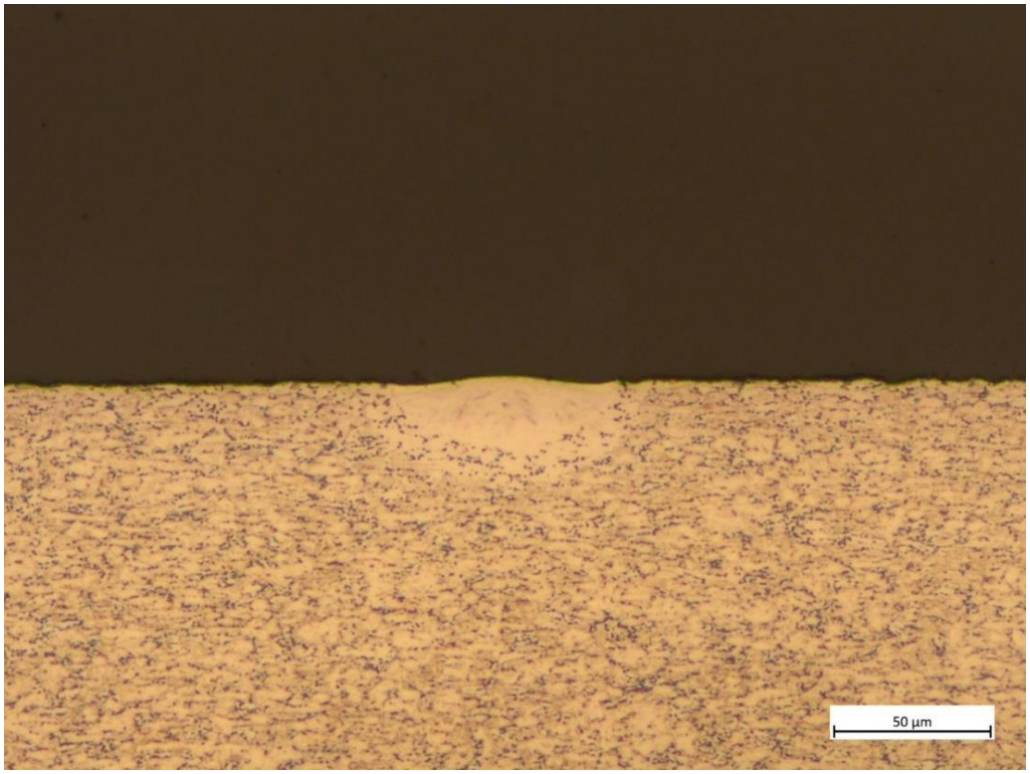

Figure 24: Typical cross-sectional optical micrograph of a melt pool created with the weak penetration parameter set in a substrate without powder

For this parameter set, all melt pools looked almost identical. The slight protrusion above the surface was quite interesting and was found for all parameter sets. The reason for this protrusion is unknown but could be due to a combination of the fluid flow within the melt pool and rapid solidification of the melt. The melt pools were relatively wide and shallow for this parameter set, with a depth-to-width ratio of 0.32, unlike the other parameter sets.

From Table IV, the average depth below the surface was 20.8 µm, and the average height above the surface was 2.8 µm resulting in an overall depth of 23.6 µm. An average width at the surface of 74.1 µm was observed. The standard deviation of the depth of the melt pool was 0.8 µm, and for the width of the melt pool, it was 2.42 µm. This translates to an RSD of 3.39% for the depth and 3.27% for the width of the melt pool, which implies that the creation of these melt pools was very steady.

Optimal process parameter set

Figure 25 shows the typical melt pool geometry resulting from the optimal parameter set.

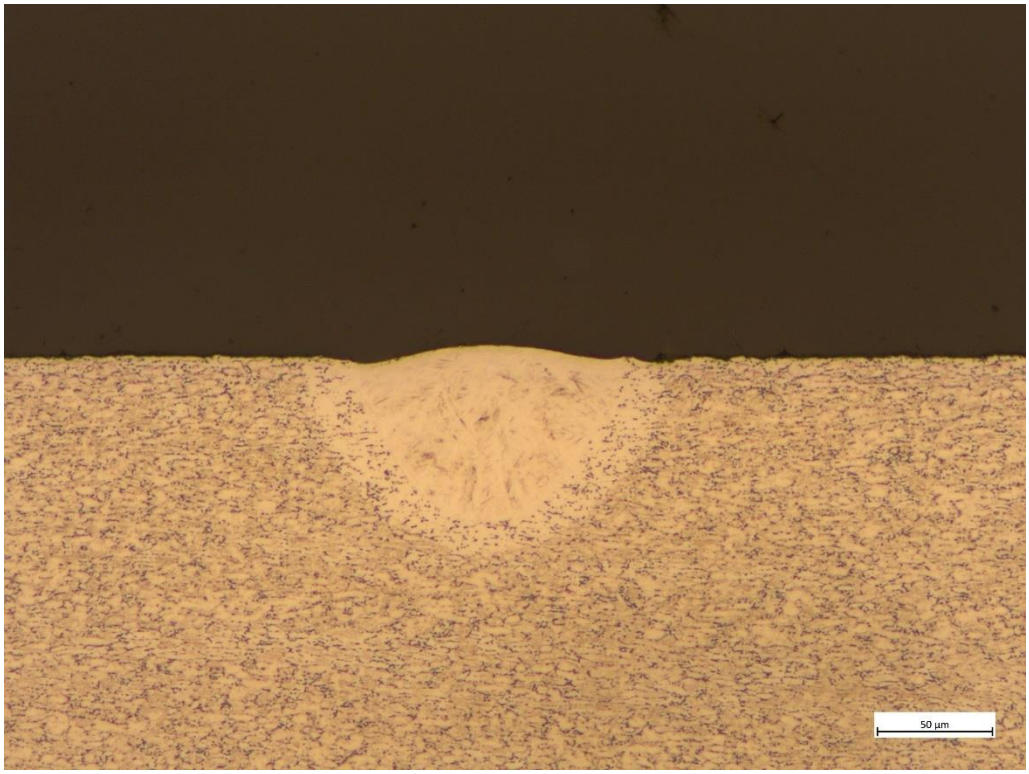

Figure 25: Typical cross-sectional optical micrograph of a melt pool created with the optimal parameter set in a substrate without powder

For this parameter set, only small variations were noted between the different melt pools that were analysed. As for the previous parameter set, the slight protrusion of the central part of the melt pool above the top horizontal level of the substrate is also evident here. The depth-to-width ratio of about 0.6 is very different to that of the weak penetration parameter set.

For the optimal parameter set, the average depth below the surface was 70.9 µm, and the average height of the melt pool was 5.1 µm above the surface, resulting in an average total melt pool height of 76.0 µm. The average melt pool width was 117.2 µm. As is shown in Table IV, a standard deviation of 1.5 µm for the depth and 1.6 µm for the width prevailed, with an attendant value of RSD of 1.96% and 1.39%, respectively. These values of deviation indicate the steady creation of melt pools. This also gives a good indication of the repeatability of the dimensions of the built tracks and the accuracy that is expected from simulations.

Balling parameter set

Figure 26 shows the typical melt pool geometry created using the balling parameter set.

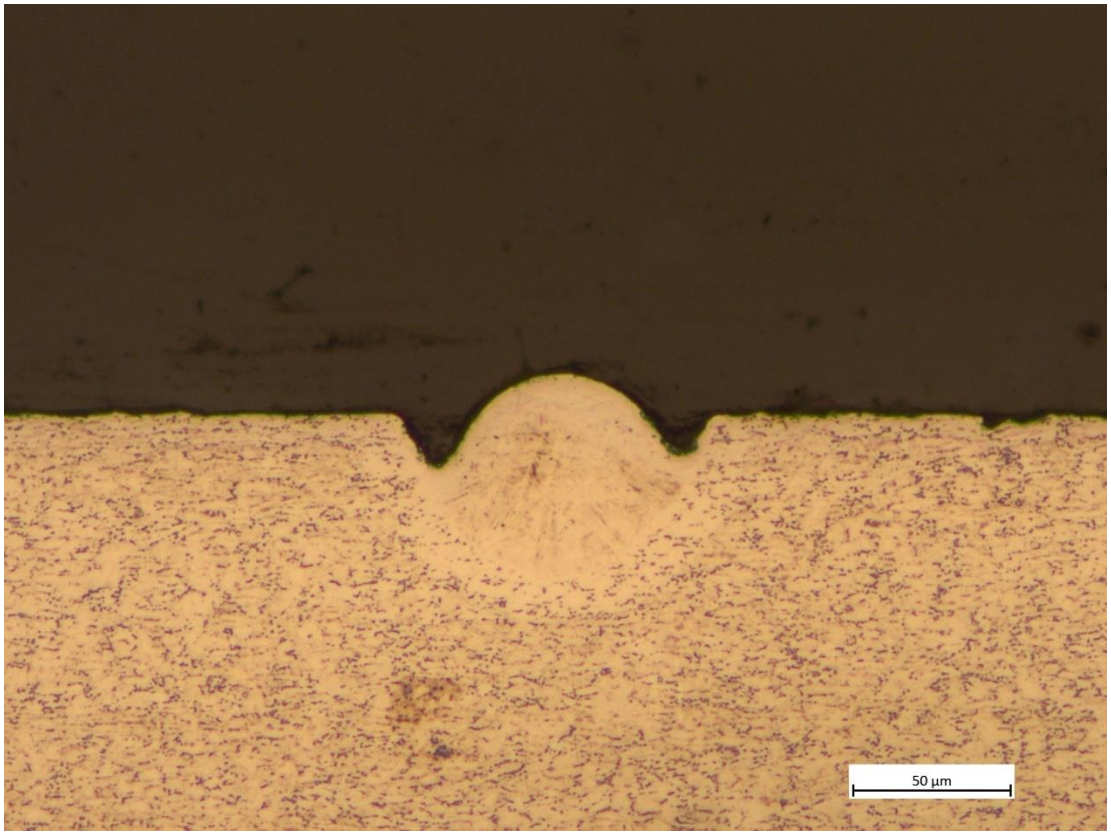

Figure 26: Typical cross-sectional optical micrograph of a melt pool created with the balling parameter set in a substrate without powder

Two significant features were observed for this geometry. Firstly, the very peculiar shape of the melt pool surface corresponds with the melt pool shape reported by Makoana et al. (2018) and Tang et al. (2020). This effect is referred to as the humping effect and is usually observed when a high laser power and scanning speed are used. Yadroitsev et al. (2021) proposed that the mechanisms by which humping occurs require further study. One study indicated that the Kelvin Helmholtz hydrodynamic instability could be the primary reason for humping (Kumar & Debroy, 2006), and another study found that a positive surface tension gradient contributes to this effect (Tang et al., 2020).

The second feature observed in Figure 26 relates to the overall dimensions of the melt pool. Comparing the dimensions of the optimal melt pool with the dimensions of the balling melt pool, the balling melt pool is 10 µm shallower, as well as 10 µm narrower. This was

unexpected because the linear energy density, $E_L = P/v$, was 23,5% higher for the balling parameter set than for the optimal parameter set.

The depth of the melt pool below the surface was, on average, 51.9 µm and the height above the surface, on average, 14.1 µm. This resulted in an average total height of 66.0 µm. The average width for this parameter set was 106.2 µm, which resulted in a depth-to-width ratio of the melt pool of about 0.6. The melt pool dimensions were once again consistent, with an RSD of 3.77% for the depth and 1.53% for the width.

Keyhole parameter set

Figure 27 shows examples of the cross-sectional geometries obtained from the keyhole parameter set. Since the geometries of the melt pools varied substantially, micrographs of the different geometries are shown.

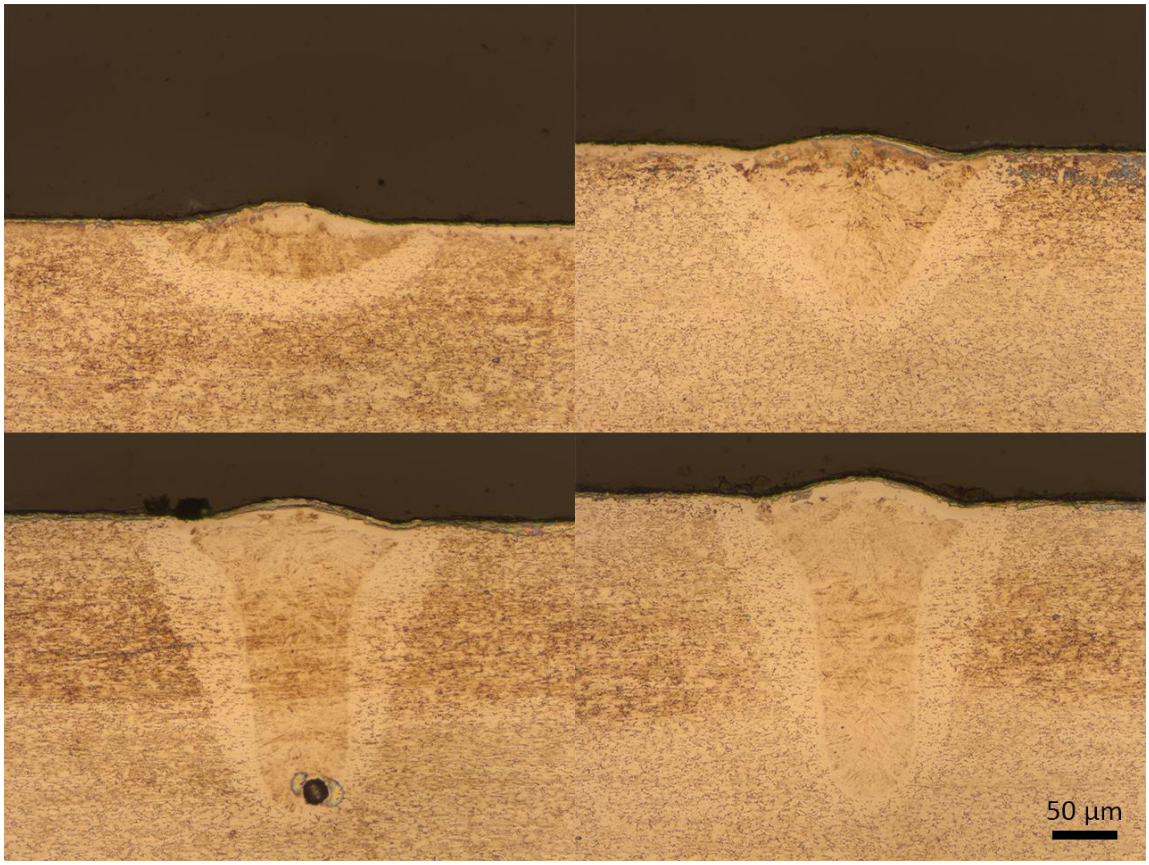

Figure 27: Cross-sectional optical micrographs of various melt pool geometries obtained with the keyhole parameter set in a substrate without powder

From these results, it became clear that the melt pool dimensions for this parameter set were very inconsistent and that the creation of the melt pool was inherently unstable, fluctuating between conduction mode and keyhole mode melting. Interestingly, however, was the consistency of the width of the melt pool when compared to the depth in the keyhole mode. From Table IV, the RSD of the depth of the melt pool was 44.0%, while the RSD of the width was only 4.66%.

When analysing the dimensions of these melt pools, the average depth below the surface was 138,9 µm, and the average height above the surface was 15,0 µm, resulting in an average height of 153,9 µm. However, considering that the standard deviation was 67,8 µm due to some melt pools forming keyhole melt pools and others only conduction melt pools, using the average height as a measurement for assessing the accuracy of the simulation becomes questionable.

For this parameter set, considering the overall shape of the melt pool could provide a more accurate comparison with the simulation results. Consequently, the width of the keyhole portion of the melt pool was measured for seven of the fifteen instances where keyhole melt pools formed. The average width of the keyhole was calculated to be 80,0 µm, with a standard deviation of only 4,3 µm. This resulted in an RSD of only 5.36%, showing that the width of the keyhole remains relatively consistent.

From the results for single tracks without powder, presented and discussed in this section, it was found that the created melt pools were repeatable for all but the keyhole parameter sets, with only small deviations in the cross-sectional melt pool geometry. This was confirmed by the low values of RSD of 3.39%, 1.96% and 3.77% for the weak, optimal and balling parameter sets seen in Table IV.

4.1.2. Single tracks with powder

The melt pool geometries and dimensions were much more inconsistent for the single tracks with powder. Therefore, two or three micrographs are presented in this section for each parameter set to provide a better understanding of the difference in geometries that were obtained. The dimensions of the melt pools for the different parameter sets created on a substrate with powder are summarised in Table V.

.

Table V: Summary of the dimensions of melt pools for the different parameter sets created on a substrate with powder.

Parameter set	Weak penetration	Optimal	Balling	Keyhole
Average depth (µm)	33,5	93,1	73,3	206,1
Standard deviation (µm)	15,8	11,1	21,7	48,3
RSD (%)	47,0	11,9	29,6	23,5
Average width (µm)	60,2	130,1	104,3	194,4
Standard deviation (µm)	11,5	9,76	12,7	10,1
RSD (%)	19,1	7,50	12,1	5,20
Width/Depth Ratio	0,56	0,72	0,70	1,06

Weak penetration parameter set

Figure 28 shows melt pool geometries obtained with the weak penetration parameter set applied to a substrate with powder.

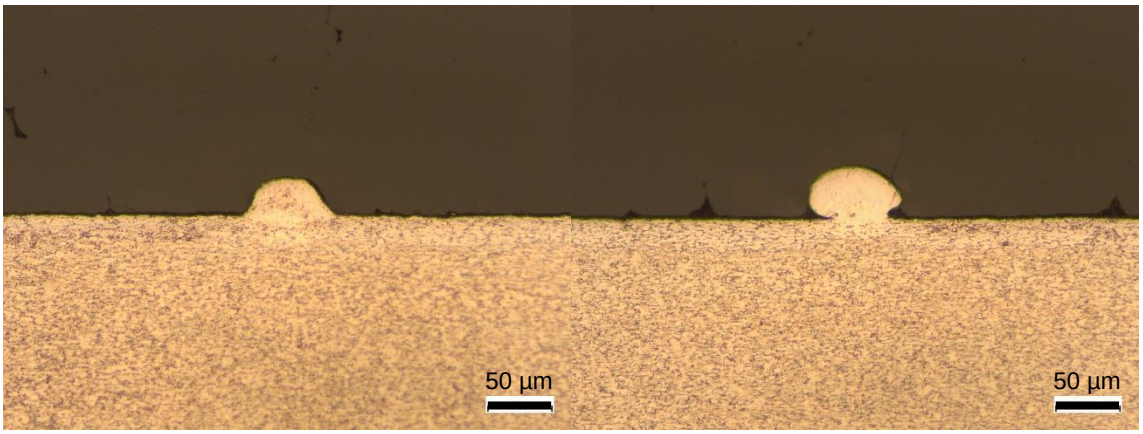

Figure 28: Cross-sectional optical micrographs of typical melt pool geometries obtained with the weak penetration parameter set applied to a substrate with powder

The weak penetration into the substrate is clear in Figure 28. For this parameter set, the average depth of penetration into the substrate was 7,8 µm, and the average height of the melt pool above the substrate was 25,5 µm. This resulted in an overall melt pool height of 33,5 µm with a standard deviation of 15,8 µm, as shown in Table V. This equates to an RSD of 47%. This deviation is substantial and shows the inconsistency caused by the powder bed. The average width at the surface was 60 µm compared with 74 µm for the single tracks without powder. Here, a standard deviation of 11.5 µm was observed. This

equated to an RSD of 19%. Although this is much better than the RSD for the depth, it is clear that a substantial deviation occurred in the width of the single track. For two of the single tracks, no penetration into the substrate occurred.

Optimal parameter set

Figure 29 shows typical melt pool geometries of single tracks obtained with the optimal parameter set applied to a substrate with powder. Compared to the previous parameter set, much greater consistency was evident for the cross-sections of single tracks generated with this parameter set.

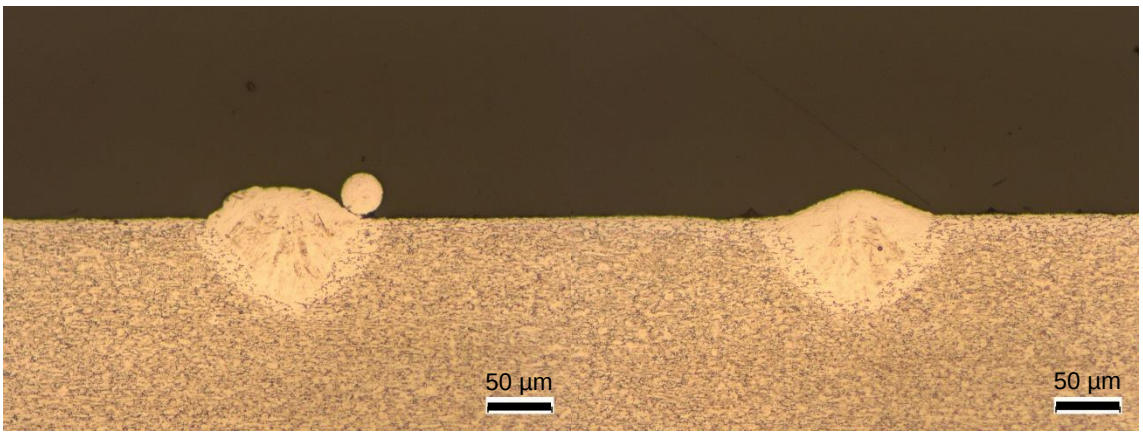

Figure 29: Cross-sectional optical micrographs of typical melt pool geometries obtained with the optimal parameter set applied to a substrate with powder

The average depth of penetration into the substrate for this parameter set was 66 µm below the surface, with an average height of 27 µm above the surface. This resulted in an average melt pool height of 93 µm with a standard deviation of 11 µm, which gave rise to by far the lowest RSD for the depth of the melt pool of 11.5% for all parameter sets for builds with powder. The average width of the melt pool was 130 µm, which was slightly larger than the width of 117 µm for optimal single tracks without powder. This resulted in a depth-to-width ratio of 0.72, compared to 0.64 for the single tracks without powder. For the width, a standard deviation of 9,76 µm was observed. This equates to an RSD of only 7.5% – also the lowest RSD for the widths of the melt pools with powder.

Balling parameter set

Figure 30 shows some interesting cross-sections obtained when investigating this parameter set for single tracks built on a substrate with powder. A few cross-sections still showed occurrences of the humping effect. Some cross-sections showed very little penetration into the substrate, and for others, wetting of the substrate did not even occur, and balling of the single track on top of the substrate could be seen. The results for this parameter set were the most inconsistent of the results with powder.

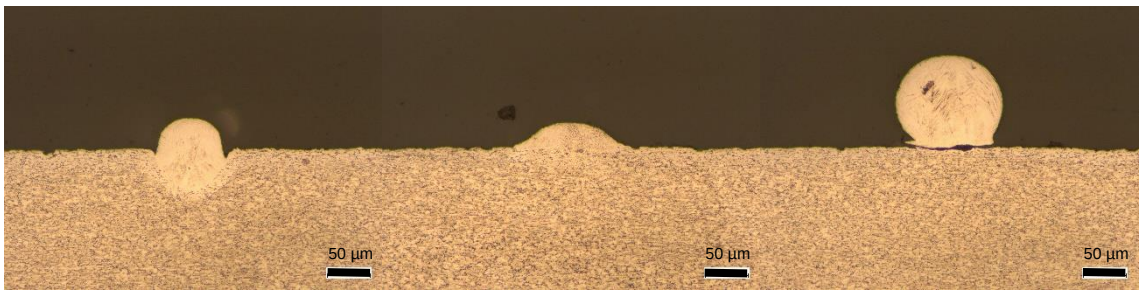

Figure 30: Cross-sectional optical micrographs of various melt pool geometries obtained with the balling parameter set on a substrate with powder

The depth of penetration ranged between 0 and 48 µm, with an average depth of 34.6 µm. Table V shows that the height above the substrate varied substantially, with values as low as 18 µm and as high as 106 µm obtained in some cases. The average for this value was 38.7 µm. Interestingly, the RSD for the total height of the melt pool was substantially lower than the RSD for the height above and depth below the surface. When considering the width of the created tracks, it was found that these were much more repeatable. The average width was 104 µm, which was almost identical to the results without powder. The RSD, however, was 12% compared to the 1.5% for the tracks without powder. From these results, it became clear that it would not be possible to assess the accuracy of the simulation results based on average values for all parameter sets but rather from a range of dimensions and geometries that were obtained. It must be noted, however, that the inconsistencies seen in Figure 30 limit the significance of the average values and standard deviations noted above. The complete dataset is presented in Appendix G.

Keyhole parameter set

Figure 31 shows the typical cross-sectional geometries of melt pools obtained with the keyhole parameter set on a substrate with powder. When comparing the results of single tracks obtained with the keyhole parameter set on a substrate with powder to the results

of the keyhole single tracks without powder, there was again substantial variability in the cross-sectional geometry of the melt pools. It was noted that the widths and standard deviation for the width were very similar. However, the RSD of the depths of the melt pools were much smaller for the single tracks created with powder, decreasing from 44% to 23.5%, indicating more stable keyhole formation for these single tracks. This could be due to the enhanced absorption of laser energy by the layer of powder.

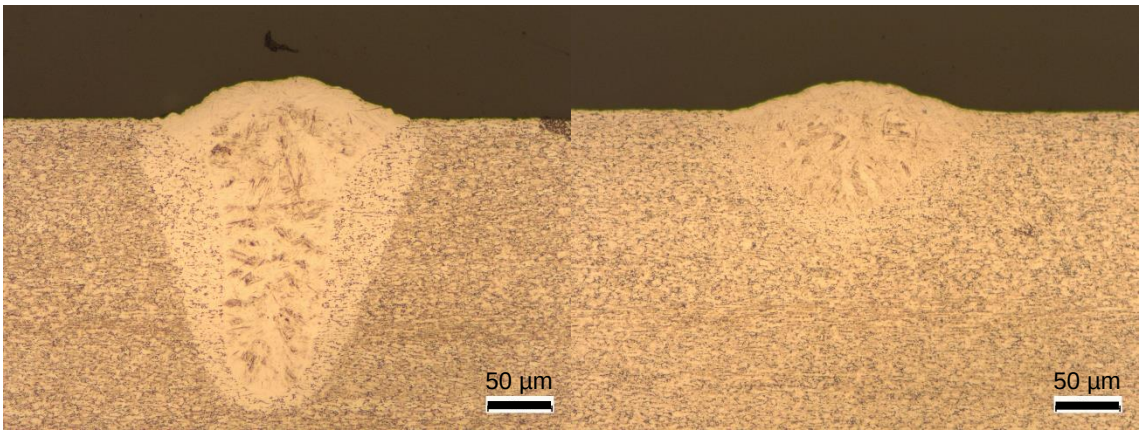

Figure 31: Cross-sectional optical micrographs of typical melt pool geometries obtained with the keyhole parameter set on a substrate with powder

Penetration below the surface ranged between 81 and 222 µm, with an average value of 176 µm. Height above the surface was fairly consistent, with an average value of 29.8 µm. Width at the surface was similar to the results obtained without powder in both dimension and deviation, with an average of 194 µm and an RSD of 5.2%. Of all the results of single tracks created with powder, the width of this parameter set was least affected by a powder layer.

4.1.3. Single layers with and without powder

As mentioned in the methodology, only the optimal process parameter set was considered in the creation of single layers. Single layers were created both with and without powder. The results of the creation of these single layers are presented and discussed in this subsection.

Single layer without powder

A few observations can be made when considering the cross-sectional micrograph of a single layer without powder, as shown in Figure 32.

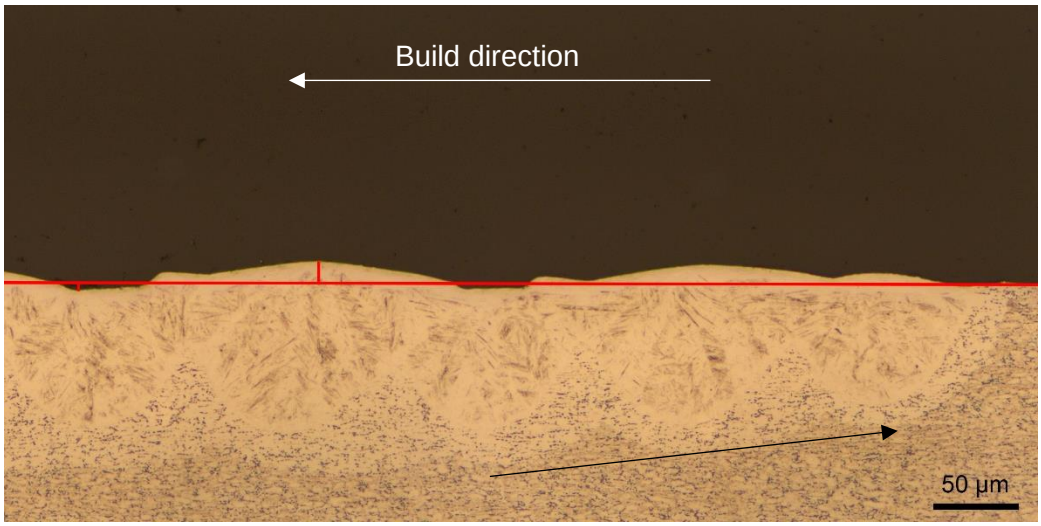

Figure 32: Cross-sectional optical micrograph of a single layer created without powder. A hatch spacing of 80 µm was used. The black arrow at the bottom of the image shows the skewed heat-affected zones.

Firstly, this process parameter set created a relatively flat surface, with measurements of the height of the top surface of the melt pool ranging from 12.9 µm above the unmelted surface to 4.5 µm below the unmelted surface. The local minimum and maximum values are indicated by the vertical red lines in the figure.

Secondly, it can be seen in Figure 32 that the melt pool shape of the individual tracks alternates between smaller and larger melt pools. Smaller melt pools have an estimated width of 117 µm and a depth of 77.9 µm. These values are similar to the single tracks investigated in section 4.1.1. These values show small increases when measured from the right to the left of the figure.

However, the larger melt pools have an average depth of 97 µm. This is much larger than the melt pool sizes observed when investigating single tracks without powder. It is believed that this is due to the elevated temperature of the substrate upon the creation of these tracks, as the laser rapidly created a new track right next to the just-created track.

Lastly, it is clear that the heat-affected zones (HAZ) are skewed to the right in Figure 32. This is attributed to the increased thermal conductivity of Ti6Al4V at elevated temperatures, as discussed in section 2.5.5. This is also an indication of the scanning

direction, as it can be inferred from this that the single tracks were created from the right of this figure to the left.

Single layer with powder

A cross-sectional micrograph of a single layer created with powder is presented in Figure 33.

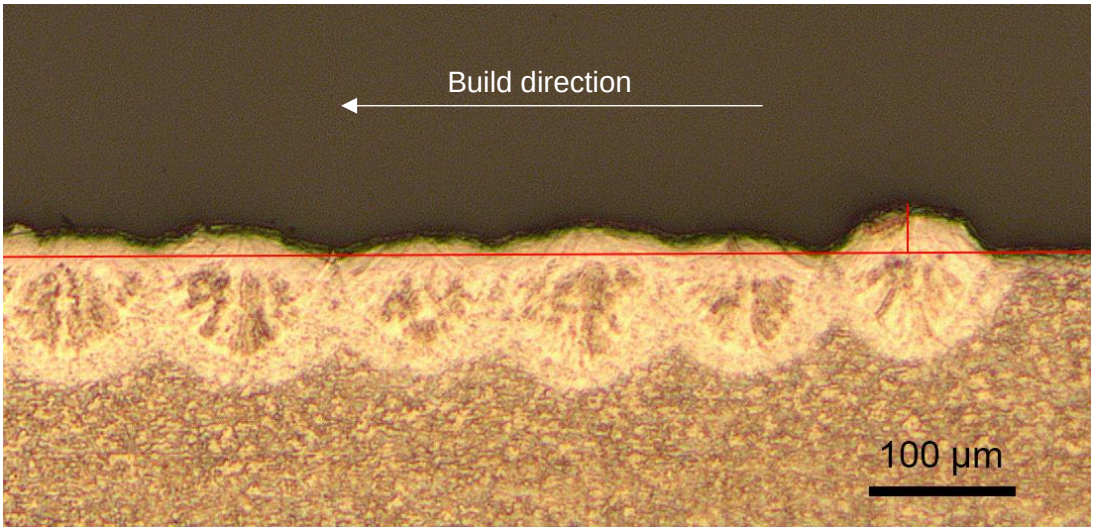

Figure 33: Cross-sectional optical micrograph of a single layer created with powder. A hatch spacing of 80 µm was used.

Here, the optimal process parameter set again created a relatively flat surface, except for the first single track on the far right of the figure. Measurements of the height of the top surface of the melt pool ranged from 29.6 µm above the unmelted surface for this single track to level with the unmelted surface. The maximum local value is indicated by the vertical red line in the figure.

It can again be seen that the melt pool shape of the individual tracks alternates between deeper and shallower melt pools. However, here the overall depth of the first single track is deeper than the track that was created second. The first melt pool has an estimated width of 114.5 µm and a depth of 105.5 µm. These values are somewhat peculiar, as they are both narrower and deeper than the single tracks discussed in section 4.1.2.

The melt pools have an average depth of 91 µm. This, interestingly, compares well with the average depth of the single tracks. However, the average widths of the melt pools were 118 µm, which is lower than the average track width for the single tracks with powder.

The HAZ are also again skewed to the right in Figure 33. This effect is, however, much less pronounced than for the single tracks without powder.

4.2. Simulation results

At the advent of the simulations, the simulation input parameters of the properties of the metal vapour were unknown. Initially, these factors did not seem of great importance, as various studies did not consider the effects of evaporation on the process at the time (Huang et al., 2016) (Knapp et al., 2017) (Mukherjee et al., 2018) (Rauniyar & Chou, 2019).

However, subsequent simulations indicated that both evaporative cooling and evaporation pressure play a very important role in the formation of melt pools, even for the optimal process parameter set (see sections 4.2.3 and 4.2.6). Because the values for these parameters were unknown, they were changed during experimentation and did not remain constant for all simulation sets. Consequently, in the following sections, these values are mentioned for each specific simulation set that was run, and the rationale for these changes is discussed.

4.2.1. Mesh studies

Mesh studies were conducted to determine the optimal cell size for future simulations. Seven different cell sizes were selected for simulation to investigate the effect of the mesh cell size on the convergence of the results. These were 20 µm, 15 µm, 12.5 µm, 10 µm, 7.5 µm and 5 µm. These can be compared to the experimental optimal melt pool width that varied between 115 µm and 120 µm. These cell sizes were chosen based on the limited experience with previous simulations at the time. The optimal parameter set was used in the mesh study.

The mesh dependency investigation was based on temperature profiles and the cross-sectional geometries of single tracks. During simulations, a point just below the melt pool was selected to monitor the temperature for each simulation.

Figure 34 compares the predicted temperature profiles of numerical solutions using meshes with different cell sizes.

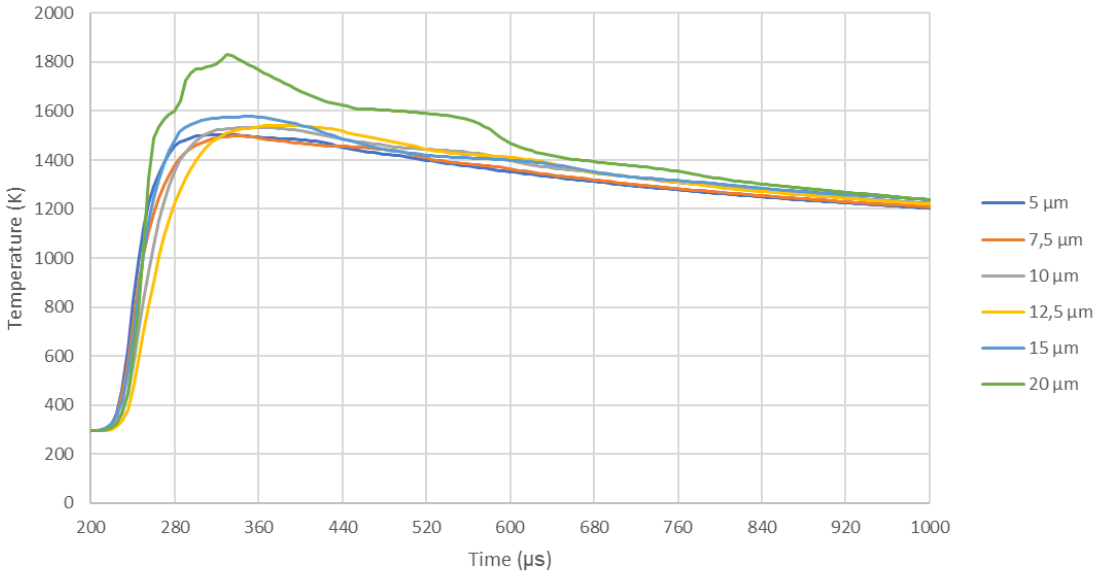

Figure 34: Effect of cell size on the convergence of simulation results for the optimal parameter set for a point along the track, just below the molten region.

From Figure 34, it is clear that the smaller cell sizes converged faster to a single solution. A cell size of 20 µm yielded relatively higher temperature values over most of the time frame compared to those obtained with smaller cell sizes. The results converged quicker using cell sizes of 15 µm or 12.5 µm. Maximum temperatures still varied by approximately five to ten per cent for these cell sizes, and the temperature gradient for these cell sizes was also distinctly different. The curves for the 10 µm, 7.5 µm and 5 µm cell sizes were very similar.

It was noted that a cell size of 5 µm increased the simulation time substantially when compared to a cell size of 7,5 µm and that the use of a mesh with smaller cell sizes in and close to the melt pool and larger cell sizes further away from the melt pool could potentially reduce simulation time. Consequently, this procedure was followed in all subsequent simulations, as discussed in more detail in section 3.5.

These results also highlighted the interesting nature of these simulations, where a high degree of accuracy – and therefore small cell sizes – was required within the region of the mesh where the melt pool formed. This was due to the complex melt pool dynamics. Much larger cells could be used in areas of the mesh where it was only required to account for thermal diffusion.

Figure 35 shows the evolution of the predicted melt pool geometry of numerical solutions using meshes with different cell sizes. In these views, the upper lines of the melt pools represent the surfaces of the melt pools, and the bottom lines the fusion lines. These cross-sectional views were taken in the yz-plane at x = 360 µm. Superimposing all melt pool geometries onto a single picture led to a very cluttered view, and therefore, a few comparisons were made and are discussed here.

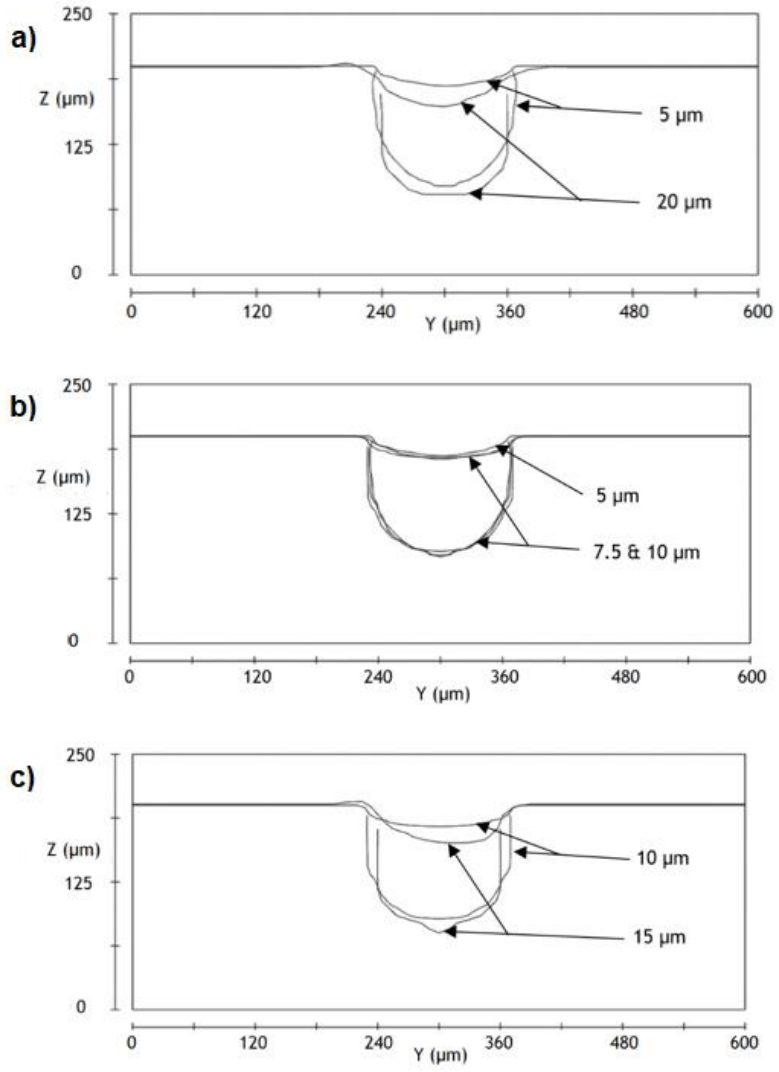

Figure 35: Difference between the simulated melt pool geometries for a) 5 µm and 20 µm cell sizes, b) 5 µm, 7.5 µm and 10 µm cell sizes, and c) 10 µm and 15 µm cell sizes for the optimal parameter set (without powder)

Figure 35 a) clearly illustrates a very large difference in melt pool geometry between the 20 µm and 5 µm cell size simulations. This was to be expected because the mesh density in the two cases differed substantially. When comparing the 10 µm, 7.5 µm, and 5 µm cell

size melt pool geometries in Figure 35 b), it is clear that the solution was converging. The differences between these geometries are very small, and a conclusion that a cell size of 7.5 µm would be optimal for a trade-off between accuracy and solver time held merit. Lastly, noticeable differences were apparent when comparing the 10 µm geometry with the 15 µm geometry in Figure 35 c).

These results showed that a cell size of 7,5 µm could be accepted as an optimal trade-off between solver time and accuracy. It was decided to repeat this process for the keyhole parameter set to ensure that this was indeed the optimal cell size. The results from these simulations are shown in Figure 36.

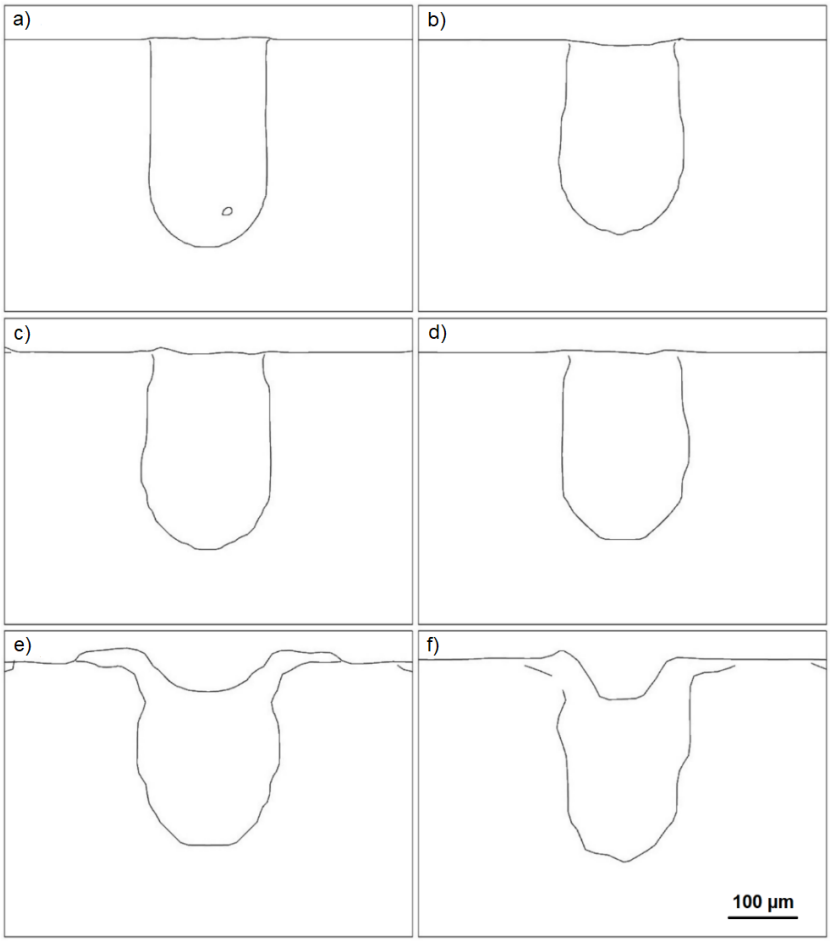

Figure 36: Difference between the simulated melt pool geometries for a) 5 µm, b) 7,5 µm, c) 10 µm, d) 12,5 µm, e) 15 µm and f) 20 µm cell sizes for the keyhole parameter set

Based on the difference in geometry between Figure 36 a) and Figure 36 b), specifically the vertical sidewalls and the inclusion of porosity in Figure 36 a), it became clear that substantial modelling errors could still be encountered with a cell size of 7,5 µm. It was,

therefore, decided to use a cell size of 5 µm for all future simulations. This agreed well with the values used in the literature. Cheng et al. (2019) also used a cell size of 5 µm. It must be noted, however, that adopting smaller cell sizes made computation prohibitively expensive without significantly adding to the accuracy of results.

4.2.2. Initial single tracks without powder

The initial simulations of single tracks without powder were run with an accommodation coefficient of 0.2 and an evaporation pressure coefficient of 10 000. These initial values were selected based on recommendations by the software provider and from setup demonstrations of the software.

Figure 37 shows the simulations of the cross-sections for different parameter sets. Blue indicates the metal substrate, and red indicates the molten region. The coloured region between the blue and red regions indicates the region of partial melting.

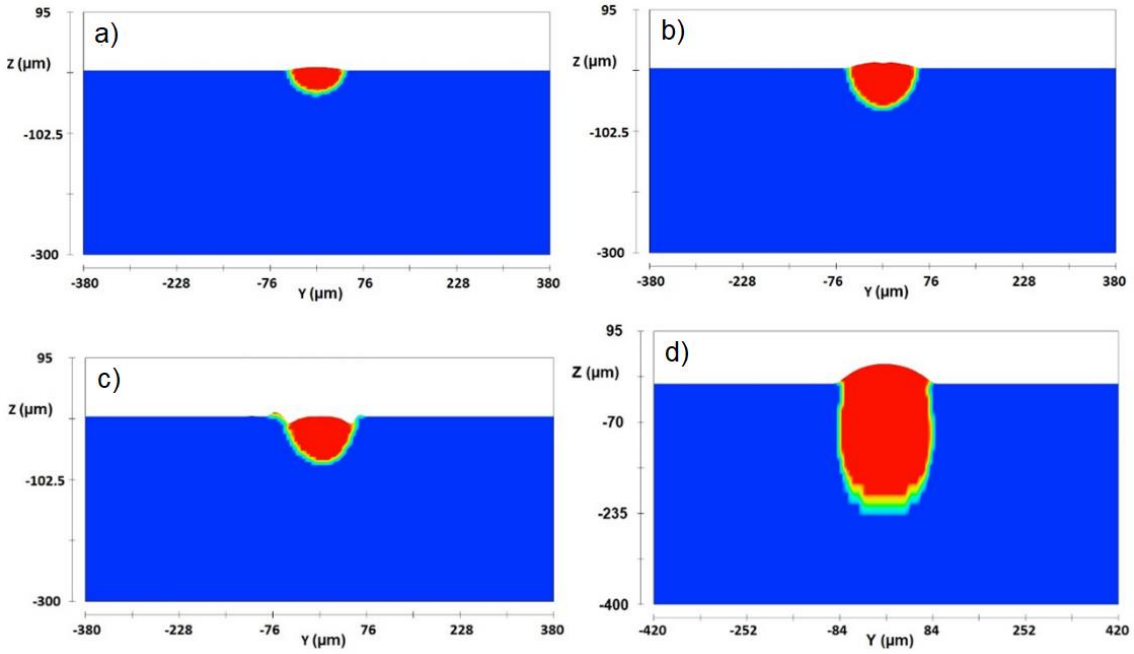

Figure 37: Cross-section results of the simulations of a) weak penetration process parameter set, b) optimal process parameter set, c) balling process parameter set and d) keyhole melting process parameter set

After the simulations were completed, the cross-sectional width and depth of the melt pools were analysed using the software and compared with the experimental results obtained. The variation of the dimensions of the simulated melt pools from the experimentally determined dimensions is shown in Table VI.

Table VI: Simulated melt pool dimensions of melt pools compared to experimental dimensions for the different process parameter sets.

Parameter set	Weak Penetration	Optimal	Balling	Keyhole
Simulated depth (µm)	40	75	76	259
Experimental depth (µm) (± Standard deviation)	21 (± 1)	71 (± 1)	52 (± 2)	139 (± 69)
Variation from experimental (%)	92	6	46	87
Simulated width (µm)	80	100	126	179
Experimental width (µm) (± Standard deviation)	74 (± 2)	117 (± 2)	106 (± 2)	195 (± 9)
Variation from experimental (%)	8	-15	19	-8

Weak penetration parameter set: melt pool dimensions

When comparing the experimental melt pool shape with the simulation result, it was clear that the melt pool depth of the simulation differed by 92% from the experimentally obtained depth (Table IV). The respective widths of the melt pool compared well, with only a 7.8% difference between the simulation and experimental results.

It was initially thought that the difference in depth could be due to enhanced conductivity resulting from a too-coarse mesh. Subsequent simulations, however, indicated that although a reduced cell size of 3 µm did result in a reduction of the melt pool depth, it was still more than 60% deeper than the experimental average values. This latter simulation, however, resulted in a melt pool width of 76 µm, which differed from the average experimental results by less than four per cent. These results indicated that a too-high absorptivity value was possibly used.

Optimal parameter set: melt pool dimensions

From the results in Table VI, the melt pool dimensions for the optimal process parameters were closest to the experimentally obtained values of all the parameter sets, with the simulated melt pool being 5.8% deeper and 14.7% narrower than the experimental melt pools. Critical analysis of the difference in melt pool geometries highlighted that although the melt pool shapes correlated well, there were differences in the angle of the sidewall of the melt pool, as well as a melt pool that protruded higher above the surface for the

simulation. Consequently, the previous inference made for the case of the weak parameter set that a too-high absorptivity value was used in simulations might have been invalid.

Balling parameter set: melt pool dimensions

When comparing the simulated melt pool dimensions of the balling parameter set given in Table VI, the simulated dimensions were approximately 20% larger than the experimental values. The peculiar melt pool shape (protruding upper central part) obtained using the balling parameter set is shown in Figure 37 c). This result, however, was not found across the full length of the track in the model. Apart from this geometric change, the dimensions of the melt pool remained stable along the length of the simulated track.

Keyhole parameter set: melt pool dimensions

From the results presented in Table VI, it is clear that the simulated melt pool dimensions obtained with the keyhole parameter set showed variations from the experimentally determined dimensions that were fairly similar to the results obtained with the weak penetration parameter set. The simulated width of the melt pool surface only varied by eight per cent from the values obtained experimentally. This was an encouraging result. When comparing the depth of the melt pool, the result obtained from the simulation differed from the experimental mean by 70.4%. However, this value still falls well within two standard deviations of the experimentally obtained results. This is due to the large variation in the melt pool depth due to the instability of the keyhole melting process (refer to Figure 27 and Table IV). Although deep penetration into the substrate occurred, which is a characteristic of keyhole mode melting, the simulated melt pool geometry was not representative of the experimental results at all.

Given these results, the possible causes for the inaccuracies were investigated and are discussed in the following sections.

4.2.3. Investigation of the effects of the accommodation and evaporation pressure coefficients of Ti6Al4V

From the results presented and discussed in the previous section, it became evident that both the simulation width and depth and, specifically, the shape of the keyhole melt pool did not correlate well with experimental results. Therefore, the simulation input parameters that could be responsible for these inaccuracies were assessed. Because the values for

the accommodation coefficient and evaporation pressure coefficient were unknown, these values were initially investigated.

A sensitivity analysis of these parameters was done by running multiple simulations with various combinations of accommodation coefficients (0.05, 0.1, 0.2, 0.3, 0.4) and evaporation pressure coefficients (5 000, 10 000, 20 000, 30 000, 40 000, 50 000) for the keyhole parameter set. The effect of these coefficients on the shape and dimensions of the resulting melt pool was examined from the analysis.

Thirty simulations were run, from which the width and depth of the melt pool for each of the simulations were recorded. Three-dimensional plots based on these results were created using the Matplotlib package in Python to investigate any trends in melt pool dimensions resulting from the variations of the accommodation coefficient and the evaporation pressure coefficient. The effect of these parameters for the keyhole parameter set on the width of the melt pool is shown in Figure 38, and their effect on the depth of the melt pool is shown in Figure 39. The data on the geometry of all simulations carried out is included in Appendix H.

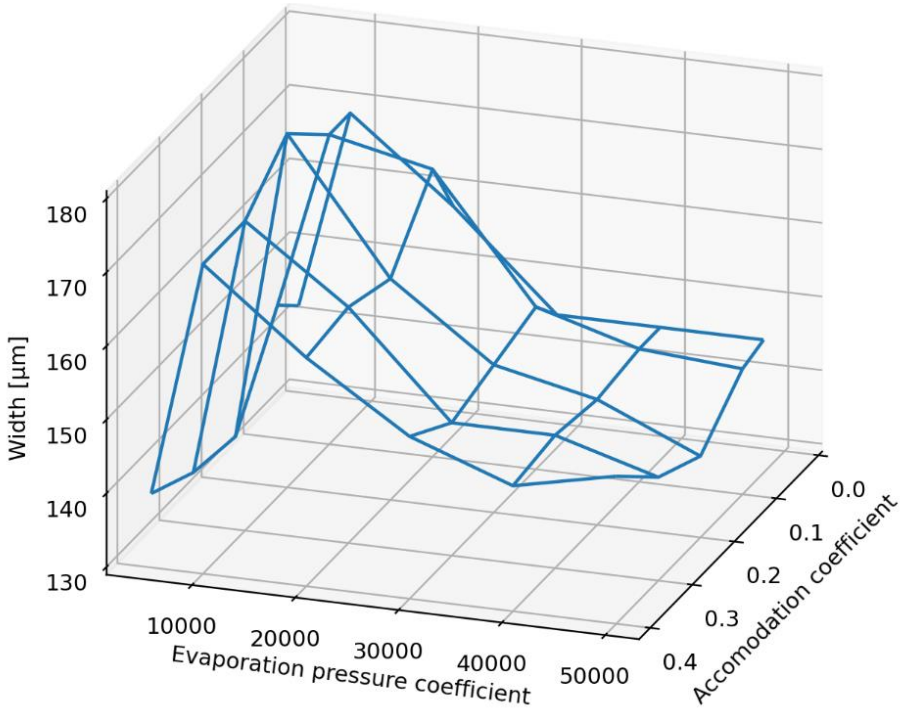

Figure 38: Effect of the accommodation and evaporation pressure coefficients on the width of the melt pool for the keyhole parameter set

From Figure 38, it is clear that although both the accommodation coefficient and evaporation pressure coefficient affected the width of the melt pool, the evaporation pressure coefficient had a much greater effect. It was also noted that this effect of the evaporation pressure coefficient was not linear but rather had a local maximum at an evaporation pressure coefficient of approximately 10 000. This trend may be explained by the change in the melt pool wall angle at the liquid-argon interface (the depressed region in the melt pool), causing reflections of the laser beam to widen the melt pool as the melt is in a transition between conduction and keyhole mode melting.

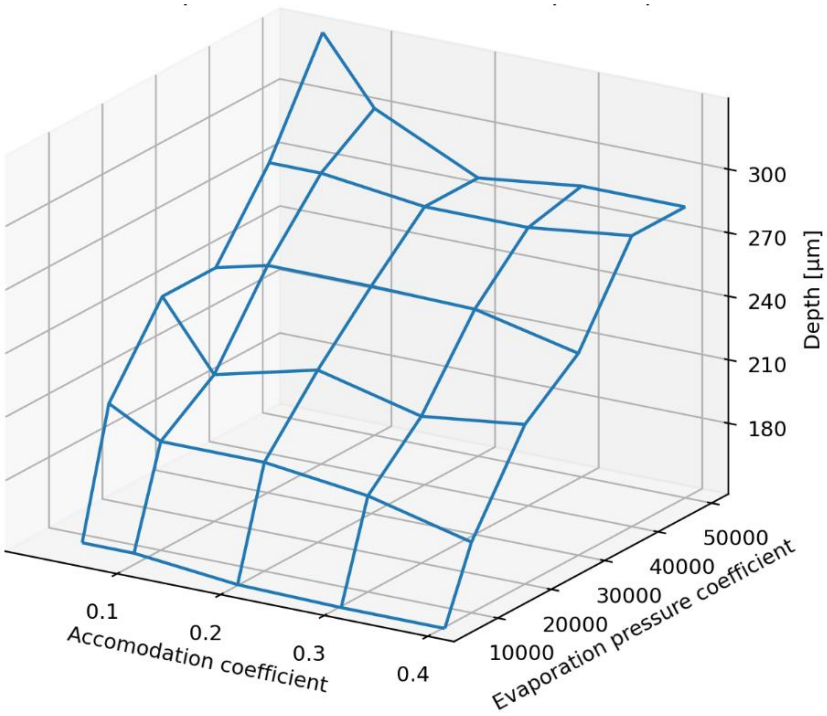

Figure 39: Effect of the accommodation and evaporation pressure coefficients on the depth of the melt pool for the keyhole parameter set

The plot in Figure 39 demonstrates that the evaporation pressure coefficient has a much greater effect on the melt pool depth than the accommodation coefficient. However, the effect of the evaporation pressure coefficient on the depth of the melt pool was much less non-linear than its effect on the melt pool width. This was expected since the pressure from evaporation directly affected the penetration depth into the substrate. It was also noted that, despite exceptions, there was a trend for the melt pool depth to increase when a lower accommodation coefficient was used, and the evaporation pressure coefficient was kept constant.

Finally, when considering the geometries of the melt pools that were created during this study (see also Appendix H), it was concluded that, although these coefficients greatly affected both the melt pool height and width, no combination of coefficients that were used in simulations resulted in a melt pool of which the shape was similar to that obtained from the experimental investigation.

However, this investigation still confirmed that these parameters directly affected melt pool dimensions and that it was important to gain an increased understanding of how they should be used in simulation and how these coefficients affected melt pool geometries.

4.2.4. Theoretical investigation of accommodation and evaporation pressure coefficients

As a consequence of the study reported in section 4.2.3, the origin of the accommodation and evaporation pressure coefficients, as well as the way they were used in the simulation software, was investigated.

The information in the following subsections, which was obtained from the user manual included with the software, is discussed. In the description in the user manual of the model used for calculating the evaporation pressure, it was mentioned that no generic equation existed for determining evaporation pressure and that the model discussed below was used.

The equation used to determine the evaporation pressure is a rework of the original Clapeyron equation, which relates the saturation pressure to the current temperature. Then, a reasonable approximation of the evaporation pressure can be found by assuming that the evaporation pressure is equal to the saturation pressure at a higher temperature. The Clapeyron equation reads as follows:

$$\frac{\partial P}{\partial T} = \frac{\Delta H^{vap}}{T \Delta V} \tag{4.1}$$

Here, P refers to pressure, T temperature, ΔH^{vap} the latent heat of vaporisation, and ΔV the change in volume. By rewriting the Clapeyron equation, substituting the volume of the vapour with the relationship $V = \frac{(\gamma-1)C_v^{vap}T}{P}$ and assuming the volume of liquid to be negligible when compared to the volume of vapour, the Clausius-Clapeyron equation is

derived. This equation is found in various forms, but to aid the discussion here, it is given in the form:

$$P_{sat} = P_v e^{\frac{-\left(\frac{1}{T}-\frac{1}{T_v}\right)\Delta H^{vap}}{(\gamma-1)C_v^{vap}}} \tag{4.2}$$

Where (P_v, T_v) is a point on the saturation curve in the phase diagram (for the present case, the known saturation pressure (atmospheric pressure) and temperature (boiling point) of Ti6Al4V), P_{sat} is the saturation pressure at the elevated temperature used in a calculation. In this instance, it is the approximated vapour pressure. C_v^{vap} is the specific heat at constant volume and γ the ratio of the specific heat. This is represented graphically in Figure 40.

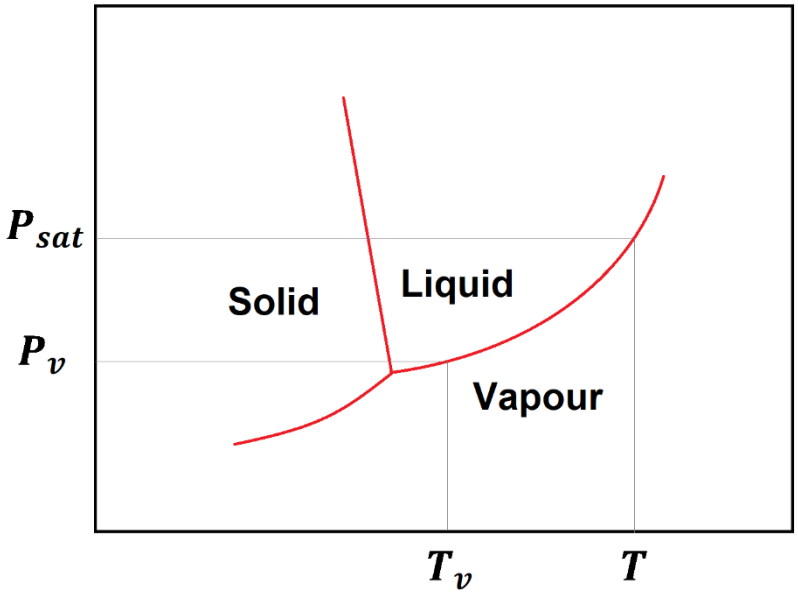

Figure 40: Calculation of the saturation pressure (evaporation pressure) at a given temperature using the Clausius-Clapeyron equation

By using equation 4.2 and combining all constants in the exponent (specific heat, specific heat ratio, saturation temperature at atmospheric pressure and latent heat of vaporisation) and equating this to a B evaporation pressure coefficient, the following equation can be obtained to determine the evaporation pressure:

$$P_{evap} = Ae^{B\left(1-\frac{T_v}{T}\right)} \tag{4.3}$$

Here, P_{evap} is the evaporation pressure, and A the first evaporation pressure coefficient (the evaporation pressure coefficient that was varied in simulations), which is equal to the saturation pressure corresponding to T_v, in this case, the atmospheric pressure multiplied by the fraction of material that evaporates. The latter fraction is unknown and, in practice, relates to the accommodation coefficient of the material. In the simulation, however, this parameter can be changed independently or calculated as the product of the accommodation coefficient and atmospheric pressure.

The symbol B stands for the second evaporation pressure coefficient, which is a combination of material constants in the exponent. The symbol can be written as follows:

$$B = \frac{\Delta H}{(\gamma - 1) C_v^{vap} T_v} \tag{4.4}$$

It should be noted that the larger the difference between the evaporation pressure and the saturation pressure, the more inaccurate this approximation becomes. Therefore, the symbol B can be calculated accurately with the above equation for evaporation taking place close to the saturated vapour point that is used. However, this approximation becomes more inaccurate when moving away from this point on the phase diagram.

Because this second evaporation pressure coefficient can be calculated using known material properties, only the first evaporation pressure coefficient (A) was further investigated while accepting the theoretically determined value of the second evaporation pressure coefficient (B).

From a better understanding of the evaporation pressure coefficients used in the simulation software, it became clear why the coefficients A and B were required in the software and also why these coefficients could potentially not remain constant for all process parameter sets. Considering the simulation results of section 4.2.3, which clearly indicated that these coefficients definitively affected the simulation predictions, it was concluded that more information on the behaviour of metal vapour in the melt pool was needed before the values for these coefficients in simulations could be accurately determined.

Accommodation coefficient

From an investigation of the equations that contain the accommodation coefficient, it was found that this value was used as a coefficient in calculating the rate of evaporation of a material. The following equation is used for this end.

$$\dot{m} = \alpha \sqrt{\frac{M}{2\pi RT}} (P_l^{sat} - P_v) \tag{4.5}$$

Where the symbol α is the accommodation coefficient, M the molecular mass of the vapour, R the gas constant, T the average liquid temperature along the surface of the melt pool, P_l^{sat} the saturation pressure for the known boiling point and P_v the calculated saturation pressure of the vapour.

From this equation, it follows that the heat loss due to evaporation is also directly affected by the accommodation coefficient used since the evaporative cooling is determined by considering the rate of evaporation of a material. This is clear from the following equation

$$q_{evap} = \frac{\alpha \times \Delta H}{\sqrt{2\pi MRT}} (P_l^{sat} - P_v) \tag{4.6}$$

Considering this, it became evident that the accommodation coefficient was coupled with the evaporation pressure in more than one way. The accommodation coefficient directly affects the rate of evaporation, which determines the evaporative cooling. This, in turn, affects the calculated evaporation pressure because the surface temperature is used to calculate the evaporation pressure (see equation 4.3).

Evaporation pressure and accommodation coefficients used in literature

An improved understanding of the use of the evaporation pressure and accommodation coefficients, as well as the forms of equations in which they were found, made it possible to identify the values used for these parameters in other published studies. These values were often given in equation form without discussing the rationale behind their use. A summary of some of the studies that did mention the values used, as well as the specific values, is given in Table VII.

Table VII: Evaporation pressure and accommodation coefficients used in published studies.

Study	Evaporation pressure coefficient (A) [kPa]	Accommodation coefficient
Cheng et al. (2019)	54 000	0.82
Bayat et al. (2019)	54 000	0.01
Chen et al. (2021)	54 000–56 000	N.A.
Wu et al. (2018)	54 000	N.A.
Khairallah et al. (2020)	54 000	N.A.
Khairallah et al. (2016)	54 000	0.82

Many other studies did not discuss the values used at all, and a substantial number of studies indicated that the effects of evaporation were not included in simulation work. Some of the abovementioned work also did not provide references for the values used. However, the source for the values of 0.54 and 0.82 for the evaporation pressure coefficient and accommodation coefficient, respectively, was a book by von Allmen & Blatter (1995) on the interactions of laser beams with materials. This publication provided valuable insight into the coefficients and the reason for their use, which will be discussed shortly.

In the fifth chapter of this book, Von Allmen & Blatter (1995) discussed the thermodynamics and kinetics of metal evaporation, as well as the use of the Clausius-Clapeyron equations for determining the evaporation pressure of vaporised metal. For the rate of evaporation, a “sticking” or accommodation coefficient was introduced, defined as the fraction of vapour particles that collide with the surface adhering to it. However, the authors noted that this value was usually close to unity for metals.

Von Allmen & Blatter (1995) discussed evaporation at moderate laser irradiance levels where the metal vapour was cool enough to be considered transparent. Under this assumption, the expansions of vapour and recoil pressure were discussed.

A region known as the Knudsen layer exists where collisions occur among the vapour particles for a few micrometres above the evaporation surface. Making a few assumptions, including an accommodation coefficient of unity, it was calculated that the vapour temperature just outside the Knudsen layer was only 65% of the surface temperature, resulting in a much cooler and less dense vapour outside of the Knudsen layer.

Considering this, it was calculated that approximately 18% of the evaporating material returned to the surface, resulting in an evaporation rate of 0.82 times the initially calculated evaporation rate.

This was the accommodation coefficient value that was used in some studies. Therefore, this value was not purely an accommodation coefficient but rather an accommodation coefficient of unity, multiplied by a correction factor of 0.82 to account for the effect of the Knudsen layer on the evaporation rate.

Von Allmen & Blatter (1995) then used this value in conjunction with the lowered vapour temperature above the Knudsen layer to calculate an effective evaporation pressure of 0.54 of the saturation pressure calculated with the surface temperature using the Clausius-Clapeyron equations. This inferred that the first evaporation pressure coefficient (A) should have been 0.54 multiplied by the saturation pressure corresponding to the saturation temperature used in the equations, in our case, the atmospheric pressure of approximately 100 kPa.

Finally, somewhat unrelated to this topic but of importance to the current study, Von Allmen & Blatter (1995) also stated that the heat lost through evaporation was much more significant than that lost through radiation. This indicated the importance of accurately calculating the evaporation rate and pressure in SLM simulations.

Given the findings in sections 4.2.3 and 4.2.4, all simulations were rerun with the updated values of the accommodation coefficient and evaporation pressure coefficient to investigate whether more accurate results could be obtained using the updated values.

4.2.5. Reworked single tracks without powder

After rerunning the simulations for all parameter sets with the updated accommodation coefficient of 0.82 and evaporation pressure coefficient of 0.54, the results shown in Table VIII were obtained.

Table VIII: Comparison of simulated melt pool (without powder) dimensions based on an evaporation pressure coefficient of 0.54 and an accommodation coefficient of 0.82 with the experimentally obtained dimensions.

Parameter set	**Weak penetration**	**Optimal**	**Balling**	**Keyhole**
Simulated depth (µm)	35	76	95	400
Experimental depth (µm) (± Standard deviation)	21 (± 1)	71 (± 1)	52 (± 2)	139 (± 67)
Variation from experimental (%)	68	6	83	188
Simulated width (µm)	80	94	130	140
Experimental width (µm) (± Standard deviation)	74 (± 2)	117 (± 2)	106 (± 2)	195 (± 9)
Variation from experimental (%)	8	-20	22	-28

The simulation results indicated a too-large melt pool cross-section for most parameter sets compared to the experimental results, likely indicating that a too-high absorptivity value was used. Consequently, the absorptivity values used in the simulation were adjusted to correlate the simulated results better with experimental results.

A study by Cunningham et al. (2019) used high-speed X-ray imaging to visually investigate the formation of melt pool depression due to evaporation and found that evaporation pressure had a pronounced effect on the formation of the melt pool, even for process parameters that were considered optimal. However, the laser power used with the weak penetration parameter set was sufficiently low to prevent evaporation and consequent vapour depression of the melt pool. This proved to be very useful since once it could be ascertained that evaporation pressure did not affect the penetration depth for a particular parameter set, that parameter set could be used to modify the absorptivity value until the penetration depth of the experiments and simulations correlated well.

This approach optimised the absorptivity value used for simulation until a good correlation between the experimental and simulated penetration depths for the weak penetration parameter set was obtained. The updated values of temperature-dependent absorptivity that gave good correlation are presented graphically in Figure 41. The absorptivity increased from 0.15 at room temperature to 0.3 at the liquidus temperature and remained at 0.27 for all temperatures above the melting point.

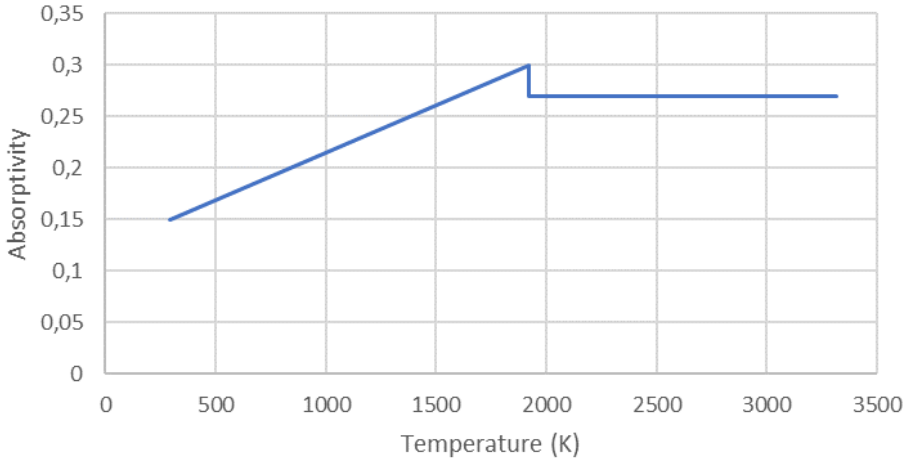

Figure 41: Graphical representation of the updated values of temperature-dependent absorptivity

By using the absorptivity values given in Figure 41, the resulting melt pool dimensions displayed in Table IX were obtained.

Table IX: Comparison of the cross-sectional dimensions of the melt pools obtained from simulations using updated absorptivity values with the experimental results.

Parameter Set	**Weak penetration**	**Optimal**	**Balling**	**Keyhole**
Simulated depth (µm)	23	56	72	321
Experimental depth (µm) (± Standard deviation)	21 (± 1)	71 (± 1)	52 (± 2)	139 (± 69)
Variation from experimental (%)	12	-21	38	131
Simulated width (µm)	72	89	117	138
Experimental width (µm) (± Standard deviation)	74 (± 2)	117 (± 2)	106 (± 2)	195 (± 9)
Variation from experimental (%)	-3	-24	10	-29

Although the absorptivity curve shown in Figure 41 yielded results very close to the experimental results for the weak penetration parameter set, the melt pool created with the optimal parameter set was 21.4% shallower and 24.1% narrower than the experimental results. In contrast, the melt pool created with the balling parameter set was 38.3% deeper and 10.2% wider than the experimental results. Lastly, the keyhole dimensions were 138.9% deeper than the experimental, while the width was still 29.4% smaller than the experimental results.

4.2.6. Comparison of simulation results with results by Cunningham et al.

Because the simulations with the updated evaporation pressure coefficient, accommodation coefficient and absorptivity values still varied substantially from the experimental results for the balling and keyhole parameter sets, it was decided to compare the formation of the melt pool over time with the experimental results presented by Cunningham et al. (2019). The intention here was to see whether the cause of the variation from experimental results arising from the simulations at these process parameters could not be obtained through visual inspection and comparison of the simulation with experimental work.

In the study by Cunningham et al. (2019), a 156 W laser with a spot size of 140 µm was focused onto the substrate and left stationary on a point for approximately 2 ms to investigate the formation of keyhole mode melting in the SLM process. Because the same material as in the current study (Ti6Al4V) was used for their study, a new simulation was set up here using the parameters used by Cunningham et al. (2019) to allow comparison with their results.

Figure 42 compares the experimental melt pool dimensions for the different timesteps of a laser drilling process described in the study by Cunningham et al. in column a) on the left and simulation results from this study in column b). The simulation figures next to the experimental figures correspond to the timestamps indicated by Cunningham et al. (2019).

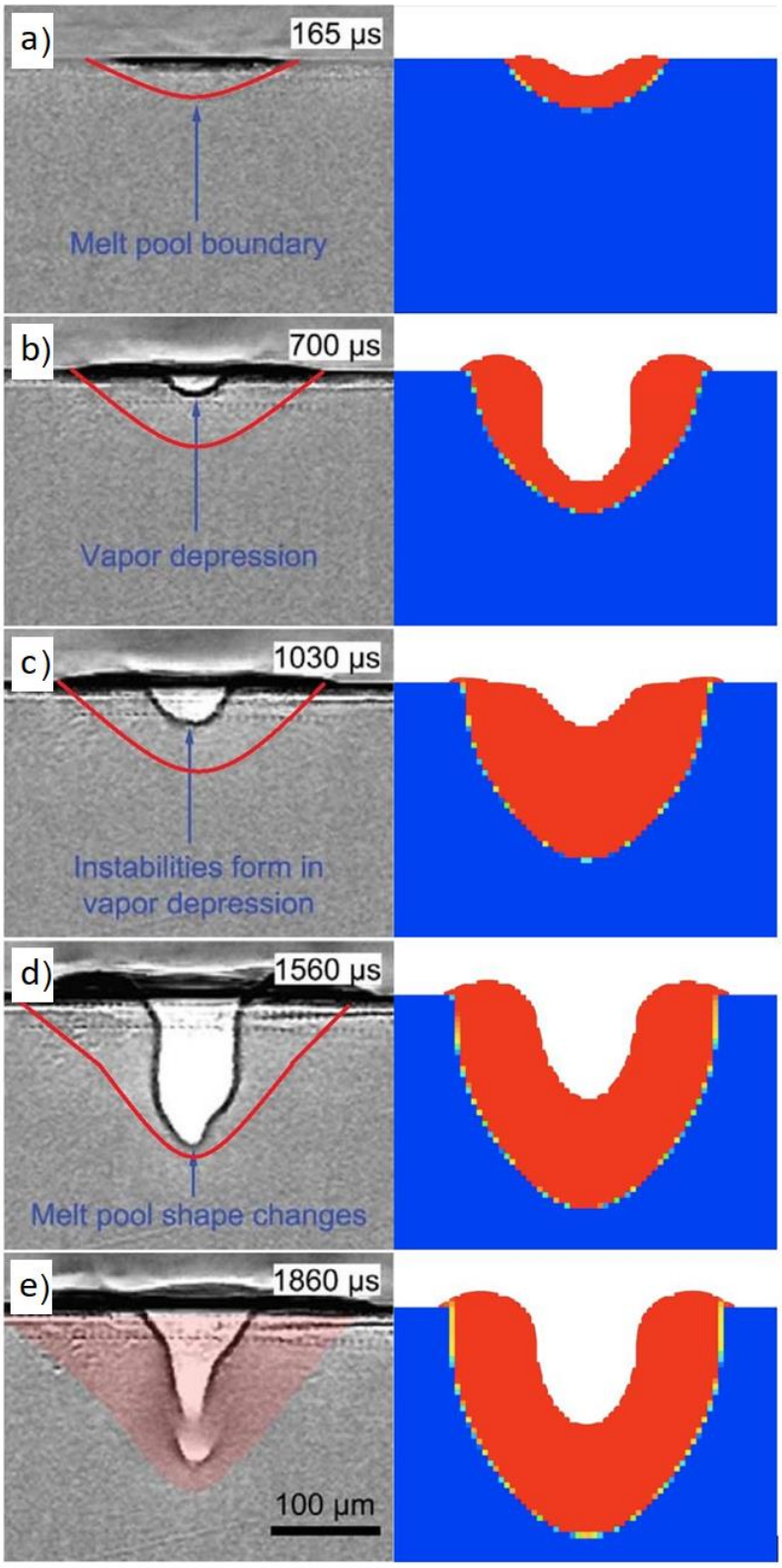

Figure 42: Comparison of column a) in-situ x-ray images by (Cunningham et al., 2019) and column b) simulated cross-sections for the laser drilling process. Molten regions and boundaries are indicated in red.

From Figure 42, the following observations were made. Firstly, it was clear that the simulated melt pool width initially widened rapidly (see Figure 42 b)) to a value smaller than the experimentally obtained values and then continued to widen at a much slower rate. This is in contrast to the experimental melt pool that widened throughout.

Secondly, the simulated melt pool deepened at a much faster rate than the experimental melt pool. The simulated melt pool that was narrower than the experimental, indicated that a higher absorptivity value is required to create a wider melt pool. At the same time, the simulated melt pool was deeper than the experimental and larger in overall size. This indicated that a lower absorptivity value is required than that which was used. This discrepancy implied that a higher absorptivity was required at the onset of the formation of the melt pool and a lower absorptivity value as the laser drilling progressed.

It should be noted that not much information can be gathered from the shape of the vapour depression in Figure 42. These micrographs were taken in situ, and the vapour depression shape differed substantially with time due to the oscillatory movement of the vapour depression within the melt pool. This can be seen in the video material published by Cunningham et al. (2019).

Lastly, a distinct difference between the simulated and experimental melt pool shapes was apparent from a comparison of the geometry of the experimental and simulated melt pool. For the experimental results, the melt pool started shallow on the sides and got progressively deeper in an almost linear contour. However, the simulated melt pool had almost vertical walls on the sides, more representative of a semi-circle.

These results clearly indicated that not only were the simulation melt pool dimensions not accurate, but neither was the simulation melt pool geometry. Various simulations indicated that, although the simulation melt pool geometry was affected to a lesser extent by the evaporation pressure, it still did not change the almost vertical sidewall of the melt pool.

Consequently, the effects of changing the surface tension temperature-dependent coefficient and viscosity on the shape of the melt pool were investigated. This is followed by indications in the literature that the viscosity and surface tension temperature-dependent coefficient could vary widely based on the concentration of various impurities, such as oxygen, in the base metal. Figure 43 shows the effect of different temperature-dependent surface tension coefficients on the shape of the melt pool.

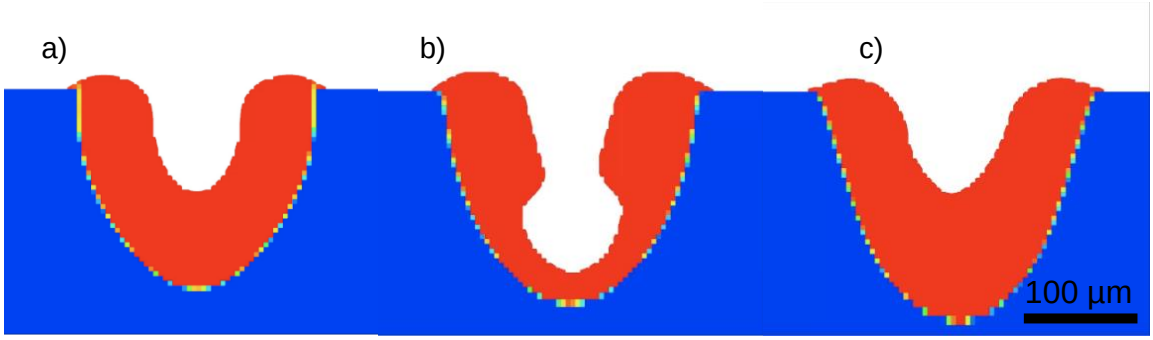

Figure 43: Effect of varying the surface tension temperature-dependent coefficient on the shape of the melt pool. The temperature-dependent coefficients used were a) -0.0004 N/m/K, b) -0.00019 N/m/k and c) 0 N/m/K

From these simulations, it became clear that larger, or even positive, coefficients resulted in a more linear, less vertical melt pool sidewall, which better resembled the results obtained experimentally. However, on changing the viscosity, no notable difference in melt pool geometry was observed. In contrast, on implementation of a higher temperature-dependent surface tension coefficient in the original simulations, no noticeable difference in melt pool geometry apart from the less-vertical sidewalls was found.

4.2.7. Final single tracks without powder

From the results presented in Table IX, it was deemed possible that the deviating simulated melt pool dimensions could have been due to a lower absorptivity at the melting point and a higher absorptivity at the boiling point. This possibility was investigated by using the following temperature-dependent absorptivity profile: an absorptivity of 0.14 at room temperature that increases to 0.3 at the beta transus temperature, then remains constant at 0.27 to the liquidus temperature and then increases to 0.4 at the boiling point. The results obtained from the simulation, based on these values, are presented in Table X.

Table X: Melt pool dimensions resulting from further updated absorptivity values.

Parameter set	Weak penetration	Optimal	Balling	Keyhole
Simulated depth (µm)	28	71	108	400
Experimental depth (µm) (± Standard deviation)	21 (± 1)	71 (± 1)	52 (± 2)	139 (± 69)
Variation from experimental (%)	35	0	108	188
Simulated width (µm)	72	91	130	137
Experimental width (µm) (± Standard deviation)	74 (± 2)	117 (± 2)	106 (± 2)	195 (± 9)
Variation from experimental (%)	-3	-22	22	-30

From the results in Table X, it is clear that values relatively close to the experimental values were obtained for both the weak penetration and optimal process parameter sets. However, using this temperature-dependent absorptivity curve, the results of the melt pool depth for the balling and keyhole parameters deviated greatly from the experimental results.

4.2.8. Comparison of all results for single tracks without powder

In an attempt to ensure that all trends were considered, all results from the four previous simulation sets were compared with each other. Table XI compares the experimentally obtained depths of the melt pools for the various parameter sets with the simulated results presented previously. This is also graphically represented in Figure 44. The table numbers in the table and figure refer to the datasets found in the respective tables in section 4.2.

Table XI: Comparison of simulated melt pool depth to the experimental values for the various simulations that were conducted without powder.

Parameter set	Weak Penetration	Optimal	Balling	Keyhole
Experimental depth (µm)	21	71	52	139
Table VI – Depth variation (%)	92	6	46	87
Table VIII – Depth variation (%)	68	6	83	188
Table IX – Depth variation (%)	12	-21	38	131
Table X – Depth variation (%)	35	0	108	188

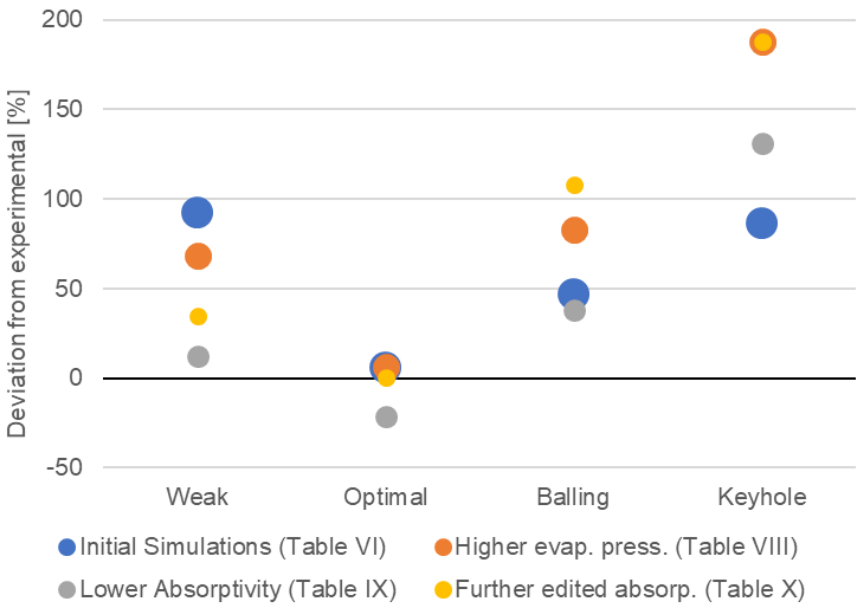

Figure 44: Comparison of the deviation of the simulated melt pool depth from the experimental average depth for all different input parameter sets used for single tracks without powder

From Figure 44, it became clear that after the updated evaporation pressure coefficient was implemented according to the literature (Table VIII), the simulation results deviated further from the experimental values for higher applied laser power than the initial simulations (Table VI). With the implementation of the lower, temperature-dependent absorptivity (Table IX), the simulation results were closer to the experimental results for all but the optimal parameter set. Therefore, it was concluded that the updated absorptivity improved the results, while the updated evaporation pressure resulted in poorer results.

A further observation was that the depth of the simulated melt pool created using the optimal parameter set was consistently lower than the simulated depth of the other parameter sets compared to the experimental results. This remained so, irrespective of the changes that were made to the model. This led to multiple investigations using the model. However, the cause of this discrepancy remained unclear.

Table XII compares the experimentally obtained widths of the melt pools for the various parameter sets with the simulated results presented previously. This is also graphically represented in Figure 45. The table numbers here again refer to the datasets found in the respective tables in section 4.2.

Table XII: Comparison of simulated melt pool width to the experimental values for the various simulations that were conducted without powder.

Parameter set	Weak Penetration	Optimal	Balling	Keyhole
Experimental width (µm)	74	117	106	195
Table VI – Width variation (%)	8	-15	19	-8
Table VIII – Width variation (%)	8	-20	22	-28
Table IX – Width variation (%)	-3	-24	10	-29
Table X – Width variation(%)	-3	-22	22	-30

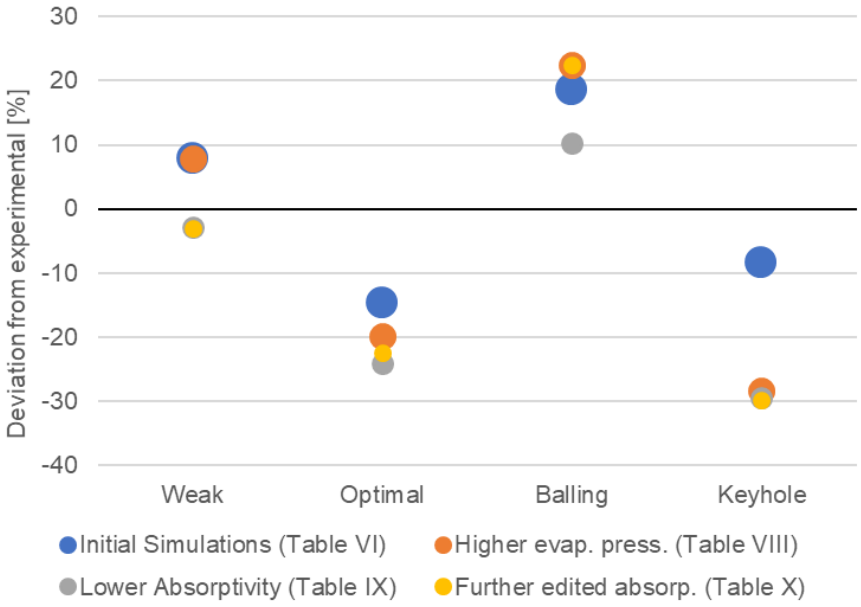

Figure 45: Comparison of the deviation of the simulated melt pool width from the experimental average depth for all different input parameter sets used for single tracks without powder

The most notable feature of Figure 45 is the lack of discernible trends. When evaporation pressure and material absorptivity were changed substantially, the deviation of simulated melt pool width remained relatively small, except for the keyhole melt pool width. For the keyhole parameter set, the increase in evaporation pressure led to a significant decrease in the simulated melt pool width. However, this same change in evaporation pressure led to an increase in the simulated melt pool width for the balling parameter set. The increase in evaporation pressure led to an increase in the difference between the experimental and simulation results.

Finally, except for the effect of the change in absorptivity on the simulation results for weak penetration and balling parameter sets (Table IX), all other changes to the model only resulted in increased deviation of the simulation results from the experimental results.

4.2.9. Simulated single tracks with powder

The same absorptivity and evaporation pressure coefficients were used for the simulations reported in this section, as discussed in section 4.2.5. This was done as additional changes to the model after this point did not result in increased accuracy of the model.

Weak penetration parameter set

For the weak penetration parameter set, a cross-section of the simulation results is presented below in Figure 46. For this image, the smoothing of surface contours was not enabled in the user interface, and the individual cells in the numerical model are clearly visible. In this figure, red cells are fully molten, blue cells are unmelted, and the coloured cells are partially melted, as for the other simulation results.

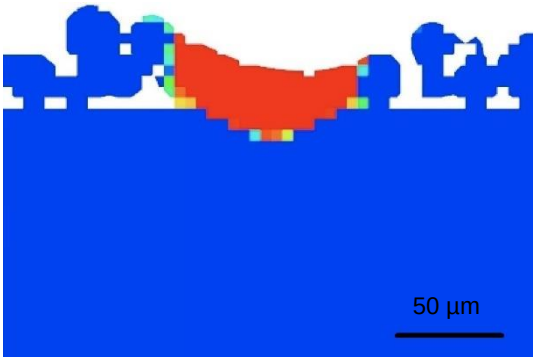

Figure 46: Cross-section of the simulation results for the weak penetration parameter set with powder

Considering the width of the simulated melt pool, a simulated width of 87 µm was observed. This is in sharp contrast to the experimental width of 60 µm but correlates well with the simulation results of a single track without powder in section 4.2.5. The depth of the melt pool was 50 µm, compared to the experimental depth of 33 µm. These inaccuracies are believed to be due to the same reasons discussed in section 4.2.5.

However, observing these simulation results, a few additional observations were also made. Firstly, when looking at the top surface of the melt pool, a concave rather than convex shape, as seen in the experimental results, was observed. Apart from the reasons discussed earlier, this difference in shape was also due to the unmolten particles of

powder staying in place and not being able to move. This is, unfortunately, a disadvantage of the FVM and cannot be changed unless this model is coupled with a simultaneous DEM simulation.

It is also evident that a very coarse cell size was used during meshing when comparing the cell sizes to the powder particle sizes. However, making the cell sizes smaller than the current 5 µm resulted in vastly increased simulation times, with simulations running for several days.

Optimal parameter set

A cross-section of the simulation results for the optimal process parameter set with powder is provided in Figure 47.

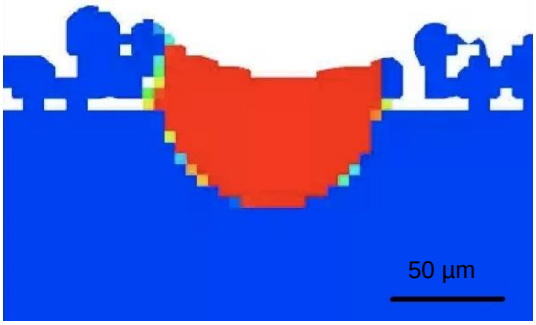

Figure 47: Cross-section of the simulation results for the optimal parameter set with powder

When considering the optimal process parameter set simulation results, results very similar to those of the simulation without powder were observed. The width of the simulated melt pool was 106 µm, compared to the experimental width of 130 µm. The depth of the simulated melt pool was 76 µm, compared to the experimental depth of 76 µm. The same observations regarding the modelling of the layer of powder are also applicable when considering the simulation results for this parameter set.

Balling parameter set

A cross-section of the simulation results for the balling process parameter set with powder is provided in Figure 48.

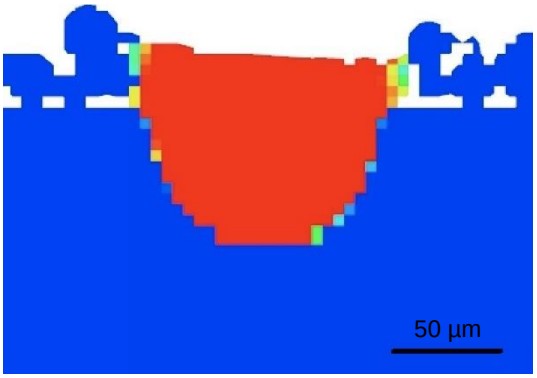

Figure 48: Cross-section of the simulation results for the balling parameter set with powder

The width of the simulated melt pool was 119 µm, compared to the experimental width of 104 µm. This is somewhat higher than the experimental results but again in line with the simulation results without powder. A simulated depth of 96 µm was observed, in contrast with the experimental depth of 73 µm. This is again in line with the simulation results without powder.

Keyhole parameter set

For the simulation of the keyhole parameter set, a few obstructions were encountered. Firstly, the addition of a layer of powder to the geometry of this simulation resulted in a drastically increased load on the solver and, therefore, a substantially increased solving time.

The next problem encountered was that the addition of the powder bed geometry to the simulation resulted in an increased spattering of small particles at high velocities. This adversely affected the simulation and resulted in the simulation failing after approximately 24 hours of running the solver. Multiple attempts were made to complete the simulation, but this could not be achieved. For this reason, no cross-section of the simulation results is included here. However, from the in-situ results of the simulation, it was found that the experimentally observed keyhole melt pool shape was still not formed.

4.2.10. Simulated single layer without powder

A cross-section of the results obtained for the simulation of a single layer without powder by applying the optimal process parameter set is represented in Figure 49.

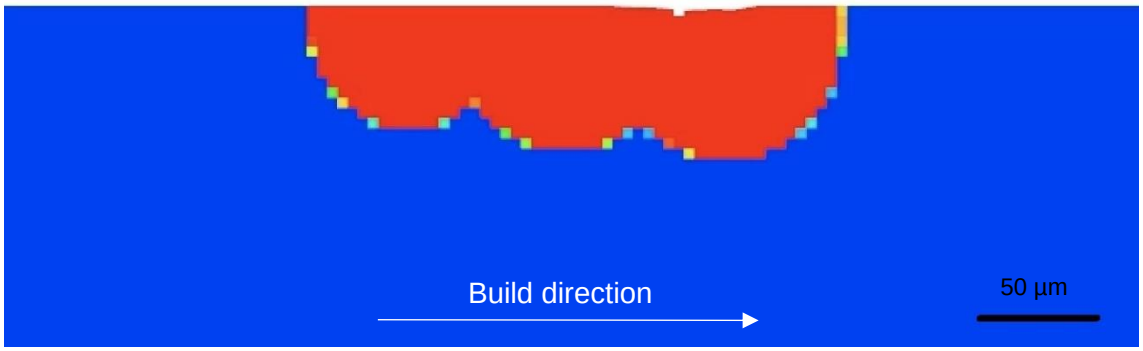

Figure 49: Cross-section of the simulation results for a single layer without powder using the optimal process parameter set

Because inaccuracies were already observed at the single-track level, it was decided that only a qualitative comparison between the simulated and experimental results would be made for the results of a single layer.

Considering the single layer in Figure 49 from left to right, the first single track created on the left had the same shape and dimensions as the single track observed in section 4.2.7, as expected. As subsequent single tracks were created, it was observed that the depth continued to increase due to the residual heat of the creation of the previous single tracks in the model.

The alternation of smaller and larger single tracks was not observed in these results. This was due to the difference in time between the creation of the single tracks, as well as the position of the sectioning of the substrate. These settings were corrected for the simulations of single layers that included powder and are discussed below.

When comparing individual single tracks to the experimental results, the observations made previously in this chapter are again valid here.

4.2.11. Simulated single layer with powder

A cross-section of the results obtained for the simulation of a single layer with powder by applying the optimal process parameter set is represented in Figure 50. The single track that was created first is on the left.

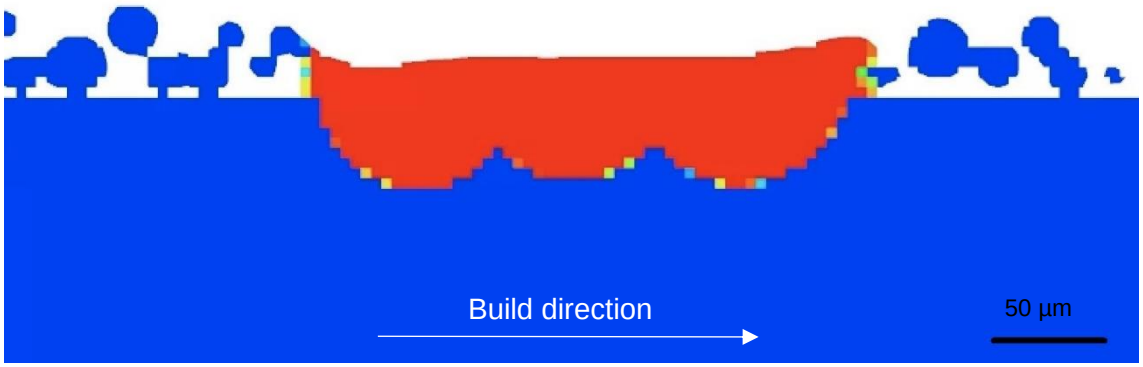

Figure 50: Cross-section of the simulation results for a single layer with powder using the optimal process parameter set

The observations made for single tracks with powder in section 4.2.9 are again valid for the simulation of a single layer. A few additional observations were also made.

Firstly, when comparing these results with the experimental single layer with powder discussed in section 4.1.3, it was observed that the stationary powder bed affects the simulation substantially. In the experimental results, the height of the first single track above the substrate was substantially more than the subsequent tracks. This is due to the entrainment of the surrounding powder particles into the first track in a process known as denudation (Chen & Yan, 2020). Figure 51 shows the stationary powder bed of the simulation, not showing any signs of denudation

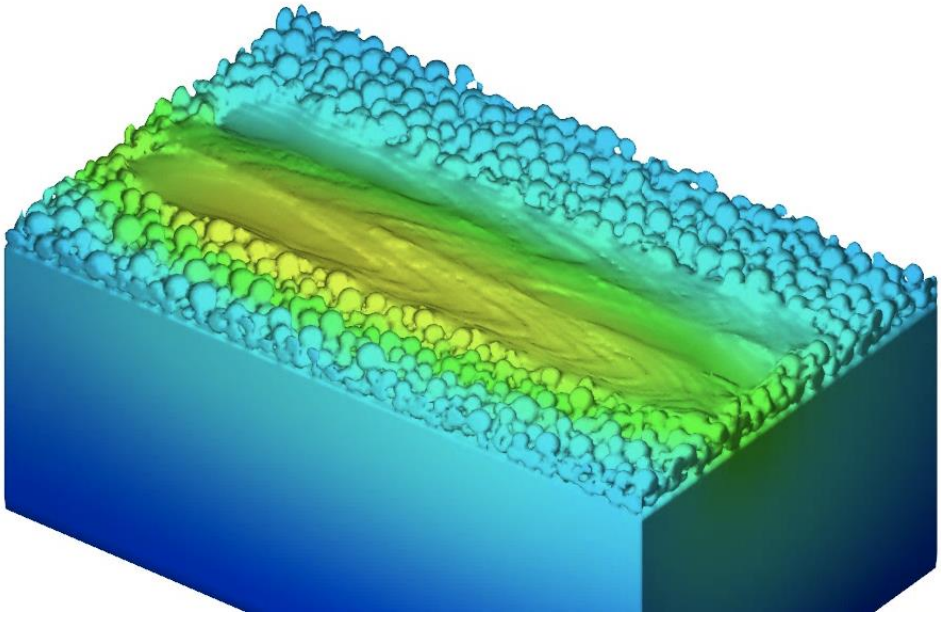

Figure 51: Isometric view of the simulation results with powder, showing the effect of the stationary powder bed on simulation results

Secondly, it was observed that the correction of the positioning of the cut through the substrate and the correction of elapsed time between the creation of the tracks resulted in the alternation between larger and smaller tracks, as was observed in the experimental samples.

In summary, it was observed that the same challenges encountered with the simulation of single tracks were again present with the simulations of single layers. However, no additional simulation errors were encountered during the simulation of single layers that could not be attributed to observations already made from the single-track results.

4.3. Discussion of inaccuracies of simulation results and their likely causes

After the results presented and discussed in this chapter were obtained, it was decided to investigate likely causes for the inaccuracies in the simulations since various authors had reported the dimensional accuracy of their models that far exceeded the accuracy obtained in some of the current simulations. From this investigation, and after consultation with one of the CFD engineers at FLOW-3D, the following was concluded.

At the time of this study, there were some shortcomings in the known values of material properties that were needed as inputs for these simulations. This resulted in tweaking of values used in each simulation run until the melt pool dimensions correlated well with experimental values. These results then, although dimensionally accurate, provided limited feedback on the accuracy of the simulation software.

Three values of material properties drastically affected melt pool dimensions but remained unknown at the time of the study. These material properties are discussed shortly in the following sections to highlight the difficulties in determining their values, as well as to show the effect of these values on the cross-sectional geometries of melt pools.

4.3.1. Absorptivity

In an insightful paper published by Lawrence Livermore National Laboratories (LLNL) (Ye et al., 2019), the authors found that the effective optical absorptivity of a material is greatly influenced by the process parameters used in the SLM process. This was concluded after conducting in-situ, precise calorimetry measurements. The effect of surface roughness on absorptivity was also noted. Figure 52 a) shows the effect of applied laser power on the

absorptivity of a bare substrate, as well as layers of powder of varying thicknesses. Figure 52 b) shows the effect of varying the scanning speed when scanning the substrate with no powder. It should be noted that this variation in absorptivity is complex and non-linear.

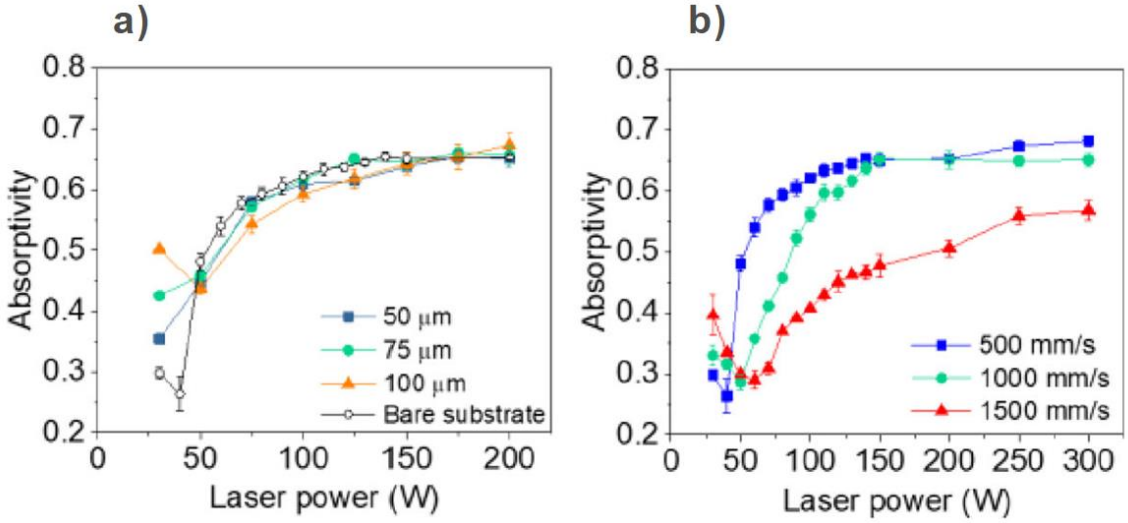

Figure 52: Effect of applied laser power on the absorptivity of Ti6Al4V for a) the bare substrate as well as powder layers of varying thicknesses and b) different scanning speeds (Ye et al., 2019)

A critical part of accurately modelling melt pool geometry is the accurate application of energy to the substrate. The results, showing that the absorptivity of the substrate can range between 0.26 and 0.66 depending on the process parameters used, highlight the difficulty in accurately applying energy to the substrate and layers of powder.

This is the first serious problem encountered when attempting to use a single simulation setup for various process parameters. After considering surface roughness and multiple reflections, it might appear that the remainder of the variation is due to the absorptivity of the material being temperature-dependent. However, temperature-dependent values of absorptivity are not readily available. From the current study, it is expected that accurate values of the temperature-dependent absorptivity of the material being investigated will greatly improve results when attempting to obtain melt pool dimensions through modelling.

However, another consideration is the detail of the effect of evaporation on the absorptivity measured in studies like that of Ye et al. (2019). Large amounts of energy carried away during the evaporation of the metal when using high laser powers and scanning speeds could result in an operative absorptivity that is lower than the measured value.

4.3.2. Evaporation pressure coefficients

The evaporation pressure directly above the melt pool affects the depth and the overall size of the melt pool. The observations made during the simulations show two main reasons for this.

Firstly, the depth of the melt pool is affected by the evaporation pressure because the pressure pushes molten metal out of the way, allowing the laser to penetrate deeper into the substrate. This is the mechanism by which keyhole mode melting occurs, and therefore the effect of the evaporation pressure on the depth of the melt pool is more pronounced at higher energy densities.

Secondly, the overall size of the melt pool can be increased by the evaporation pressure above the melt pool when the depressed region of the melt pool increases the effective absorptivity of the material through multiple reflections. This effect is explained in Figure 53.

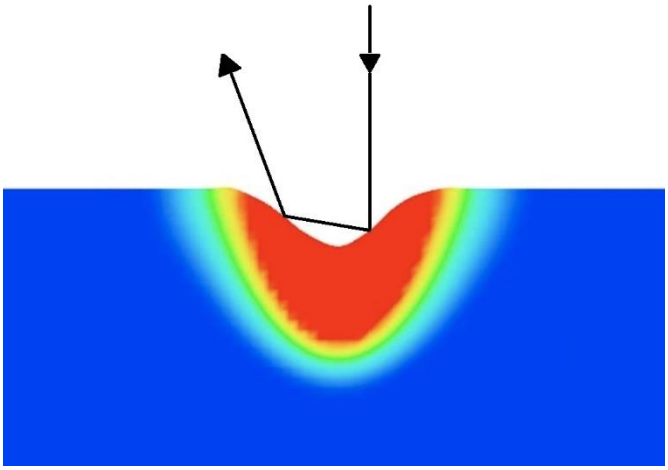

Figure 53: Diagram depicting the effect of evaporation pressure on the laser reflection and subsequent effective absorption

As observed in sections 4.2.3 and 4.2.4, a specific value for the evaporation pressure coefficient is not available, while this value greatly affects the size and shape of the melt pool. Also, based on the discussion of the origin of the evaporation pressure coefficient in section 4.2.4, it is not clear that the use of a single, non-temperature-dependent evaporation pressure coefficient is sufficient for the numerical modelling of melt pools over a broad range of process parameters.

For these reasons, it is proposed that the use of a single, fixed evaporation pressure coefficient for which the exact value is unknown partly explains the discrepancies between the numerical model and experimental results observed in this study.

4.3.3. Modelling of the powder bed

Considering the results obtained when modelling the powder bed, a few interesting observations were made regarding this part of the model.

An important factor is the effect of the mesh size on the reconstruction of the powder bed in the CFD simulation. Since the particle diameters ranged between 12 and 37 µm, as laid out in section 3.5.2, using a cell size of 5 µm resulted in a very coarse reconstruction of some of the smaller particles in the powder bed. This could be addressed by the use of smaller cell sizes but would result in vastly increased simulation times, as indicated earlier in this document.

The effects of this coarse mesh are exacerbated by the reconstruction of the powder bed using the VOF method. It results in the incorrect reconstruction of adjacent, touching particles, effectively bonding adjacent particles together. This incorrect reconstruction of the powder bed affects the modelling of multiple reflections, the wetting of the powder bed, and the effective thermal conductivity of the resulting powder bed.

In addition, using the FVM, the powder bed is modelled as a solid, and movement of the powder bed is not possible. This prevents the accurate modelling of important phenomena in SLM, specifically spattering and denudation, as was noted by Chen & Yan (2020).

4.3.4. Modelling of metal vapour

Results from this study have indicated that evaporative cooling and evaporation pressure proves to be much more integral to the shape and dimensions of the melt pool. This was indicated by a comparison of the work by Cunningham et al. (2020) with the work done in this study, where a clear discrepancy between the depressed vapour regions could be seen.

Building on the discussion in section 4.3.3, it is clearly essential to have accurate information on the movement and velocity of the gaseous phase to aid in the accurate modelling of phenomena such as denudation and spattering, even at the single-track level.

Chapter 5 - Conclusions

5.1. Achieving the aim of the study

The aim of this study was to determine whether, through numerical modelling and melt pool characterisation, process parameters for the selective laser melting of the Ti6Al4V alloy could be predicted.

Due to a few limitations, the aim of the study could not be fully achieved. Commercially available software capable of modelling the SLM process is extremely powerful. However, to accurately model SLM single tracks, some additions still need to be made to these software packages. Additionally, some challenges inherent to numerical modelling limited the accuracy of the results obtained with modelling as discussed in section 4.3. These are also summarised in section 5.3.

The addition of capabilities and information to the existing model would produce a substantial increase in the accuracy of the model and would most likely enable more accurate prediction of process parameters using simulated single tracks.

5.2. Achieving the research objectives

The first objective of this study was to create a numerical model of a single-track SLM process with existing commercial software, incorporating optimisation techniques found in the literature.

This objective was achieved in full using the commercial FLOW-3D software. Optimisation techniques such as temperature-dependent material properties, DEM modelling of the powder bed, variable mesh sizing and multiple Fresnel reflections were successfully incorporated into the model. Further extensive work was conducted to ensure accurate temperature-dependent material properties were used in this study.

The second objective was to validate the numerical model by comparing the melt pool characteristics with experimentally obtained results found in literature and through experimentation.

This objective of the study was reached in part. High-quality experimental results were successfully obtained from built tracks. Other in-situ experimental results were also obtained in the literature. Melt pool characteristics were compared between the experimental and simulation results, both in situ and ex situ. Various attempts to increase the accuracy of the model were also made based on the information obtained in the validation process.

The third objective was to assess the obtained preferred significant process parameters for the SLM process of Ti6Al4V and then use those parameters in the numerical model to determine the melt pool characteristics and compare these results for various sets of process parameters. This was expected to provide a range of process parameters with which parts of high quality could be created.

This objective could not be achieved in full. Because the accuracy of the numerical model was under investigation throughout the entire study, the numerical model could not yet be used to obtain process parameters with which parts of high quality could be created.

The last objective of this study was to expand the numerical model from a single-track model to a multiple-track, single-layer model.

This objective was also achieved in full. The numerical model was successfully expanded from a single-track model to a single-layer model. Simulation results for a single layer with and without powder were obtained and compared to experimental single-layer results.

5.3. Limitations and challenges of the numerical model

The following limitations and challenges were encountered during the creation of the model, as well as during the analysis of the obtained results.

The first limitation encountered was the limited availability of accurate, temperature-dependent material properties up to very high temperatures. This limited the accuracy of the model. This was particularly true for the availability of material properties of the gaseous phase and accurate temperature-dependent absorptivity values for bulk Ti6Al4V as discussed in section 4.3.1

The second challenge was the handling of the powder bed by the solver during the melting simulation. As there was no bi-directional coupling of FVM and VOF models, the accurate modelling of the movement of powder particles during the melting of the metal was not possible as discussed in section 4.2.11 and 4.3.3.

Thirdly, the computational time for running some single-track simulations were more than 24 hours as discussed in section 4.2.9. This computational cost for a single track simulation negates some of the advantages of using simulation instead of experimental work. This also limits the feasibility of adding complexity such as bi-directional coupling of FVEM and VOF models.

The fourth limitation that was encountered was the modelling of evaporated metal. As discussed in sections 4.3.2 and 4.3.4, the metal vapour, as well as its resulting pressure, has a marked impact on the results of the simulations. The omission or approximation of the resulting effect of the metal vapour, therefore, limits the accuracy of the model.

5.4. Conclusions

Numerical modelling of the SLM process is an incredibly powerful tool for understanding the underlying physical phenomena driving the peculiarities of the SLM process. Substantial information on the working of the process was obtained during this study by assessing the simulated process in situ – even with its limited capabilities.

The complete and accurate development of a digital twin for this process would be hugely beneficial, and continued research efforts focused on developing an accurate model of the SLM process, which should include all the phenomena discussed in this model, are essential.

5.5. Recommendations for future work

Considering the requirements of a model that would be accurate enough to predict process parameters for a material for which these parameters are completely unknown and the results obtained in this study, the following further research is required:

- Determine temperature-dependent material properties, specifically the absorptivity of the material in question up to its boiling point.
- Develop a numerical model that simultaneously considers the solid, liquid and gaseous phases of the metal.

- Develop a bi-directionally coupled DEM-FVM multiphase flow model to take momentum- and heat transfer between powder particles and the gaseous phase into account.
- Access high-performance computing capabilities, which can run such a coupled simulation in a reasonable time.

Other methods which reduce or eliminate the need for the prediction of SLM process parameters should also be considered as possible solutions to this problem. These include various optical- and acoustic in-situ monitoring systems with real-time feedback.

References

1. Andreotta, R., Ladani, L., & Brindley, W. (2017). Finite element simulation of laser additive melting and solidification of Inconel 718 with experimentally tested thermal properties. *Finite Elements in Analysis and Design 135*, 36-43.

2. Ansys. (n.d.). *Ansys Fluent Fluid Simulation Software*. Retrieved 09 22, 2021, from Ansys: https://www.ansys.com/products/fluids/ansys-fluent

3. Argyropoulos, C. D., & Markatos, N. C. (2015). Recent advances on the numerical modelling of turbulent flows. *Applied Matematical Modelling 39693-732*, 693-732. doi:10.1016/j.apm.2014.07.001

4. Attar, H., Calin, M., Zhang, L. C., Scudino, S., & Eckert, J. (2014). Manufacture by selective laser melting and mechanical behavior of commercially pure titanium. *Materials Science and Engineering A 593*, 170-177.

5. Aune, R., Battezzati, L., Brooks, R., Egry, I., Fecht, H., Garander, J., . . . Vinet, B. (2005). Surface Tension and Viscosity of Industrial Alloys form Parabolic Flight Experiments - Results of the ThermoLab Project. *Microgravity - Science and Technology, 16(1)*, 11-15.

6. Basak, D., Overfelt, R. A., & Wang, D. (2003). Measurements of Specific Heat Capacity and Electrical Resistivity of Industrial Alloys Using Pulse Heating Techniques. *International Journal of Thermophysics*, 1721-1733. doi:10.1023/B:IJOT.0000004101.88449.86

7. Bayat, M., Thanki, A., Mohanty, S., Witvrouw, A., Yang, S., Thorborg, J., . . . Hattel, J. H. (2019). Keyhole-induced porosities in Laser-based Powder Bed Fusion (L-PBF) of Ti6Al4V: High-fidelity modelling and experimental validation. *Additive Manufacturing 30*, 100835.

8. Beese, A. M., & Carroll, B. E. (2015). Review of Mechanical Properties of Ti-6Al-4V Made by Laser-Based Additive Manufacturing Using Powder Feedstock. *Journal of the Minerals, Metals & Materials Society*, 724-734.

9. Bergstrom, D. (2008). *The Absorption of Laser Light by Rough Metal Surfaces.* Doctoral Thesis: Lulea University of Technology.

10. Boivineau, M., Cagran, C., Doytler, D., Eyrand, V., Nadai, M. H., Wilthan, B., & Pottlacher, G. (2006). Thermophysical Properties of Solid and Liquid Ti-6Al-4V (TA6V) Alloy. *International Journal of Thermophysics, 27(2)*, 507-529.

11. Boley, C. D., Mitchell, S. C., Rubenchik, A. M., & Wu, S. S. (2016). Metal powder absorptivity: modelling and experiment. *Applied Optics 55*, 6496-6500, doi:10.1364/AO.55.006496.

12. Brandes, E. A., & Brook, G. B. (1992). *Smithells Metals Reference Book Seventh Edition.* Woburn, MA: Butterworth-Heinemann.

13. Brandt, M., Sun, S., Leary, M., Feih, S., Elambasseril, J., & Liu, Q. (2013). High-value SLM aerospace components: from design to manufacture. *Advanced Materials Research 633*, 135-147.

14. Cengel, Y. A., & Ghajar, A. J. (2015). *Heat and Mass Transfer - Fundamentals & Applications, Fifth Edition.* New York: McGraw-Hill Education.

15. Cezairliyan, A., McClure, J. L., & Taylor, R. (1977). Thermophysical Measurements on 90Ti-9Al-4V Alloy Above 1450 K Using a Transient (Subsecond) Technique. *Journal of Research of the Nattional Bureau of Standards - A. Physics and Chemistry 81*, 251-256.

16. Chen, H., & Yan, W. (2020). Spattering and denudation in laser powder bed fusion process: multiphase flow modelling. *Acta Materialia 196*, 154-167. doi:https://doi.org/10.1016/j.actamat.2020.06.033

17. Chen, Q., Zhao, Y., Strayer, S., Zhao, Y., Aoyagi, K., Koizumi, Y., . . . To, A. C. (2021). Elucidating the Effect of Preheating Temperature on Mlet Pool Morphology Variation in Inconel 718 Laser Powder Bed Fusion via Simulation and Experiment. *Additive Manufacturing 37*. doi:https://doi.org/10.1016/j.addma.2020.101642

18. Cheng, B., Loeber, L., Willeck, H., Hartel, U., & Tuffile, C. (2019). Computational Investigation of Melt Pool Process Dynamics and Pore Formation in Laser Powder Bed Fusion. *Journal of Materials Engineering and Performance*, 6565-6578. doi:https://doi.org/10.1007/s11665-019-04435-y

19. COMSOL. (2021, 09 22). *COMSOL*. Retrieved from COMSOL: https://www.comsol.com/

20. Cook, P. S., & Murphy, A. B. (2020). Simulation of melt pool behaviour during additive manufacturing: Underlying physics and progress. *Additive Manufacturing Vol 31*.

21. Cunningham, R., Zhao, C., Parab, N., Kantzos, C., Pauza, J., Fezzaa, K., . . . Rollett, A. D. (2019). Keyhole threshold and morphology in laser melting revealed by ultrahigh-speed x-ray imaging. *Science 363*, 849-852. doi:10.1126/science.aav4687

22. Du, Y., You X, Qiao, F., Guo, L., & Liu, Z. (2019). A Model for Predicting the Temperature Field During Selective Laser Melting. *Results in Physics, 12*, 52-60.

23. Edwards, P., & Ramulu, M. (2014). Fatigue performance evaluation of selective laser melted Ti-6Al-4V. *Materials Science and Engineering: A 598*, 327-337.

24. Egry, I., Holland-Moritz, D., Navokovic, R., Ricci, E., Wunderlich, R., & Sobezak, N. (2010). Thermophysical Properties of Liquid AlTi-Based Alloys. *International Journal of Thermophysics*, 949-965.

25. Egry, I., Ricci, E., Novakovic, R., & Ozawa, S. (2010). Surface tension of liquid metals and alloys - Recent developments. *Advances in Colloid and Interface Science, 159*, 198-212.

26. Engineering Toolbox. (2003). *Rations of Specific Heat of Gases*. Retrieved November 15, 2020, from Engineering ToolBox: https://www.engineeringtoolbox.com/specific-heat-ratio-d_608.html

27. ESI. (n.d.). *ACE+ Suite*. Retrieved 09 22, 2021, from ESI: https://www.esi-group.com/products/computational-fluid-dynamics/ace-suite

28. Facchini, L., Magalini, E., Robotti, P., Molinari, A., Hoges, S., & Wissenbach, K. (2010). Ductility of a Ti-6Al-4V alloy produced by selective laser melting of prealloyed powders. *Rapid Prototyping Journal 16*, 450-459.

29. FLOW-3D. (n.d.). *FLOW-3D AM*. Retrieved 09 09, 2021, from FLOW-3D: https://www.flow3d.com/products/flow3d-am/

30. Ford, I. J., & Lee, T. L. (2001). Entropy production and destruction in models of material evaporation. *Journal of Physics D: Applied Physics 34*, 413-417.

31. Gibson, I., Rosen, D., & Stucker, B. (2015). *Additive Manufacturing Technologies.* New York: Springer.

32. Gong, H., Gu, H., Zeng, K., Dilip, J. J., Pal, D., Stucker, B., . . . Lewandowski, J. J. (2014). Melt Pool Characterization for Selective Laser Melting of Ti-6Al-4V Pre-alloyed Powder. *25th Annual International Solid Freeform Fabrication Symposium*, (pp. 256-267).

33. Gong, H., Rafi, K., Starr, T., & Stucker, B. (2013). The Effects of Processing Parameters on Defect Regularity in Ti-6Al-4V Parts Fabricated By Selective Laser Melting and Electron Beam Melting. *24th International Solid Freeform Fabrication Symposium*, (pp. 424-439). Austin, Texas.

34. Griebel, M., Dornseifer, T., & Neunhoeffer, T. (1998). *Numerical Simulation in Fluid Dynamics - A Practical Introduction.* Philadelphia: Society for Industrial and Applied Mathematics.

35. Gurtler, F. J., Karg, M., Leitz, K. H., & Schmidt, M. (2013). Simulation of Laser Beam Melting of Steel Powders using the Three-Dimensional Volume of Fluid Method. *Physics Procedia 41*, 881-886.

36. Harrison, N. J., Todd, I., & Mumtaz, K. (2015). Reduction of micro-cracking in nickel superalloys processed by selective laser melting: a fundamental alloy design approach. *Acta Materialia 94*, 59-68.

37. Huang, Y., Khamesee, M. B., & Toyserkani, E. (2016). A comprehensive analytical model for laser powder-fed additive manufacturing. *Additive Manufacturing Vol 12*, 90-99.

38. Jia, Q., & Gu, D. (2014). Selective laser melting additive manufacturing of Inconel 718 superalloy parts: densification, microstructure and properties. *Journal of Alloys and Compounds 585*, 713-721.

39. Kaschnitz, E., Reiter, P., & McClure, J. L. (2002). Thermophysical Properties of Solid and Liquid 90Ti-6Al-4V in the Temperature Rang from 1400 to 2300 K Measured by Millisecond and Microsecond Pulse-Heating Techniques. *International Journal of Thermophysics 23(1)*, 267-275. doi:10.1023/A:1013925715428

40. Kempen, K., Thijs, L., Humbeeck, J. V., & Kruth, J. P. (2015). Processing AlSi10Mg by selective laser melting: parameter optimisation and material characterisation. *Materials Science and Technology 31*, 917-923.

41. Khairallah, S. A., & Anderson, A. (2014). Mesoscopic Simulation Model of Selective Laser Melting of Stainless Steel Powder. *Journal of Material Processing Technology, 214 (11)*, 2627-2636.

42. Khairallah, S. A., Anderson, A. T., Rubenchik, A., & King, W. E. (2016). Laser powder-bed fusion additive manufacturing: Physics of complex melt flow and formation mechanisms of pores, spatter, and denudation zones. *Acta Materialia, 108*, 36-45.

43. Khairallah, S. A., Martin, A. A., Lee, J. R., Guss, G., Calta, N. P., Hammons, J. A., . . . King, W. E. (2020). Controlling interdependent meso-nanosecond dynamics and defect generation in metal 3D printing. *Science 368*, 660-665. doi:10.1126/science.aay7830

44. King, W. E., Barth, H. D., Castillo, V. M., Gallegos, G. F., Gibbs, J. W., Hahn, D. E., . . . Rubenchik, A. M. (2014). Observation of keyhole-mode laser melting in laser powder-bed fusion additive manufacturing. *Journal of Materials Processing Technology, Vol. 214*, 2915-2925.

45. Knapp, G. L., Mukherjee, T., Zuback, J. S., Wei, H. L., Palmer, T. A., De, A., & DebRoy, T. (2017). Building blocks for a digital twin of additive manufacturing. *Acta Materialia, 135*, 390-399.

46. Kumar, A., & Debroy, T. (2006). Toward a unified model to prevent humping defects in gas tungsten arc welding. *Welding Journal, 85(12)*.

47. Kumar, S., & Pityana, S. (2011). Laser-Based Additive Manufacturing of Metals. *Advanced Materials Research, Vol. 227*, pp. 92-95.

48. Lawrence Livermore National Laboratories. (n.d.). *ALE3D for Industry*. Retrieved 09 22, 2021, from Lawrence Livermore National Laboratories: https://ale3d4i.llnl.gov/#how-wrapper

49. Le, K. Q., Tang, C., & Wong, C. H. (2019). On the study of keyhole mode melting in selective laser melting process. *International Journal of Thermal Sciences, 145*.

50. Leuders, S., Thone, M., Riemer, A., Niendorf, T., Troster, T., Richard, H. A., & Maier, H. J. (2013). On the mechanical behaviour of titanium alloy TiAl6V4 manufactured by selective laser melting: fatigue resistance and crack growth performance. *International Journal of Fatigue 48*, 300-307.

51. Li, C., Guo, Y., Fang, X., & Fang, F. (2018). A scalable predictive model and validation for residual stress and distortion in selective laser melting. *CIRP Annals, 67 (1)*, 249-252.

52. Li, J. Z., Johnson, W. L., & Rhim, W.-K. (2006). Thermal expansion of liquid Ti-6Al-4V measured by electrostatic levitation. *Applied Physics Letters, 89*. doi:https://doi.org/10.1063/1.2349840

53. Li, R., Liu, J., Shi, Y., Wang, L., & Jiang, W. (2011). Balling behavior of stainless steel and nickel powder during selective laser melting process. *International Journal of Advanced Manufacturing Technology 59*, 1025-1035.

54. Li, R., Shi, Y., Liu, J., Yao, H., & Zhang, W. (2009). Effects of processing parameters on the temperature field of selective laser melting metal powder. *Powder Metallurgy and Metal Ceramics 48*, 186-195.

55. Li, Y., & Gu, D. (2014). Parametric analysis of thermal behavior during selective laser melting additive manufacturing of aluminum alloy powder. *Materials and Design 63*, 856-867.

56. Lia, F., Park, J., Tressler, J., & Martukanitz, R. (2017). Partitioning of laser energy during directed energy deposition. *Additive Manufacturing 18*, 31-39. doi:http://dx.doi.org/10.1016/j.addma.2017.08.012

57. Liu, B., Fang, G., Lei, L., & Liu, W. (2019). A New Ray Tracing Heat Source Model for Mesoscale CFD Simulation of Selective Laser Melting (SLM). *Applied Mathematical Modelling, 79*, 506-520. doi:https://doi.org/10.1016/j.apm.2019.10.049

58. Liu, Q., Elambasseril, J., Sun, S., Leary, M., Brandt, M., & Sharp, P. K. (2014). The effect of manufacturing defects on the fatigue behaviour of Ti-6Al-4V specimens fabricated using selective laser melting. *Advanced Materials Research 891-892*, 1519-1524.

59. Luo, Z., & Zhao, Y. (2018). A survey of finite element analysis of temperature and thermal stress fields in powder bed fusion Additive Manufacturing. *Additive Manufacturing, 21*, 318-332.

60. Majeed, M., Khan, H. M., & Rasheed, I. (2019). Finite element analysis of melt pool thermal characteristics with passing laser in SLM process. *Optik, 194*.

61. Makoana, N. W., Yadroitsava, I., Moller, H., & Yadroitsev, I. (2018). Characterization of 17-4PH Single Tracks Produced at Different Parametric Conditions towards Increased Productivity of LPBF Systems - The Effect of Laser Power and Spot Size Upscaling. *Metals 8*. doi:10.3390/met8070475

62. Malefane, L. B., du Preez, W. B., Maringa, M., & du Plessis, A. (2018). Tensile and high cycle fatigue properties of annealed Ti6Al4V (ELI) Specimens produced by direct metal laser sintering). *South African Journal of Industrial Engineering, 29*, 299-311.

63. Mills, K. (2002). *Recommended Values of Thermophysical Properties for Selected Commercial Alloys.* Woodhead Publishing.

64. Milosevic, N., & Aleksic, I. (2012). Thermophysical properties of solid phase Ti-6Al-4V alloy over a wide temperature range. *International Journal of Materials Research*, 707-714.

65. Mohr, M., Wunderlich, R., Novakovic, R., Ricci, E., & Fecht, H. (2020). Precise Measurements of Thermophysical Properties of Liquid Ti-6Al-4V (Ti64) Alloy On Board the International Space Station. *Advanced Engineering Materials,22*. doi:https://doi.org/10.1002/adem.202000169

66. Moukalled, F., Mangani, L., & Darwish, M. (2015). *The Finite Volume Method in Computational Fluid Dynamics* (Vol. 113). Springer. doi:10.1007/978-3-319-16874-6

67. Mukherjee, T., & DebRoy, T. (2019). A digital twin for rapid qualification of 3D printed metallic components. *Applied Materials Today, 14*, 59-65.

68. Mukherjee, T., Wei, H. L., De, A., & DebRoy, t. (2018). Heat and fluid flow in additive manufacturing Part I - Modeling of powder bed fusion. *Comput. Mater. Sci, 150*, 304-313.

69. Olleak, A., & Xi, Z. (2018). Finite Element Modeling of the Selective Laser Melting Process for Ti-6Al-4V. *Proceedings of the 29th Annual International Solid Freeform Fabrication Symposium - An Additive Manufacturing Conference*, (pp. 1710-1720).

70. OpenFOAM. (n.d.). *OpenFOAM*. Retrieved 09 22, 2021, from OpenFOAM: https://www.openfoam.com/

71. Paradis, P. F., & Yoda, S. (2002). Non-Contact Measurements of Surface Tension and Viscosity of Niobium, Zirconium, and Titanium Using an Electrostatic Levitation Furnace. *International Journal of Thermophysics 23*, 825-842.

72. Pavlyukevich, N. V., & Polezhaev, Y. V. (2011). *Accommodation coefficient*. Retrieved November 30, 2020, from THERMOPEDIA: http://thermopedia.com/content/286/#:~:text=Accommodation%20coefficient%20is%20a%20physical,solid%20or%20liquid%20body%20surface.

73. Rai, R., Burgardt, P., Milewski, J. O., Lienert, T. J., & DebRoy, T. (2008). Heat transfer and fluid flow during electron beam welding of 21Cr-6Ni-9Mn steel and Ti-6Al-4V alloy. *Journal of Physics D: Applied physics 42*, 025503. doi:10.1088/0022-3727/42/2/025503

74. Rai, R., Elmer, J. W., Palmer, T. A., & DebRoy, T. (2007). Heat transfer and fluid flow during keyhole mode laser welding of tantalum, Ti-6Al-4V, 304L stainless steel and vanadium. *Journal of Physics D: Applied Physics, 40*, 5753-5766. doi:10.1088/0022-3727/40/18/037

75. Rauniyar, S. K., & Chou, K. (2019). Melt Pool Analysis and Mesoscale Simulation of Laser Powder Bed Fusion Process (L-PBF) with Ti-6Al-4V Powder Particles. *JOM, 71 (3)*, 938-945.

76. Ridolfi, M. R., Folgarait, P., Battaglia, V., Vela, T., Corapi, D., & Di Schino, A. (2019). Development and calibration of a CFD-based model of the bed fusion SLM additive manufacturing process aimed at optimising laser parameters. *Proocedia Structural Integrity, 24*, 370-380.

77. Rohatgi, A. (2020, November). Retrieved from WebPlotDigitizer: https://automeris.io/WebPlotDigitizer

78. Royal Society of Chemistry. (n.d.). *Titanium*. Retrieved 08 2020, from Periodic Table: https://www.rsc.org/periodic-table/element/22/titanium

79. Safarian, J., & Engh, T. A. (2012). Vacuum Evaporation of Pure Metals. *Metallurgical and Materials Transactions A, 44A*, 747-753.

80. Schmon, A., Aziz, K., & Pottlacher, G. (2017). Density of liquid Ti-6Al-4V. *EPU Web of Conferences, 151*. doi:10.1051/epjconf/201715104003

81. Schneider, S., Egry, I., & Seyhan, I. (2002). Measurement of the Surface Tension of Undercooled Liquid Ti6Al4V by Oscillating Drop Technique. *International Journal of Thermophysics, 23*, 1241-1248.

82. Schoinochoritis, B., Chantzis, D., & Salonitis, K. (2015). Simulation of metallic powder bed additive manufacturing processes with the finite element method: A critical review. *Journal of engineering manufacture, 231 (1)*, 96-117.

83. Shellabear, M., & Nyrhila, O. (2004). DMLS - Development History and State of the Art. *LANE 2004 conference*, (p. 4). Erlangen, Germany.

84. Shi, B., Khairallah, S., Heo, T. W., Rolchigo, M., McKeows, J. T., & Matthews, M. J. (2019). Integrated Simulation Framework for Additively Manufactured Ti-6Al-4V: Melt Pool Dynamics, Microstructure, Solid-State Phase Transformation, and Microelastic Response. *JOM, 71 (10)*, 3640-3655.

85. Shipley, H., McDonnell, D., Culleton, M., Coull, R., Lupoi, R., O'Donnell, G., & Trimble, D. (2018). Optimisation of process parameters to address fundamental challenges during selective laser melting of Ti-6Al-4V: A review. *International Journal of Machine Tools and Manufacture, 128*, 1-20.

86. Simonelli, M., Tuck, C., Aboulkhair, N. T., Maskery, I., Ashcroft, I., Wildman, R. D., & Hague, R. (2015). A study on the laser spatter and the oxidation reactions during selective laser melting of 316L stainless steel, Al-Si10-Mg, and Ti-6Al-4V. *Metallurgical and Materials Transactions A: Physical Metallurgy and Materials Science 46*, 3842-3851.

87. Sun, S., Brandt, M., & Easton, M. (2017). Powder bed fusion Processes: an overview. In M. Brandt, *Laser Additive Manufacturing - Materials* (pp. 55-77). Duxford: Woodhead Publishing.

88. Tan, P., Shen, F., Li, B., & Zhou, K. (2019). A thermo-metallurgical-mechanical model for selective laser melting of Ti6Al4V. *Materials and Design, 168*. doi:10.1016/j.matdes.2019.107642

89. Tang, C., Le, K. Q., & Wong, C. H. (2020). Physics of humping formation in laser powder bed fusion. *International Journal of Heat and Mass Transfer 149*, 119172. doi:10.1016/j.ijheatmasstransfer.2019.119172

90. Thejane, K., Chikoska, S., & du Preez, W. B. (2017). Characterisation and monitoring of Ti6Al4V (ELI) Powder used in different Selective Laser Melting systems. *South African Journal of Industrial Engineering, 28(3)*, 161-171.

91. Tryggvason, G., Scardovelli, R., & Zaleski, S. (2011). *Direct Numerical Simulations of Gas-Liquid Multiphase Flows.* Cambridge University Press. doi:https://doi.org/10.1017/CBO9780511975264

92. Vilaro, T., Colin, C., & Bartout, J. D. (2011). As-Fabricated and heat-treated microstructures of the Ti-6Al-4V alloy processed by selective laser melting. *Metallurgical and Materials Transactions 42A*, 3190-3199.

93. Vinet, B., Garandet, J., Marie, B., Domergue, L., & Drevet, B. (2004). Surface Tension Measurements on Industrial Alloys by the Drop-Weight Method. *International Journal of Thermophysics, 25(3)*, 869-883.

94. von Allmen, M., & Blatter, A. (1995). *Laser-Beam Interactions with Materials - Physical Principles and Applications* (2 ed.). Springer. doi:https://doi.org/10.1007/978-3-642-57813-7

95. Weckman, D. C., Kerr, H. W., & Liu, J. T. (1997). The effect of process variables on pulsed Nd:YAG laser spot welds: Part II. AA1100 aluminium and comparison to AISI 409 stainless steel. *Metallurgical and Materials Transactions B, 28*, 687-700.

96. Weingarten, C., Buchbinder, D., Pirch, N., MeinersW, Wissenbach, K., & Poprawe, R. (2015). Formation and reduction of hydrogen porosity during selective laser melting of AlSi10Mg,. *Journal of Materials Processing Technology 221*, 112-120.

97. Wu, Y., San, C., Chang, C., Lin, H., Marwan, R., Baba, S., & Hwang, W. (2018). Numerical modeling of melt-pool behavior in selective laser melting with random powder distribution and experimental validation. *Journal of Materials Processing Technology, 254*, 72-78.

98. Wunderlich, R. K. (2008). Surface Tension and Viscosity of Industrial Ti-Alloys Measured by the Oscillating Drop Method on Board Parabolic Flights. *High Temperature Materials and Processes 27(6)*, 401-412.

99. Wunderlich, R. W., & Fecht, H.-J. (2005). Modulated electromagnetic induction calorimetry of reactive metallic liquids. *Measurement Science and Technology*, 402-416.

100. Xie, J., Kar, A., Rothenflue, J. A., & Latham, W. P. (1997). Temperature-dependent absorptivity and cutting capability of CO2, Nd:YAG and chemical oxygen-iodine lasers. *Journal of Laser Applications 9*, 77-85, doi:10.2351/1.4745447.

101. Yadroitsava, I., Els, J., Booysen, G., & Yadroitsev, I. (2015). Peculiarities of single track formation from Ti6Al4V alloy at different laser power densities by selective laser melting. *South African Journal for Industrial Engineering, 26*, 86-95.

102. Yadroitsev, I., & Yadroitsava, I. (2015). Evaluation of residual stress in stainless steel 316L and Ti6Al4V samples produced by selective laser melting. *Virtual and Physical Prototyping*, 67-76.

103. Yadroitsev, I., Gusarov, A., Yadroitsava, I., & Smurov, I. (2010). Single track formation in selective laser melting of metal powders. *Journal of Materials Processing Technology 210*, 1624-1631.

104. Yadroitsev, I., Krakhmalev, P., & Yadroitsava, I. (2014). Selective laser melting of Ti6Al4V alloy for biomedical applications: temperature monitoring and microstructural evolution. *Journal of Alloys and Compounds 583*, 404-409.

105. Yadroitsev, I., Yadroitsava, I., Du Plessis, A., & MacDonald, E. (2021). *Fundamentals of Laser Powder Bed Fusion of Metals.* Elsevier.

106. Ye, J., Khairallah, S. A., Rubenchik, A. M., Crumb, M. F., Guss, G., Roehling, J., . . . Matthews, M. J. (2019). Energy Coupling Mechanisms and Scaling Behavior Associated with Laser Powder Bed Fusion Additive Manufacturing. *Advanced Engineering Materials, 1900185*.

107. Yuan, P., & Gu, D. (2015). Molten pool behaviour and its physical mechanism during selective laser melting of TiC/AlSi10Mg nanocomposites: simulation and experiments. *Journal of Physics D: Applied Physics 48*, 035303.

108. Zhang, B., & Coddet, C. (2016). Selective laser melting of iron powder: observation of melting mechanism and densification behavior via point-track-surface-part research. *Journal of Manufacturing Science and Engineering, Transactions of the ASME 138*.

109. Zhou, K., & Wei, B. (2016). Determination of the thermophysical properties of liquid and solid Ti-6Al-4V alloy. *Applied Physics A, 122(3)*, 248.

110. Zhou, Y., Wen, S. F., Song, B., Zhou, X., Teng, Q., Wei, Q. A., & Shi, Y. S. (2016). A novel titanium alloy manufactured by selective laser melting: microstructure, high temperature oxidation resistance. *Materials & Design 89*, 1199-1204.

111. Zhuang, J., Lee, Y., Hsieh, W., & Yang, A. (2018). Determination of melt pool dimensions using DOE-FEM and RSM with process window during SLM of Ti6Al54V powder. *Optics and Laser Technology, 103*, 59-76.

Appendix A - Density

	A	B	C	D	E	F	G	H	I	J	K	L	M	N	O	P
1	Mills, 2002		Schmon, 2017		Tan, 2019		Mohr solid, 2020		Mohr Liquid, 2020		Li, 2006		Li Liquid, 2006		Used in study	
2	Temp [K]	[kg/m^3]	Temp [K]	[kg/m^3]	Temp [K]	[kg/m^3]	Temp [K]	[kg/m^3]	Temp [K]	[kg/m^3]	Temp [K]	[kg/m^3]	Temp [K]	[kg/m^3]	Temp [K]	[kg/m^3]
3	296,2521	4420,5	2 046	4030	296,2675	4418,9	1033,402	4316,2	1702,903	4131,2	1091,44	4382,222	1691,656	4186,853	297,3737	4421,4
4	372,0237	4406,7	2 050	4028	477,6295	4391	1092,64	4306,1	1773,858	4119,6	1166,475	4372,584	1754,002	4170,214	300	4420,9
5	472,7723	4395,8	2 100	4006	675,4816	4363,2	1128,481	4299,5	1835,201	4108,5	1243,196	4363,706	1816,254	4154,734	400	4404,7
6	574,4374	4382,6	2 150	3983	873,3337	4335,3	1124,98	4289,9	1886,303	4098,4	1322,101	4353,301	1879,563	4139,746	500	4392,8
7	673,3204	4367,4	2 200	3961	1071,179	4300,4	1120,382	4272,7	1932,688	4087,5	1396,124	4341,469	1941,38	4121,889	600	4379,8
8	774,0503	4351,5	2 250	3938	1269,031	4272,5	1155,824	4260,1			1469,06	4330,202	1974,949	4111,517	700	4364,7
9	873,8618	4337,3	2 300	3915	1475,135	4251,7	1217,02	4249,9			1547,045	4316,905			800	4348,9
10	974,6053	4324,9	2 350	3893	1681,232	4223,8	1304,656	4241			1621,966	4303,578			900	4334,6
11	1074,414	4310	2 400	3870	1870,839	4195,9	1402,734	4231,5			1698,997	4289,666			1000	4322,3
12	1175,149	4295,3	2 450	3848	1924,152	3924,1	1499,562	4221,6			1772,48	4277,048			1008,51	4319,7
13	1268,493	4282,4	2 500	3825	2175,449	3752,5	1585,629	4211,6			1843,334	4262,214			1050	4313,4
14	1373,849	4267,4	2 550	3802	2776,918	3345,4	1665,598	4201,9			1909,929	4247,145			1100	4303,9
15	1473,66	4253	2 592	3783	3250,674	3021,7	1741,327	4191,6							1116,409	4274
16	1574,402	4240,3					1799,703	4182,6							1122,888	4266,9
17	1673,286	4225,3					1856,813	4172,8							1150	4261,1
18	1774	4205,1					1905,2	4163,4							1200	4251,8
19	1872,913	4197,9													1300	4241,5
20	1935,201	3911,8													1400	4231,5
21	1976,223	3886,5													1500	4221,5
22	2072,134	3819													1600	4210,2
23	2171,738	3750,1													1700	4198,1

	A	B	C	D	E	F	G	H	I	J	K	L	M	N	O	P
1	Mills, 2002		Schmon, 2017		Tan, 2019		Mohr solid, 2020		Mohr Liquid, 2020		Li, 2006		Li Liquid, 2006		Used in study	
2	Temp [K]	[kg/m^3]	Temp [K]	[kg/m^3]	Temp [K]	[kg/m^3]	Temp [K]	[kg/m^3]	Temp [K]	[kg/m^3]	Temp [K]	[kg/m^3]	Temp [K]	[kg/m^3]	Temp [K]	[kg/m^3]
24															1800	4182,8
25															1900	4165,7
26															1921,252	4159,8
27															1924,706	4085,7
28															1950	4074,7
29															2050	4028
30															2100	4006
31															2200	3961
32															2300	3915
33															2400	3870
34															2500	3825
35															2600	3779,6
36															2700	3734,4
37															2800	3689,1
38															2900	3643,9
39															3000	3598,7
40															3100	3553,5
41															3200	3508,3
42															3300	3463
43															3315	3456,3
44																

Appendix B - Viscosity

	A	B	C	D	E	F	G	H	I	J	K	L	M	N	O	P
1	Mills, 2002		Wunderlich, 2008		Mohr, 2020		Wunderlich, 2005		Paradis equation		Lu, 2017 CPTi		Wunderlich, 2008 extr		Used in study	
2	Temp [K]	[kg/ms]	Temp [K]	[kg/ms]	Temp [K]	[kg/ms]	Temp [K]	[kg/ms]	Temp [K]	[kg/ms]	Temp [K]	[kg/ms]	Temp [K]	[kg/ms]	Temp [K]	[kg/ms]
3	1923	0,00325	1735,629	0,0363	1709,792	0,008231	1943	0,00482	1750	5,70731	2050,259	0,003243035	1735,629	0,0363	1900	0,004425
4	1973	0,00303	1747,085	0,034302	1771,813	0,006217	2097	0,00392	1800	5,37381	2093,803	0,003021424	1747,085	0,034302	1950	0,00398
5	2073	0,00266	1766,047	0,031858	1807,927	0,0056			1850	5,04031	2143,697	0,00279675	1766,047	0,031858	2000	0,00362
6	2173	0,00236	1788,17	0,029285	1830,891	0,005702			1900	4,70681	2193,591	0,002602712	1788,17	0,029285	2050	0,00333
7			1813,452	0,026852	1837,564	0,004674			1950	4,37331	2243,939	0,002431143	1813,452	0,026852	2100	0,00309
8			1842,686	0,024797					2000	4,03981	2293,833	0,002277956	1842,686	0,024797	2200	0,00274
9			1871,919	0,023129					2050	3,70631	2344,614	0,002143449	1871,919	0,023129	2300	0,00246
10			1908,263	0,021471							2393,395	0,002020601	1908,263	0,021471	2400	0,00223
11			1939,076	0,020567							2443,516	0,001912349	1939,076	0,020567	2500	0,00203
12			1970,68	0,019802							2476,855	0,001844873	1970,68	0,019802	2600	0,00187
13			1998,333	0,019422									1998,333	0,019422	2800	0,0017
14			2024,406	0,019042									2024,406	0,019042	3000	0,00165
15			2052,059	0,018662									2052,059	0,018662	3200	0,00162
16			2078,131	0,01841									2078,131	0,01841	3315	0,00161
17													2100	0,01825		
18													2200	0,0176		
19													2300	0,01705		
20													2400	0,01655		
21													2500	0,0161		
22													2600	0,0157		
23													2700	0,01535		
24													2800	0,01505		
25													2900	0,0148		
26													3000	0,0146		
27													3100	0,01445		
28													3200	0,014325		
29													3300	0,014225		
30													3400	0,014125		

Appendix C – Thermal Conductivity

	A	B	C	D	E	F	G	H	I	J	K	L	M	N
1	Mills, 2002		Boiveneau, 2006		Mohr, 2020		Mohr Liquid, 2020		Milosevic, 2012		Uncertain		Used in study	
2	Temp [K]	[W/mK]	Temp [K]	[W/mK]	Temp [K]	[W/mK]	Temp [K]	[W/mK]	Temp [K]	[W/mK]	Temp [K]	[W/mK]	Temp [K]	[W/mK]
3	297,6011	6,962312	431,7473	5,809914	1012,859	13,51692	1060,479	30,40466	194	5	304,1271	6,15171	298	6,7
4	372,7783	7,436965	509,3364	6,725988	1054,555	14,07607	1675,505	25,37585	214	5,2	405,8666	7,507344	500	8,3
5	473,1644	8,788533	586,9255	7,622338	1105,95	15,06227	1694,77	25,99804	233	5,4	507,6061	8,862978	680	10,1
6	573,5495	10,13474	664,5145	8,554847	1129,973	16,57112	1709,92	26,23973	248	5,6	609,3455	10,22259	860	11,9
7	672,6549	11,34546	742,1036	9,454485	1144,702	16,81132	1725,07	26,46809	273	6	711,085	11,57822	1012,859	13,51692
8	773,0177	12,58516	819,6927	10,36727	1187,078	17,54212	1740,219	26,71562	287	6,1	812,8245	12,93783	1026,681	13,6904
9	874,7012	14,15726	897,2817	11,35895	1228,232	18,32445	1755,368	26,96478	296	6,3	914,564	14,29744	1041,116	13,95967
10	975,0817	15,48201	974,8708	12,37692	1272,513	18,97342	1770,519	27,1821	322	6,6	1016,303	15,65307	1054,555	14,07607
11	1073,153	17,7349	1052,46	13,4212	1316,449	19,77454	1785,667	27,44815	372	7,2	1118,043	17,01268	1072,13	14,5186
12	1175,005	20,11228	1130,049	14,53121	1362,133	20,51647	1800,815	27,72719	419	7,9	1219,782	18,36832	1089,409	14,75567
13	1268,127	22,63387	1207,638	15,68724	1403,839	21,37231	1815,964	27,97374	477	8,7	1321,522	19,72793	1105,95	15,06227
14	1268,672	19,24789	1283,871	17,12695	1445,329	21,99845	1831,113	28,22192	519	9,2	1423,261	21,08754	1118,355	16,15232
15	1372,879	20,91857	1348,709	18,71503	1489,609	22,54871	1846,262	28,47788	569	9,7	1525,001	22,44715	1129,973	16,57112
16	1473,378	22,81414	1403,021	20,20582	1535,219	23,4091	1861,412	28,71751	612	10,3	1626,74	23,80676	1144,702	16,81132
17	1572,398	23,61341	1479,2	21,36214	1581,1	24,09371	1876,561	28,97513	656	11,1	1728,48	25,17034	1187,078	17,54212
18	1672,689	24,50908	1556,789	22,46558	1625,036	24,76233	1891,71	29,22428	714	11,9	1830,219	26,52598	1228,232	18,32445
19	1773,043	25,70511	1634,378	23,58875	1666,56	25,44207	1905,908	29,40606	765	12,4	1928,876	28,63695	1272,513	18,97342
20	1870,894	26,90141	1711,967	24,64288	1727,209	26,22045	1922,011	29,66113	812	13,1	2030,615	30,35833	1316,449	19,77454
21	1926,384	33,47651	1789,556	25,75618	1774,381	26,9449	1937,164	29,84583	858	14	2132,355	32,02007	1362,133	20,51647
22	1972,588	34,52459	1867,145	26,89079	1818,949	27,6165	1948,873	29,97391	905	14,3	2234,094	33,68977	1403,839	21,37231

	A	B	C	D	E	F	G	H	I	J	K	L	M	N
1	Mills, 2002		Boiveneau, 2006		Mohr, 2020		Mohr Liquid, 2020		Milosevic, 2012		Uncertain		Used in study	
2	Temp [K]	[W/mK]	Temp [K]	[W/mK]	Temp [K]	[W/mK]	Temp [K]	[W/mK]	Temp [K]	[W/mK]	Temp [K]	[W/mK]	Temp [K]	[W/mK]
23			1915,706	28,42672	1865,048	28,24505			924	14,7	2335,834	35,35151	1445,329	21,99845
24			1994,109	29,9565	1912,258	28,95318	m	0,015627	954	16,2	2437,573	37,02518	1489,609	22,54871
25			2032,903	30,65121			c	-0,48157	998	17,4	2539,313	38,68693	1535,219	23,4091
26			2071,698	31,27689					1051	18,6	2641,052	40,35662	1581,1	24,09371
27			2145,76	32,59847			2000	30,77288	1105	20	2742,792	42,02632	1625,036	24,76233
28			2223,349	33,92743			2200	33,89832	1144	21	2844,531	43,69204	1666,56	25,44207
29			2300,938	35,33			2400	37,02377	1169	22,5	2946,271	45,36174	1727,209	26,22045
30			2378,528	36,67669			2600	40,14921	1194	26,2	3048,01	47,02348	1774,381	26,9449
31			2450,474	38,15325			2800	43,27465	1237	32	3149,75	48,69318	1818,949	27,6165
32			2526,652	39,54408			3000	46,4001	1283	42,7	3246,865	50,27243	1865,048	28,24505
33			2604,241	40,90063			3200	49,52554	1312	35,2			1912,258	28,95318
34			2669,487	42,16725			3400	52,65099	1380	25,5			1948,873	29,97391
35			2800	44,43061					1430	25,2			2000	30,77288
36			3100	49,83389					1478	26,2			2200	33,89832
37			3400	55,23717					1532	27			2400	37,02377
38													2600	40,14921
39			m=	0,018011									2800	43,27465
40			c=	-6									3000	46,4001
41													3200	49,52554
42													3400	52,65099
43														

Appendix D – Specific heat

	A	B	C	D	E	F	G	H	I	J	K	L	M	N	O	P	Q	R
1	Mills, 2002		Boivineau, 2006		Mohr, 2020		Mohr Liquid, 2020		Basak, 2003		Cezairliyan, 1977		Kaschnitz, 2002		Milosevic, 2012		Used in study	
2	Temp [K]	[J/kgK]	Temp [K]	[J/kgK]	Temp [K]	[J/kgK]	Temp [K]	[J/kgK]	Temp [K]	[J/kgK]	Temp [K]	[J/kgK]	Temp [K]	[J/kgK]	Temp [K]	[J/kgK]	Temp [K]	[J/kgK]
3	298,15	546	453,2174	610,6116	1615,002	767,3285	1764,79	942,9682	397,9447	619,9294	1401,403	724,9369	1401,403	730,0509	193,4186	490,5432	300	535
4	373,15	562	501,2806	619,6477	1624,406	769,2314	1771,207	943,0666	447,61	639,1894	1451,902	731,2529	1451,101	731,8933	250,7009	514,176	400	566
5	473,15	584	550,946	639,2308	1633,004	769,5669	1776,214	943,766	498,0764	659,7879	1500,799	736,346	1500,799	736,3152	271,9736	523,7525	500	599
6	573,15	606	602,2134	639,3461	1642,677	773,1552	1784,543	943,766	549,3439	680,1219	1550,497	742,9528	1549,695	743,3164	300,029	535,1438	600	627
7	673,15	629	651,8788	649,4635	1652,618	775,6625	1793,679	943,766	599,0092	700,0797	1600,195	752,3521	1600,195	752,9101	349,7271	550,032	700	649
8	773,15	651	699,942	669,078	1660,947	777,7519	1802,814	943,766	648,6746	709,5513	1652,298	762,5503	1652,298	761,2869	399,4252	566,7023	800	671
9	873,15	673	750,4084	680,2206	1670,352	780,962	1811,949	943,766	700,7431	729,4698	1701,194	776,0694	1699,591	774,5455	449,1233	580,9853	900	693
10	973,15	694	800,8748	639,8993	1677,928	782,3866	1821,211	944,0341	748,8063	748,9383	1751,694	790,0653	1750,893	790,693	498,8214	599,3672	1000	735
11	1073,15	714	850,5402	649,0108	1687,547	785,4448	1830,22	943,766	798,4717	779,6087	1802,194	809,3936	1799,789	806,8455	550,1226	611,3943	1100	790
12	1173,15	734	900,2055	739,1622	1696,414	789,6806	1839,356	944,4172	848,9381	809,5242	1851,892	827,8686	1850,289	827,7915	599,8207	626,8257	1200	950
13	1268,15	753	951,473	728,4161	1705,818	793,1376	1848,491	944,9056	897,8024	859,2061			1923	931	649,5188	633,506	1250	1150
14	1373,15	660	1001,138	747,9636	1717,013	797,7914	1857,761	944,8582	949,8709	909,6989			2200	931	700,0185	648,6288	1275	1126
15	1473,15	678	1050,804	756,4465	1723,283	800,8622	1866,762	945,8825	997,1331	969,4386					750,5181	659,2209	1300	1053
16	1573,15	696	1099,668	767,3543	1733,314	803,2049	1875,36	946,2733	1047,599	1048,912					800,2162	671,1988	1400	759
17	1673,15	714	1150,134	899,096	1741,822	807,5736	1885,032	946,0453	1098,867	1109,544					849,1127	682,1496	1500	765
18	1773,15	732	1199,8	1128,655	1750,958	811,9899	1893,093	945,4755	1146,129	1138,418					901,2156	693,6028	1600	771
19	1873,15	750	1222,229	1168,645	1761,974	818,2692			1250,266	1019,61					948,5089	710,444	1700	791
20	1923,15	831	1251,868	850,1176	1768,422	821,6298			1398,461	779,8524					1000,612	735,9409	1800	844

	A	B	C	D	E	F	G	H	I	J	K	L	M	N	O	P	Q	R
1	Mills, 2002		Boivineau, 2006		Mohr, 2020		Mohr Liquid, 2020		Basak, 2003		Cezairliyan, 1977		Kaschnitz, 2002		Milosevic, 2012		Used in study	
2	Temp [K]	[J/kgK]	Temp [K]	[J/kgK]	Temp [K]	[J/kgK]	Temp [K]	[J/kgK]	Temp [K]	[J/kgK]	Temp [K]	[J/kgK]	Temp [K]	[J/kgK]	Temp [K]	[J/kgK]	Temp [K]	[J/kgK]
21	1973,15	831			1777,02	826,3784			1448,928	784,3306					1047,905	771,6372	1900	916
22	2073,15	831	1923	1126	1785,349	831,2221			1497,792	783,8382					1100,008	809,2766	1923	940
23	2200	831	2200	1126	1798,515	839,7917			1548,258	784,0761					1150,508	862,1863	2000	940
24					1803,083	844,7559			1599,526	789,9336					1174,555	893,0401	2100	940
25									1646,788	788,9879					1198,603	968,2077	2200	940
26									1696,453	794,3858					1225,856	1044,12		
27									1747,721	793,8981					1249,904	1201,069		
28									1798,187	799,0297					1274,753	1509,547		
29															1299,602	1257,049		
30															1324,451	992,9719		
31															1350,102	906,4996		
32															1375,752	789,3566		
33															1399,8	745,5428		
34															1451,101	750,118		
35															1498,394	746,0195		
36															1549,695	756,6741		
37															1598,592	753,9822		
38															1649,092	756,1929		
39																		

Appendix E – Model setup

Setup of a single-track model without powder

The default workflow of the FLOW-3D software was studied before setting up the numerical model. The first tab in this workflow is the Global settings. In the Global settings, the following settings were selected. Firstly, the SI unit system was selected. Secondly, the pressure type, which could be switched between absolute and relative, was set to absolute pressure, the reference pressure set to 100 kPa, and the reference temperature to 273,15 K. In this window, the finish time for each simulation was set as well. This depended on the specific process parameters and varied with a change in scanning speed. Time was allowed for solidification after every single track was created.

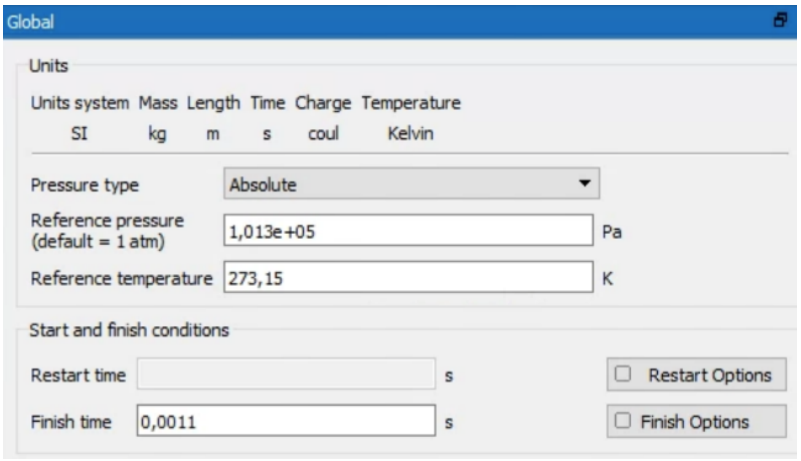

Figure 54: Global window of the simulation software, where the unit system, pressure type, reference values and simulation times are selected

The second tab in the workflow is the Physics tab. In this tab, all physics relevant to this simulation was added. Before adding the relevant physics models, a choice between a single- or two-fluid simulation approach had to be made. For this model, a single fluid simulation approach was selected. The area above the substrate where the air occurs is referred to as the void in the software. Utilising this approach, it followed that the incompressible flow mode would be selected. This can be seen in Figure 55.

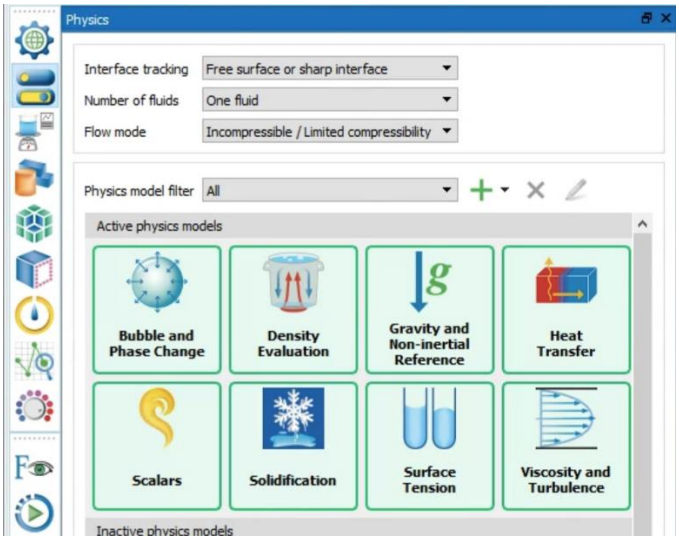

Figure 55: Physics window, where all relevant physics models were activated and a single-fluid approach selected

After these selections, the first model that was activated was the bubble and phase change model. For this simulation, constant pressure bubbles with vaporisation were selected. When selecting this option, the following information is required. Firstly, the ratio of specific heats for the vapour. This was set to 1.66. The pressure of the void was set to 100 kPa. The convective heat transfer coefficient between the void and the metal was set to 50 W/m^2K, and an accommodation coefficient for evaporation was set to 0.5.

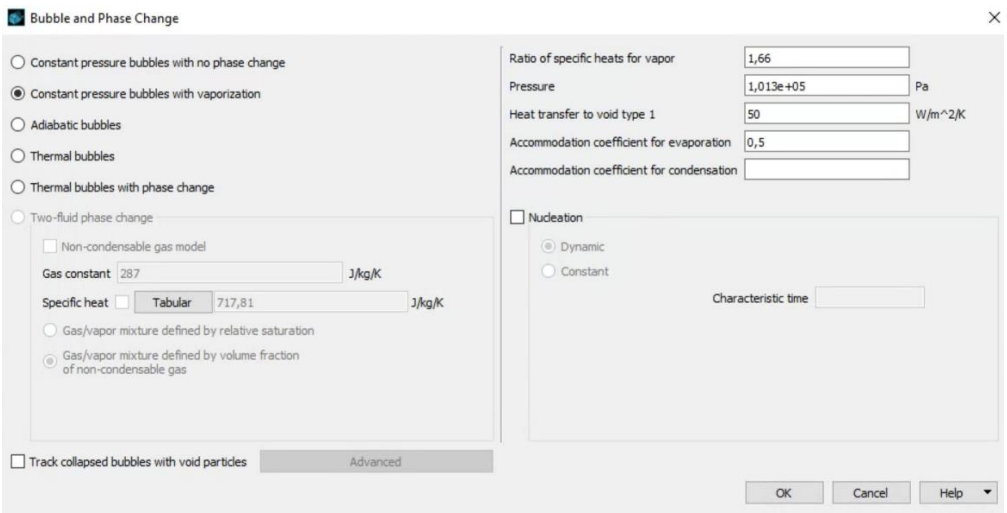

Figure 56: Bubble and phase change model parameter selection window

Secondly, the density evaluation option was turned on to account for the dramatic change in the density of the material over a wide range of temperatures. Enabling the density

evaluation option comes with the possibility of including the effects of volumetric thermal expansion in the simulation. It was decided to include this effect in the simulation.

Thirdly, gravity was enabled and set as -9.81m/s^2 on the z-axis. Next, heat transfer and first-order fluid internal energy advection were enabled. Fluid-to-solid heat transfer was also enabled. The simulation of viscous heating was left disabled.

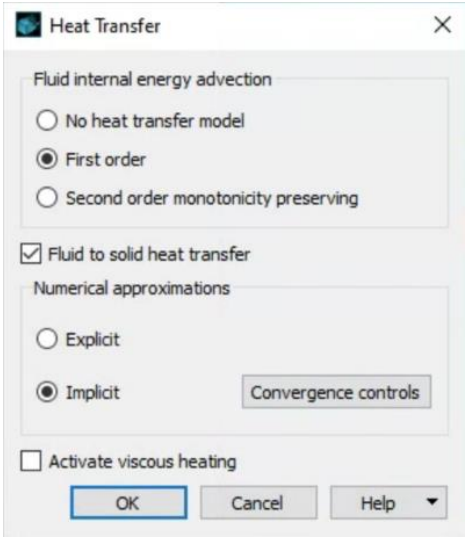

Figure 57: Heat transfer model parameter selection window

The solidification model was then activated. This model includes various sub-models that can be activated, including thermal stress evolution, shrinkage, binary alloy segregation, and microporosity. All of these models were left deactivated. It should be noted that many of these models were developed for the simulation of metal castings and are, therefore, not integral to this study. However, investigating the evolution of thermal stresses is an exciting possibility for other studies.

Next, the surface tension model was activated, with the surface tension coefficient set to 1,493 N/m at a reference temperature of 1923 K and the temperature dependence coefficient to -0.0004 N/mK. Lastly, the viscosity and turbulence model was activated. The simulation of viscous flow was enabled. Various turbulence options were available, most notably laminar flow, k-epsilon turbulence and k-omega turbulence models. Both laminar flow and k-epsilon turbulence models were utilised, though it turned out that the effect of the turbulence model used on the dimensions of the melt pool was negligible for the mesh size used.

These were all the physics models that were activated in the Physics window. The next window in the software, Fluids, was used to import the relevant material properties. This included temperature-dependent density, thermal conductivity, specific heat, viscosity and solidus and liquidus temperatures. The reference temperature for all of these parameters was selected as the liquidus temperature of Ti6Al4V at 1923 K.

No changes were made to the tab for Geometry, as no additional geometries needed to be imported or created for the simulation without powder. This is, however, not the same for simulations with powder. The details for this are discussed in the section for the setup of a model with powder on page 135.

The following tab in the workflow was the Meshing tab. The simulation domain was set up in this tab, and the cell size selection was made. The setup of the mesh can be seen in Figure 58. A non-conforming mesh was used. It was decided to use a mesh with various meshing planes, with different planes denoting different cell sizes. If the cell size between two adjacent planes differed, the cell size was increased gradually from one plane to the next. This can be seen in Figure 58.

It was decided to use a cell size of 5 µm for the innermost mesh planes. Upon recommendation in the simulation software documentation, it was decided to use a cell size four times larger than the inner cells (20 µm) for the outer mesh planes to capture heat diffusion further away from the melt pool. This can be seen in Figure 58. This figure shows the finer mesh between the innermost meshing planes and a coarser mesh along the edges to account for thermal diffusion.

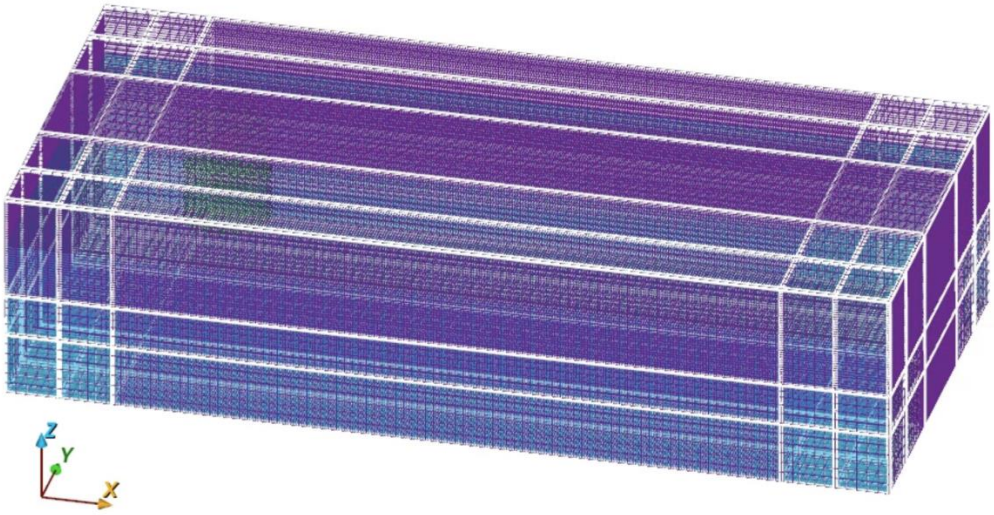

Figure 58: Graphical representation of the setup of the mesh

For selecting the width of the y-axis of the mesh, the recommendation made in the simulation software documentation was followed to create an inner mesh twice the width of the expected melt pool. This was equal to 400 µm for the keyhole process parameters and 240 µm for all other process parameters. The length of the melt pool was selected after preliminary simulations revealed that the single-track melt pool reached a steady state well before 1000 µm. It was, therefore, decided to use a scanning track length of 1000 µm. This resulted in an inner mesh length of 1400 µm for the keyhole parameter set and 1240 µm for all other parameter sets. The additional 400 and 240 µm, respectively, accounted for the spot diameter of the laser melting the substrate before the starting point and beyond the endpoint of the laser path. Lastly, on the z-axis, only four meshing planes were used, as there was no thermal conduction to account for at the top of the domain. The inner mesh was extended 100 µm above the surface of the substrate to accurately capture the movement of the melt above the substrate, as well as 300 µm below the surface for the keyhole parameter set and 100 µm below the surface for all other parameter sets, as this was sufficient to capture the entire melt pool.

After the mesh was set up, the next tab in the workflow was used to set up boundary conditions for the mesh. The upper boundary was set up as a constant pressure outflow boundary at atmospheric pressure and a temperature of 293 K. All other boundaries were set up as walls with no in- or out-flow at a constant temperature of 293 K.

Following the setup of the boundary conditions, the initial conditions for the simulation were set up in the next workflow tab. First, a fluid region was added to the mesh to define

the region where the substrate was located. As almost the entire mesh consisted of a Ti6Al4V substrate, only a z-axis limit was introduced 100 µm below the top plane of the mesh. Next, to indicate to the simulation software the location of the void above the substrate, a void pointer was added in this 100 µm region above the substrate. All these can be seen in Figure 59. After the fluid and void regions had been initialised, the initial temperature of both the fluid and the void regions was set to 293 K, and the initial pressure of the void was set to atmospheric pressure.

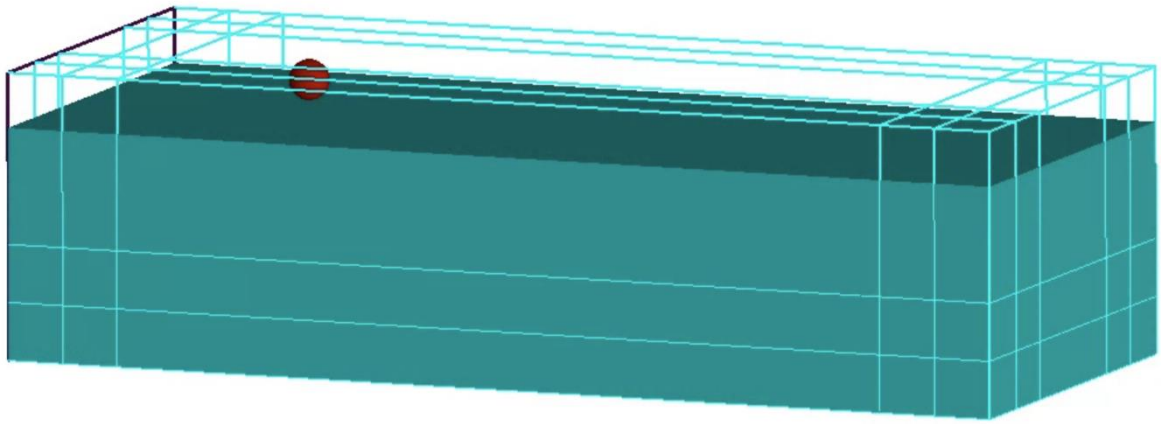

Figure 59: Initialisation of the fluid region (blue) and void pointer (red). The meshing planes can also be seen (light blue lines)

In the Output tab, no parameters that affect the outcome of the simulations could be changed. Parameters such as the simulation time interval for data output could be changed here and modified according to the specific interest at that point.

Lastly came the Numerics tab. In this tab, various changes were made. Firstly, the volume-of-fluid (VOF) advection was changed from automatically determined to using the Split Lagrangian method. Next, under advanced options of the volume of fluid advection method, the removal of isolated fluid droplets was enabled. A coefficient of 0.1 was used here to remove these fluid droplets. This coefficient is dependent on the cell size used and was determined by trial and error.

The following value was changed under the pressure solver option, accessed by clicking the convergence controls button. By default, a dynamically adjusted convergence criterion is activated for pressure iterations. This dynamically adjusted convergence criterion was changed to a constant convergence criterion of 0.1.

Lastly, inside the same window for pressure convergence controls, the GMRES subspace size was changed for simulations where excessive pressure iterations took place with the default GMRES subspace size. This specifically took place for the simulation of keyhole parameters with powder. The GMRES value is 15 by default for all simulations and was increased to 30 for the keyhole parameter simulation. This, however, increased the computation time required.

The foregoing was everything that was set up in the main FLOW-3D program. The FLOW Weld User Interface (UI) was used to add the application of the laser to the substrate. To do this, the already-created simulation was right-clicked and unloaded in the FLOW-3D main program. Next, the FLOW Weld UI was opened, and the simulation setup file was loaded in this UI.

First, the laser tab was opened, and a new laser was added. The position of this origin was given as the origin of the x- and y-axis and 410 mm above the origin of the z-axis. Next, the shape of the laser was defined as circular. The focal distance was set as 410 mm.

Subsequently, the lens radius, spot radius and Gaussian distance of the laser beam were required by the software. Now, the spot diameter of the laser beam used in experimental work is equal to 80 µm. However, when investigating the definition of a laser with a spot diameter of 80 µm, this refers to the $1/e^2$ diameter of a beam with a Gaussian distribution. What this means is that the diameter of the beam is measured by finding the points in the Gaussian distribution where the relative intensity of the beam reaches $1/e^2$ or 13,53% of the maximum relative intensity. This is shown in Figure 60. This means that if a spot radius of 40 µm is selected in the simulation software, energy deposited outside this diameter will not be taken into consideration. A graphical representation of this can be seen in Figure 60. In this figure, modified refers to the distribution of the beam currently used in simulation, and standard refers to the beam profile that would be employed in the simulation software if no corrective action was taken

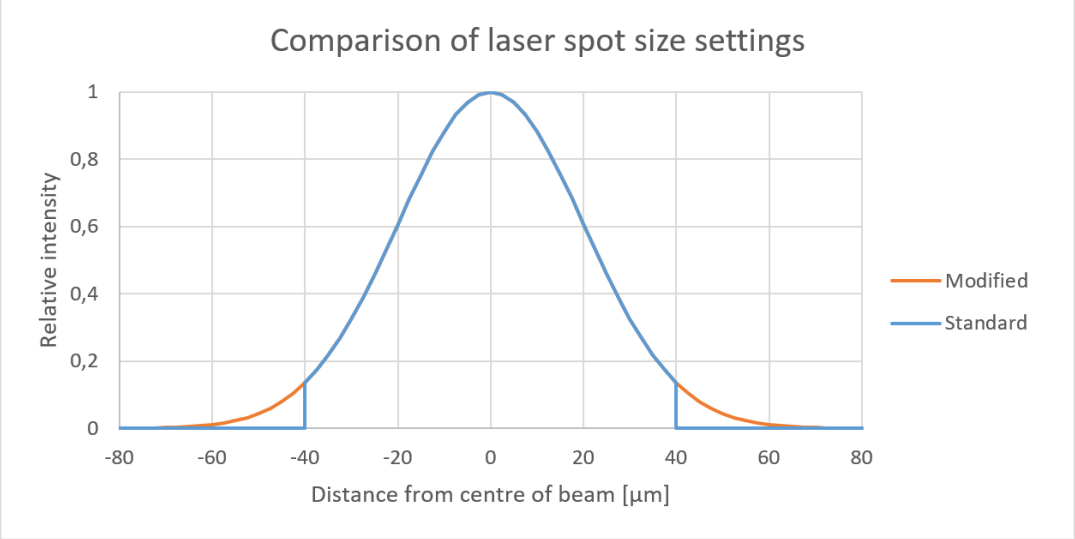

Figure 60: Explanation of the spot size of an 80 µm laser beam.

Taking the abovementioned into consideration, it was decided to calculate the Gaussian distance according to a spot radius of 40 µm. This is simply done by dividing the spot radius by $\sqrt{2}$ to obtain a Gaussian distance of 28.28 µm and then change the spot radius to 80 µm to account for the lost heat flux shown in Figure 60. This results in a laser with a Gaussian distribution and a $1/e^2$ spot size of 80 µm.

Next, the inputs for the power and scanning speed of the laser beam had to be filled in. For the simulation software, a tabular input for power and velocity over time had to be given. To determine the time at which the laser had to be shut off, the simple equation $(t = s/v)$ is used with the symbol *s* standing for the displacement and *v* for the scanning speed. This value is different for every parameter set. An example of such a tabular input can be seen in Figure 61.

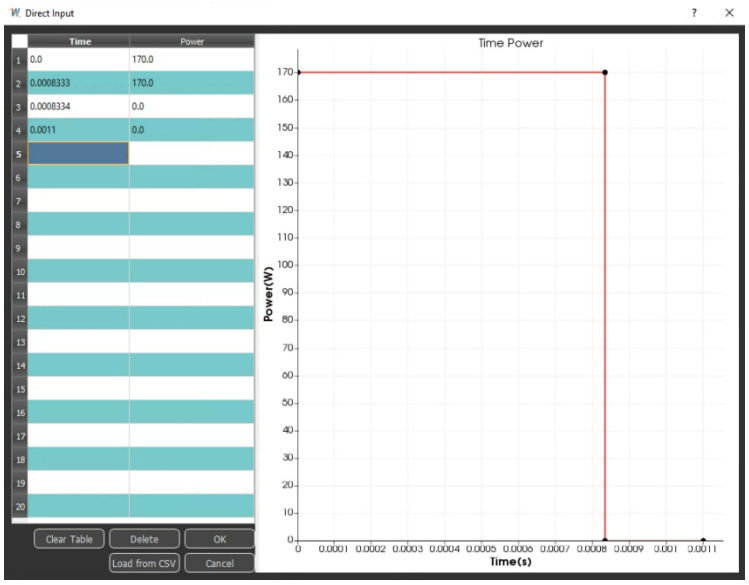

Figure 61: Tabulated input values over time used for the power and scanning speed of the laser

Lastly, after navigating to the Materials tab, the A and B evaporation pressure coefficients had to be set. The software has the option to calculate the evaporation pressure coefficients automatically. The B coefficient was calculated using the built-in function. The A coefficient had to be a fraction of the atmospheric pressure of 100 kPa. As this value was still unknown, it was initially chosen to be 50 000. However, this value varied substantially throughout the investigation and is indicated together with the relevant results.

After all these values were selected, the appropriate features were activated as outputs so that these could be investigated and analysed after the simulation was completed. These included the melting distance in the x-, y- and z-directions, as well as the heat flux by the laser beam and the melt region. All changes were saved, the FLOW Weld UI closed, the simulation loaded into the main FLOW-3D software again, and the simulation was run.

Setup of a single-track model with powder

The previous section explained the complete process for setting up a simulation without powder. A few additional steps were required to set up a simulation with powder. Only the additional required steps will be mentioned, as all steps mentioned in the previous section were still required for the setup.

The first step in creating a simulation with powder was the creation of the powder bed itself. This was done by creating a new simulation in the main FLOW-3D software. The

Global setting remained the same as previously mentioned. In the Physics tab, only two physics models were activated. These were gravity and particles.

In the Particles window, under the Mass tab, mass particles were enabled. Seven species of mass particles were created to account for the particle size distribution (PSD) of the particles that were used. The concentration of the different particles was set at a later time and is discussed later in this section. The information for the particle sizes that were used was obtained from Thejane et al. (2017). The total number of particles was set as 11500. This number was determined by running various simulations until a powder layer height of more than 70 µm was obtained, which was required for the particle spreading.

Next, in the Fluids tab, material property values for air at 15 °C were loaded. Subsequently, in the Geometry tab, a stereolithography (STL) file created in CAD software was added to the simulation for particles to settle on when falling. This geometry had a lip of 50 µm where the particles could settle. This geometry can be seen in Figure 62. After this, the Meshing tab was used to create the mesh inside which the particles were to be placed, and the simulation took place. The mesh dimensions of 3600 x 760 x 300 µm can also be seen in Figure 62.

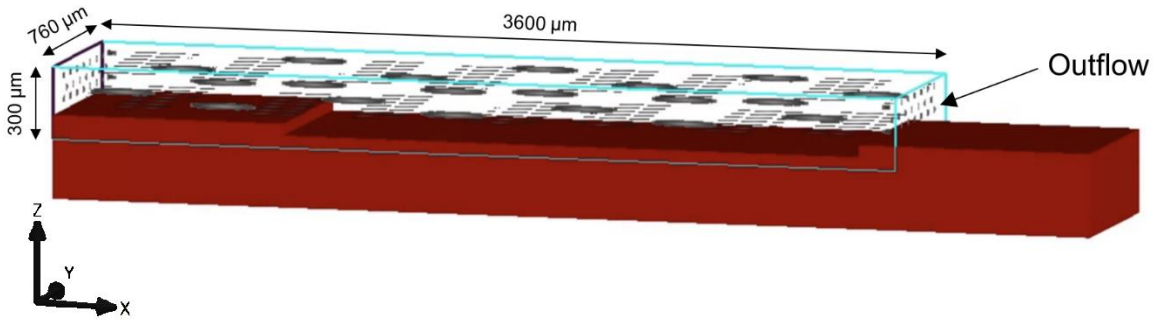

Figure 62: Geometry and mesh used for the particle-settling and particle-spreading simulations

Lastly, the boundary conditions for the simulation were set up. The y-boundaries and x-min boundaries were set up as walls. The x-max boundary was set up as an outflow. This was done so that particles could flow out at this end in the simulation that followed. The z-axis boundary conditions were irrelevant for this simulation and were left as per the default setting.

This was all the setup that was required in the main FLOW-3D software. After this, the simulation was unloaded, FLOW DEM UI opened, and the simulation loaded in the DEM

UI. Here, after navigating to the DEM tab, the spring constant for the particles was automatically calculated using the software, and a coefficient of restitution in both the normal- and tangential directions of 0,3 was used according to the recommendations of a FLOW-3D setup video that can be found on the software users' site. A static friction coefficient of 0,2 for both the particles and the walls and a dynamic friction coefficient of 0,15 were used. These values were also used on the recommendation of the setup video.

From here, the concentration of the different particle sizes was set by navigating to the Particles tab and opening the concentration dropdown menu. Here the concentration values were set according to the data from Thejane et al. (2017) study, as this is the powder used for this study. The concentration of the different particle sizes that were used here can be seen in Table III. Lastly, in the same Particle tab, under the particle distribution dropdown menu, the particle distribution was set to random.

After this, the changes made were saved, FLOW DEM was closed, and the simulation was loaded into FLOW-3D and run. The resulting geometry looked like the one shown in Figure 63. In this figure, the particle diameter is indicated with colour, with red particles being the largest and dark blue the smallest. This part of the simulation only simulated particles falling on the substrate and did not consider a recoater blade being drawn over the particles to obtain the correct layer height. For this reason, the following simulation was used to simulate the spreading of powder by the recoater blade.

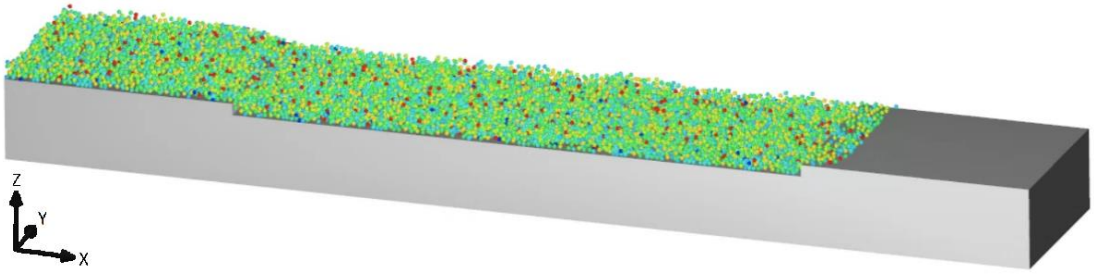

Figure 63: Powder bed geometry after particle-settling simulation, and before particle-spreading simulation

Upon completion of the simulation, the simulation icon was right-clicked, and the icon add restart simulation was selected. This enabled the software to use the results from the previous simulation as initial conditions for the simulation that was just created. Therefore, the only changes that had to be made to this restart simulation were the change in simulation time in the Global tab, the addition of a moving recoater blade that interacts with the particles and disabling the creation of new powder particles.

Disabling the creation of new powder particles was done by navigating to the Particles tab and turning off the status icon for block one in the Particles tab. The creation of a moving recoater blade that interacts with the particles requires two steps. Firstly, the moving and simple deforming objects physics model was enabled by navigating to the Physics tab, clicking the moving and simple deforming objects icon and clicking the activate general moving objects (GMO) checkbox. Secondly, a simplified recoater blade geometry was created by navigating to the Geometry tab and adding a rectangular box object with a width the same as the simulation domain and an arbitrary thickness of 150 µm. The blade geometry was created to the left of the domain when referring to Figure 63. The recoater blade was then given a constant velocity in the positive x-direction by accessing the properties of the moving object inside the geometry tab and selecting the edit moving object properties icon.

The foregoing was all the parameters that were changed. After this, the simulation was run, and the results obtained are shown in Figure 64.

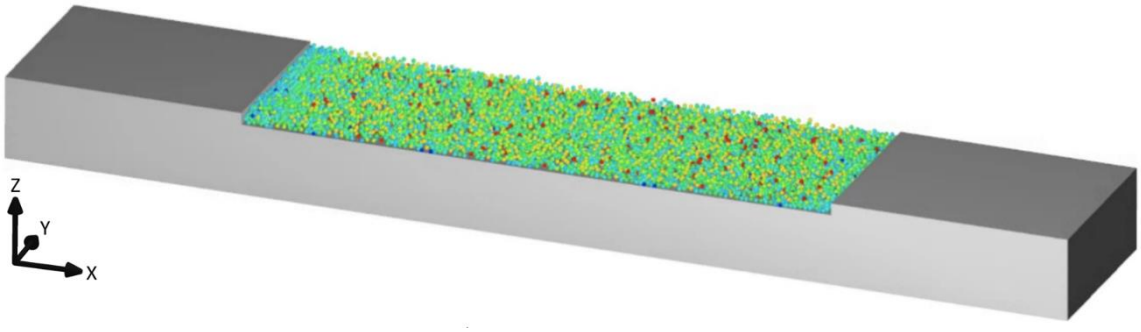

Figure 64: Resulting powder bed geometry after particle-spreading simulation

After this simulation was completed, the geometries of the particles were extracted from the simulation results file using the FLOW-3D Particle to STL conversion program. The results file was imported into the software, and the generate STL button was clicked on. This created an STL geometry file of the powder bed, which was saved into the directory for the simulation. The resulting geometry can be seen in Figure 65. In this figure, each grid line represents 100 µm.

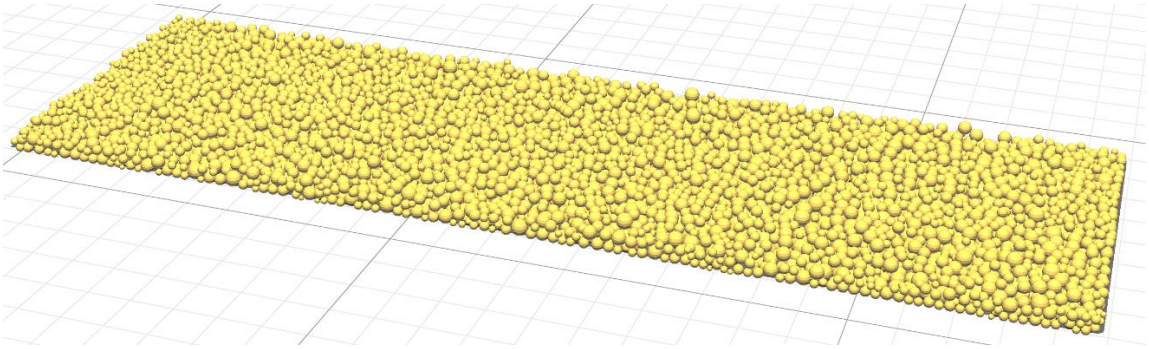

Figure 65: Resulting STL geometry after all particle simulations were completed

After running these simulations and obtaining the powder bed geometry, the only step left was to import the geometry file into a simulation without powder using the Geometry tab, setting the initial temperature to be the same as the substrate and lowering the substrate height by 50 µm. After these last changes were made, the simulations with powder could be run.

Appendix F – Experimental results without powder

	A	B	C	D	E	F	G	H	I	J	K	L	M	N	O	P	Q	R	S	T	U
1		Weak penetration					Optimal					Balling					Keyhole				
2		Depth belo	Height abo	Total heigh	Width at surfa		Depth belo	Height abo	Total heigh	Width at surfa		Depth belo	Height abo	Total heigh	Width at surfa		Depth belo	Height abo	Total heigh	Width at su	Keyhole width
3	1	21,70033	2,256835	23,95717	75,86437		70,65629	5,555286	76,21157	119,265		53,64323	13,88821	67,53144	104,856		56,24727	34,37333	90,62059	194,2614	na
4	2	20,48512	3,124848	23,60996	74,82275		72,39231	6,249696	78,64201	116,8346		51,7336	15,27704	67,01063	106,2448		49,65036	22,56835	72,21871	187,8381	na
5	3	21,70033	1,909629	23,60996	76,55878		69,44107	5,034477	74,47555	115,793		52,2544	15,45064	67,70504	105,5504		44,78949	15,97145	60,76094	214,5729	na
6	4	Data NA - Bad photograph					73,08672	4,166464	77,25319	117,1818		48,08794	13,36741	61,45535	110,0641		73,08672	12,8466	85,93332	201,0319	na
7	5	21,70033	2,430437	24,13077	81,24605		72,39231	4,687272	77,07959	119,0914		51,7336	13,88821	65,62181	105,5504		156,0688	8,853736	164,9225	196,8654	na
8	6	21,00592	3,298451	24,30437	75,51716		69,78827	5,555286	75,34356	116,8346		49,65036	18,22828	67,87864	107,9809		190,4421	13,0202	203,4623	188,5325	76,73238
9	7	20,65872	2,430437	23,08916	72,73952		72,39231	4,166464	76,55878	116,661		50,51838	11,28417	61,80255	105,724		127,7716	10,58976	138,3613	208,4968	na
10	8	22,56835	3,298451	25,8668	73,26033		72,04511	6,076094	78,1212	115,9666		52,77521	13,1938	65,96902	103,2936		53,12242	7,81212	60,93454	200,6847	na
11	9	21,35313	1,736027	23,08916	72,56592		71,00349	5,381683	76,38518	114,925		53,64323	13,0202	66,66343	105,8976		100,8632	9,72175	110,5849	202,7679	na
12	10	19,6171	3,472053	23,08916	72,56592		70,65629	4,687272	75,34356	118,397		53,29602	13,54101	66,83703	108,5017		182,8036	13,0202	195,8238	195,8238	76,90598
13	11	18,92269	3,298451	22,22114	73,43393		69,96188	5,728888	75,69077	114,925		51,38639	13,88821	65,2746	105,2032		158,8464	11,97858	170,825	198,0806	87,32214
14	12	21,17953	2,430437	23,60996	72,56592		69,78827	5,20808	74,99635	120,3067		48,43515	13,71461	62,14976	106,7656		234,19	15,62424	249,8142	190,9629	77,42679
15	13	20,31151	3,298451	23,60996	72,21871		70,48268	3,124848	73,60753	115,2722		52,77521	12,673	65,44821	105,0296		230,3707	15,45064	245,8214	189,2269	76,90598
16	14	20,48512	3,298451	23,78357	72,39231		71,1771	5,902491	77,07959	117,0082		53,81683	13,88821	67,70504	105,0296		196,6918	17,70747	214,3993	178,4635	86,10693
17	15	19,6171	3,472053	23,08916	72,39231		68,92026	4,340067	73,26033	118,9178		54,68484	16,31865	71,00349	107,1128		227,9403	15,79784	243,7382	183,8452	78,81561
18																					
19	Average	20,80752	2,839644	23,64716	74,15314		70,94563	5,057625	76,00325	117,1587		51,89563	14,10811	66,00374	106,187		138,859	15,02242	153,8814	195,4303	80,03083
20	Std Dev	0,957308	0,589107	0,801421	2,422326		1,225372	0,831039	1,49231	1,633301		1,913798	1,597983	2,489408	1,626892		68,75341	6,326975	67,69186	9,115373	4,288674
21	RSD	4,600777	20,74581	3,389078	3,266653		1,727199	16,43142	1,963482	1,394093		3,687784	11,3267	3,771617	1,532101		49,51311	42,11689	43,98963	4,664257	5,358777
22																					

Appendix G – Experimental results with powder

	A	B	C	D	E	F	G	H	I	J	K	L	M	N	O	P	Q	R	S	T
1		Weak penetration					Optimal					Balling					Keyhole			
2		Depth belo	Height abo	Total Heigh	Width at surfa		Depth belo	Height abo	Total Heigh	Width at surfa		Depth belo	Height abo	Total Heigh	Width at surfa		Depth belo	Height abo	Total Heigh	Width at surface
3	1	7,11771	30,20686	37,32457	72,73952		71,3507	30,38047	101,7312	134,8893		47,56713	21,87394	69,44107	103,4672		198,4279	32,11649	230,5443	187,3173
4	2	7,985723	39,92861	47,91434	73,95474		62,84417	28,99165	91,83581	125,5147		28,29724	51,7336	80,03083	107,6337		216,8297	32,4637	249,2934	200,6847
5	3	9,027339	15,27704	24,30437	74,99635		54,68484	15,97145	70,65629	114,2306		48,43515	57,63609	106,0712	88,88457		222,0378	34,54693	256,5847	176,5539
6	4	6,596902	17,88108	24,47798	60,06652		74,82275	28,12363	102,9464	141,139		43,22707	18,05468	61,28174	98,43272		202,5943	30,38047	232,9748	183,1508
7	5	9,72175	18,92269	28,64444	66,48982		70,82989	33,15811	103,988	145,6526		46,35191	31,42208	77,774	87,32214		216,1353	33,85252	249,9878	179,6788
8	6	5,20808	41,31744	46,52552	43,05346		60,06652	29,16525	89,23177	143,0486		40,62303	16,31865	56,94168	110,7585		205,372	32,81091	238,1829	201,5527
9	7	10,41616	3,645656	14,06182	52,77521		60,76094	20,48512	81,24605	127,9452		48,43515	36,63016	85,06531	106,4184		215,7881	21,70033	237,4885	190,2685
10	8	6,249696	37,49818	43,74787	66,31622		72,73952	42,70626	115,4458	138,1877		43,22707	46,00471	89,23177	112,8417		219,6074	32,81091	252,4183	195,1294
11	9	5,728888	2,430437	8,159326	36,97737		65,2746	19,2699	84,5445	117,7026		42,01185	26,73481	68,74666	99,12713		200,8583	32,4637	233,322	188,3589
12	10	0	64,9274	64,9274	54,85844		66,31622	20,13791	86,45413	121,6955		15,45064	19,7907	35,24134	93,22463		147,3887	29,68606	177,0747	198,2543
13	11	10,93697	11,45778	22,39474	60,93454		72,04511	33,50532	105,5504	135,0629		0	106,765	106,765	103,8144		169,957	22,04754	192,0046	192,0046
14	12	0	n.a.	na	na		60,24013	31,76929	92,00942	119,4386		6,423299	28,99165	35,41495	137,4933		116,1402	36,28296	152,4231	214,2257
15	13	11,45778	9,027339	20,48512	55,90006		72,04511	24,47798	96,52309	131,07		40,10222	45,83111	85,93332	98,95352		81,07245	22,74195	103,8144	207,8024
16	14	15,45064	15,45064	30,90128	73,60753		67,18423	24,47798	91,66221	119,265		38,01899	54,16403	92,18302	93,91905		118,7442	22,74195	141,4862	199,1223
17	15	10,93697	44,61589	55,55286	50,69198		62,32336	21,00592	83,32928	137,1461		30,72767	18,74909	49,47676	122,3899		112,3209	31,07488	143,3958	202,0735
18																				
19	Average	7,788973	25,18479	33,53012	60,24013		66,23521	26,90841	93,14362	130,1326		34,59323	38,71335	73,30658	104,3121		176,2183	29,84809	206,0664	194,4118
20	Std Dev	4,005606	17,58285	15,76631	11,49061		5,75526	6,784586	11,05416	9,756573		15,01912	22,75255	21,70489	12,66576		46,44359	4,802436	48,34095	10,10319
21	RSD	51,42662	69,81534	47,02135	19,07468		8,689124	25,21362	11,86787	7,497411		43,41636	58,77185	29,60838	12,14218		26,35571	16,08959	23,45892	5,196798
22																				

Appendix H – Variation of evaporation pressure and accommodation coefficient

Accommodation coefficient 0.05

Evaporation pressure of 5 000, 10 000, 20 000, 30 000, 40 000, 50 000 for each accommodation coefficient.

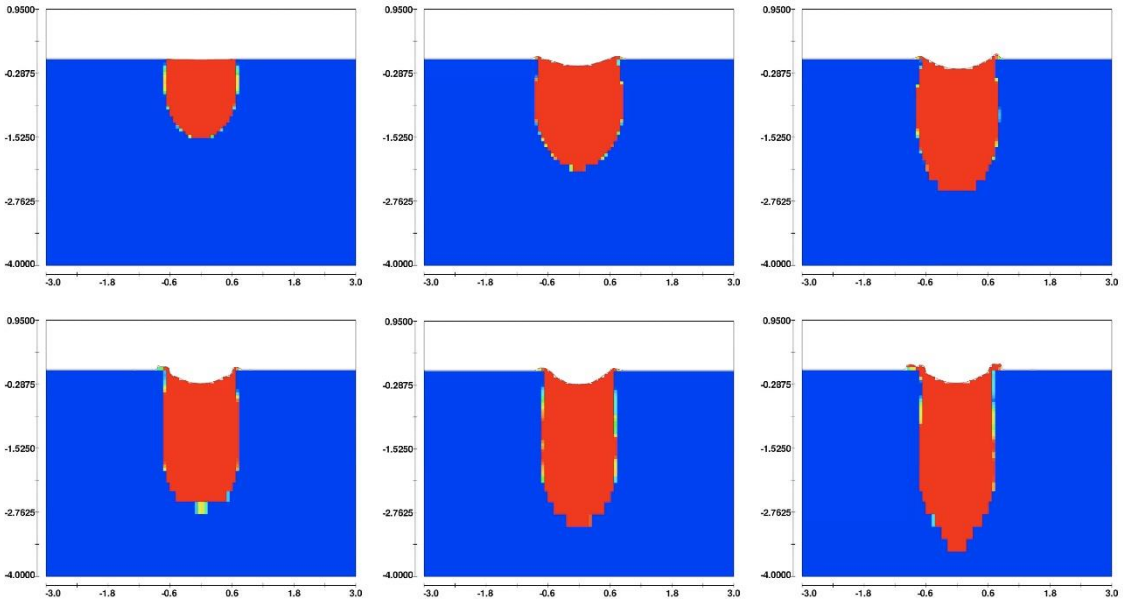

Accommodation coefficient 0.1

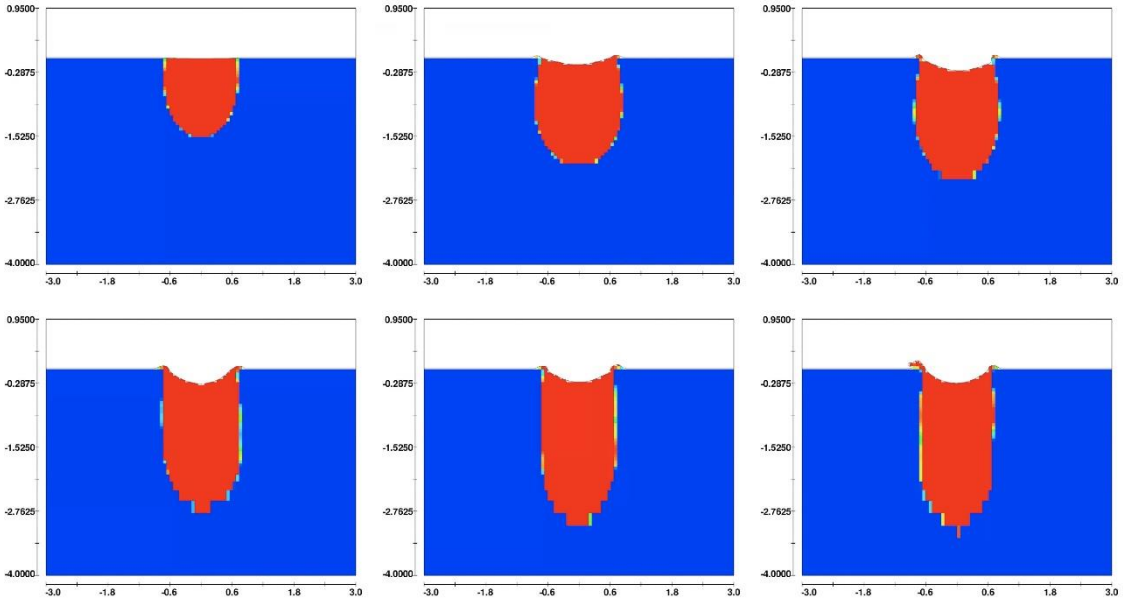

Accommodation coefficient 0.2

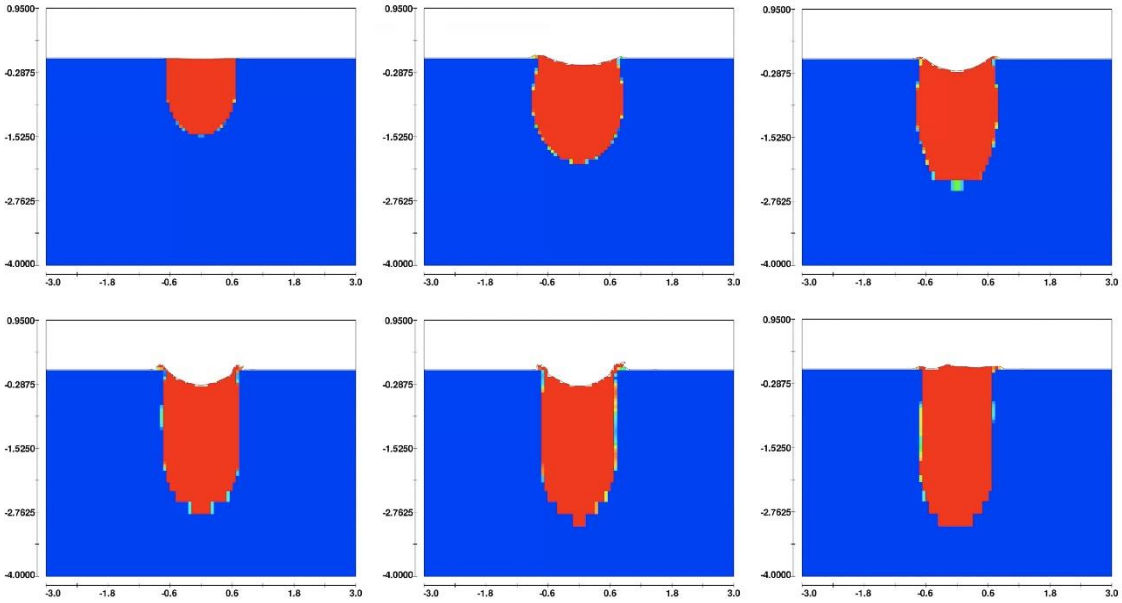

Accommodation coefficient 0.3

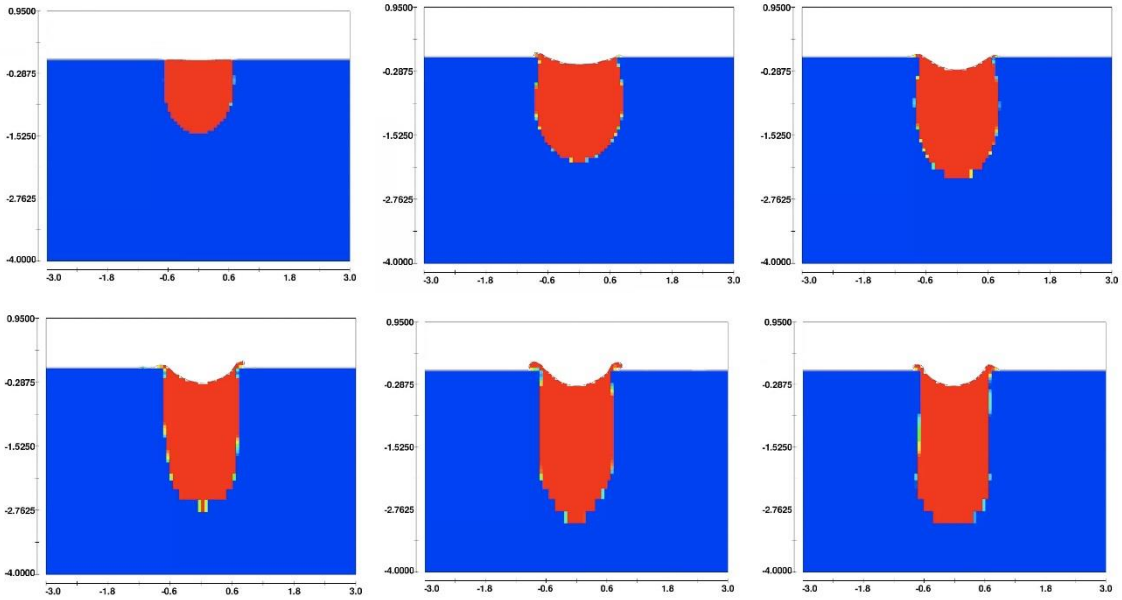

Accommodation coefficient 0.4